Multi-dimensional Flow and Combustion Diagnostics

Xuesong Li

Dissertation proposal submitted to the faculty of the Virginia Polytechnic Institute and State University in partial fulfillment of the requirements for the degree of

Doctor of Philosophy

In

Aerospace Engineering

Lin Ma Chair

Srinath Ekkad

Kevin T. Lowe

Heng Xiao

April 16, 2014

Blacksburg, VA

Keywords: Optical diagnostics, Tomography, Combustion diagnostics

Multi-dimensional Flow and Combustion Diagnostics

Xuesong Li

Abstract

Turbulent flows and turbulent flames are inherently multi-dimensional in space and transient in time. Therefore, multidimensional diagnostics that are capable of resolving such spatial and temporal dynamics have long been desired; and the purpose of this dissertation is to investigate three such diagnostics both for the fundamental study of flow and combustion processes and also for the applied research of practical devices. These multidimensional optical diagnostics are a 2D (two dimensional) two-photon laser-induced fluorescence (TPLIF) technique, a 3D hyperspectral tomography (HT) technique, and a 4D tomographic chemiluminescence (TC) technique. The first TPLIF technique is targeted at measuring temporally-resolved 2D distribution of fluorescent radicals, the second HT technique is targeted at measuring temperature and chemical species concentration at high speed, and the third TC technique is targeted at measuring turbulent flame properties. This dissertation describes the numerical and experimental evaluation of these techniques to demonstrate their capabilities and understand their limitations. The specific aspects investigated include spatial resolution, temporal resolution, and tomographic inversion algorithms. It is expected that the results obtained in this dissertation to lay the groundwork for their further development and expanded application in the study of turbulent flow and combustion processes.

Preface

This dissertation is submitted for the degree of Doctor of Philosophy at Virginia Tech. The research conducted herein was conducted under the supervision of Professor Lin Ma at the Department of Aerospace and Ocean Engineering from Aug. 2011 to May. 2014, and at the Department of Mechanical Engineering at Clemson University from Aug. 2009 to Aug. 2011.

This work is to the best of my knowledge original. The purpose of the dissertation in to introduce and demonstrate some novel approaches to perform multi-dimensional flow and combustion diagnostics. These multi-dimensional approaches implemented robust algorithms such as simulated annealing and Monte Carlo simulation to promote the efficiency and fidelity of tomographic methods. Then verifications and applications of the purposed diagnostics methods were illustrated in this dissertation.

I was the lead investigator for the work in Chapter 2, which introduced a numerical method to simulate two-photon laser-induced fluorescence and amplified spontaneous emission. The ASE effects represent a major challenge to the application of TPLIF as a flow diagnostics that is more difficult to correct. A correction method was developed and demonstrated to correct for the distortion caused by ASE effects. I was responsible for major areas of concept formation, analytical studies and numerical simulation.

I was one of the lead investigators for the work in Chapter 3, which reports a new 3D laser diagnostic that can measure 2D distribution of temperature and H_2O concentration simultaneously with a temporal resolution of 50 kHz at 225 spatial grid points. To our knowledge, it is the first time that such measurement capabilities have been reported. I

was responsible for the optimization of HT algorithms and processing the experimental data for practical applications. Dr. Weiwei Cai was involved in the early stage of concept formation and verification. The research group in University of Wisconsin, Madison, led by Professor Scott Sanders was credited for experimental implementation of the purposed HT technique.

I was the lead investigator for the work in Chapter 4, which introduced a 4D flame diagnostics method based on tomographic chemiluminescence. The contribution of our research is threefold. First, a hybrid algorithm is developed to solve the TC problem. Second, a set of experiments were designed to both demonstrate the TC technique, and also to examine its performance quantitatively. Third, based on the reconstruction algorithm and experimental results, we investigated the effects of the view orientations. I was responsible for major areas of concept formation, analytical studies and numerical simulation. I also designed and carried experiments to validate the proposed TC technique.

Part of the work has been presented in the following publications:

Cai, W., **Li, X.**, Ma, L., "Practical aspects of implementing three-dimensional tomography inversion for volumetric flame imaging", Applied Optics **52** (33), 8106-8116 (2013)

Cai, W., **Li, X.**, Li, F., and Ma, L., "Numerical and Experimental Validation of a Three-dimensional Combustion Diagnostic Based on Tomographic Chemiluminescence," Optics Express, **21**(6), 7050-7064 (2013)

Li, X., Zhao, Y., and Ma, L., "Method to Correct the Distortion Caused by Amplified Stimulated Emission as Motivated by LIF-based Flow Diagnostics," Applied Optics, 51(12), 2107-2117 (2012).

An, X., Kraetschmer, T., Takami, K., Sanders, S., Ma, L., Cai, W., Li, X., Roy, S., and Gord, J. R., "Validation of Temperature Imaging by H_2O Absorption Spectroscopy Using Hyperspectral Tomography in Controlled Experiments," Applied Optics, 50(4), A29-A37 (2011)

Acknowledgement

It would not have been possible for me to accomplish this doctoral dissertation and my Ph.D. study without the help and support from the people around me. I would like to take this opportunity to thank all those who have contributed in my academic and personal life. Over the past five years, I have received immeasurable help and advice from my advisor, Dr. Lin Ma, who has been a mentor, supervisor, and friend to me for years and to whom I owe my sincere gratitude. I also would like to thank Dr. Todd Lowe, Dr. Ekkad Srinath, and Dr. Heng Xiao for serving on my advisory committee and providing me academic and professional suggestions.

I would like to express my thanks to my colleagues in Virginia Tech and Clemson University for sharing the unforgettable and rewarding journey with me. They are Dr. Weiwei Cai, Dr. Yan Zhao, Dr. David Ewing, Minwook Kang, Fan He, Yue Wu, Qingchun Lei, Zhenyu Xue, Donald Brooks, Tobias Ecker, Pietro Francesco, Litao Liang, Shuaishuai Liu, Wei Li, and many others.

My greatest gratitude goes to my families and my girlfriend, Siyi Dai, for their love and supports which has led and encouraged me towards a more challenging yet rewarding future.

Table of Contents

Figure Captions

Chapter 1 Introduction

1.1 Overview of optical diagnostics

Non-intrusive optical diagnostics are indispensable tools for both the fundamental study of turbulent flows and flames, and also applied research and diagnosis of practical devices [1]. Compared to intrusive techniques such as Pitot tubes and thermocouples, optical diagnostic methods offer several key advantages. First and foremost, optical diagnostics techniques are non-intrusive and do not disturb the target flow fields. Secondly, because optical diagnostics do not involve the direct contact between a physical probe with the measurement medium, they can endure harsh measurement environments such as high temperature, high pressure, and corrosive species [2]. Lastly, optical diagnostics also provide excellent perspective for remote implementation, which are critical for onboard, *in situ*, and distributed implementation.

A wide spectrum of optical diagnostic techniques has been developed in the past for flow and combustion research. As an incomplete list, these methods include absorption techniques [3, 4], Mie scattering [5, 6], Raman scattering [7], Rayleigh scattering [8], coherent anti-stokes Raman scattering (CARS) [9], laser-induced fluorescence (LIF) [10], laser-induced incandescence (LII) [11], laser Doppler velocimetry[12], particle imaging velocimetry (PIV) [13], chemiluminescence [14, 15], and phase Doppler anemometry [16]. These methods are based on different physics (i.e., emission, excitation, refraction, etc.) and they are primarily targeted at measuring one or two flow or combustion properties (e.g., velocity, temperature, species concentration, or particle size distribution). It is worth noting that no single one technique can provide all

the properties desired or needed in a typical experiment, and therefore multiple different techniques are usually required.

Before further discussion of the specific techniques studied in this dissertation, this dissertation would like to point out some of the limitations and difficulties in optical diagnostics applications. First, optical access is always a concern in the implementation of optical diagnostics, and practical devices typically have limited optical access. It can be quite difficult to overcome the practical constraints and obtain the necessary optical access in a practical device such as an gas turbine engine [1]. Second, the quantitative interpretation of the optical signal is non-trivial. Converting the optical signal to the target flow or flame properties often involves sophisticated modeling and other inputs (such as the quenching rates in LIF measurements). Third, the capital cost of optical diagnostics (including cameras and lasers) relatively expensive. Significant research efforts have been investigated to address these limitations. For example, fiber optics or imaging fiber bundles have been utilized to address the issue of optical access, and both 1D measurement (single fiber optics) [17] and 2D measurement (imaging fiber bundles) [18] have been demonstrated with relatively small window size. The use of fibers also facilitate remote measurement and control based on optical diagnostics (attenuation in fibers could be an issue and optical multipliers and intensifiers [19] could be employed to compensate for the signal attenuation). Regarding the second issue of signal interpretation, researchers nowadays typically have multiple diagnostic methods at their disposal and can measure several properties simultaneously. These simultaneous measurements can either be used as inputs to obtain quantitative inferences of the target property, or be used to confirm the inferences of the target property. And lastly, with the

continuing technological advancements, optics and electronics are becoming more power and also more affordable, paving the path for expanded application of optical diagnostics.

1.2 Current development of multi-dimensional diagnostics methods

Before any further discussion, it is essential to clearly define dimensionality for the "multidimensional" work in this dissertation. This work defines dimensionality based both on space and time. If a technique can resolve a target quantity in all three spatial coordinates (i.e., x, y, and z) and time, then the measurement is defined as a 4D technique – the ultimate goal of measurement techniques. If a technique can resolve a target quantity in two spatial coordinates (i.e., a planar measurement) and time, then it is called a 3D technique. If a technique can resolve a sought quantity in all three spatial coordinates but without temporal resolution, this work also defines it as a 3D technique. Under this definition, multidimensional measurements in this dissertation refers to 3D and 4D measurements primarily.

It is also important to clarify the treatment of single short measurements and continuous measurements. Optical techniques can be qualitatively divided into two categories. This work will name the first category single shot techniques, and the second category continuous techniques. The first category of techniques make one measurement in a short duration (e.g., a few nanosecond), but are only able to make either one such measurement or are able to make another subsequent measurement after a long delay (relative to the time scale needed to resolve flow or flame dynamics). The second category of techniques can make measurements continuously at high rate and each measurement during a short duration (again, both relative to the time scale needed to resolve flow or flame dynamics). This work does not consider counting the temporal

resolution in single short measurements to be an additional dimension. For example, a single shot measurement of a property in 2D is considered just a "2D" measurement, not a 3D measurement, no matter how rapidly the single shot measurement is taken. On the other hand, if a series of 2D measurements of a target quantity are taken continuously, and each measurement during a short measurement duration, then such measurements will be defined as 3D measurements in this work. Clearly, such treatment of single shot and continuous measurements is arbitrary, and this dissertation adapted such a particular treatment mostly to emphasize "temporal resolution" in the sense of studying temporal correlations.

Based on the above definition of dimensionality, this work is mostly focused on obtaining 3D or 4D measurements in turbulent flows and flames. There are several possible approaches to obtain such measurements, but some of them are only at a conceptual stage at this time. Therefore, here we will focus the discussion on two of these possible approaches: the first approach involves a rapid scanning a low dimensional technique to obtain a high dimensional measurement, and the second approach involves obtaining a high dimensional measurement instantaneous (without scanning) via tomography.

Techniques in the first category involve rapidly scanning a low dimensional technique to obtain high dimensional measurements. For example, when the probing laser sheet used for obtaining 2D planar measurements is scanned rapidly (e.g., using a rotational mirror [20, 21]) at multiple locations, such 2D measurements can be "stacked" together and form a 3D or 4D measurements depending on the rapidness of the scanning relative to time scale of the processes. Results obtained by this first category of

techniques are straightforward to process (e.g., via a simple “stacking”), and their spatial resolution are defined by the spatial resolution of the low dimensional technique and the scanning step size. However, the disadvantage of such method is that the scanning speed must be high enough for the flow to be assumed stationary during the measurement, which is difficult when the flow is very turbulent and transient. Otherwise, the measurements are not simultaneous and the results cannot reflect the instantaneous flow features. Furthermore, the experimental setup of such measurements is often complicated since translational or rotational devices with high precision and high speed are required, or multiple laser devices have to be utilized and synchronized.

Techniques in the second category obtain high dimensional measurements from tomography. In such tomographic techniques, multiple line-of-sight-averaged projections (i.e., low dimensional measurements) are obtained simultaneously and these projections are used as the inputs for the subsequent tomographic reconstruction to obtain high dimensional measurements. The advantage of such tomographic techniques is that they do not require scanning and can achieve instantaneous and volumetric measurements (given that all the projection measurements were obtained simultaneously). Besides the simultaneity advantage, with current technologies, we can also typically obtain multiple projections simultaneously at higher temporal rate than scanning or traversing a low dimensional technique in the first category, resulting in a better temporal resolution. On the other hand, tomographic techniques do have disadvantages or issues to be further investigated. Firstly, the spatial resolutions of the tomographic measurements are not as definitively defined as those in the scanning techniques. The spatial resolutions of tomographic measurements are not only influenced by the laser and optical system, but

also by the inversion process itself. Furthermore, tomographic inversion is a computationally expensive process. The computation requirement is further compounded by the high-speed nature of most practical flows and flames. These issues will be further elucidated in the subsequent chapters of this dissertation, together with our ongoing efforts to address them.

Again, in this dissertation we will mainly focus on the tomographic methods for obtaining multi-dimensional measurements, and thus past work on combustion diagnostics based on tomography approach is summarized here. Past efforts included tomography sensing of the distribution of chemical species and temperature using tunable diode laser absorption spectroscopy (TTDLAS) [22, 23], and also later with hyperspectral absorption tomography (HT) [24, 25], in which new laser sources were used to probe many absorption transitions in significantly wider spectra range than diode lasers. For velocity measurements, researchers have combined traditional 2D PIV (particle imaging velocimetry) with tomography and developed tomographic PIV for 3D and three-component velocity measurements, and such measurements have been demonstrated in passive flows [26, 27], [26, 27]. To resolve 3D turbulent flame fronts, researchers have demonstrated tomographic Mie scattering [28], and tomographic chemiluminescence (TC) measurements [14, 15]. These past work demonstrated the capability and practical potential for tomographic techniques. Based on such previous efforts, this work emphasizes the fundamental study of tomographic approaches, using both numerical simulations and controlled experiments for experimental validation. Numerical simulations play a significant role in this dissertation for the verification purpose, mainly because generating turbulent flows in a controlled way is experimentally difficult, if

possible at all. Several numerical approaches, such as computational fluid dynamics (CFD) [29, 30] and Monte Carlo (MC) [6, 31] simulations are applied for such verification and validation purposes. Parallel to these numerical simulations, controlled flow and flames were implemented to experimentally validate and verify the multidimensional diagnostics investigated in this work.

The rest of this dissertation is organized as the following. Chapter 2 discusses the 2D measurements of combustion species (especially atomic and minor species) using 2D two-photon LIF (TPLIF) technique. The focus here is to investigate the effects of amplified spontaneous emission (ASE) in 2D TPLIF measurements. A MC method was developed to address such effects, and a practical method has been developed to correct ASE and enabled the quantitative interpretation of 2D TPLIF measurements. Chapter 3 discusses a 3D techniques based on hyperspectral tomography. This chapter describes both the fundamental of obtaining measurements of chemical species and temperature in two spatial coordinates and time (thusly 3D measurements) and its application in the exhaust plane of a GE J85 jet engine. Chapter 4 describes a 4D technique (3D in space and 1D in time) based on tomographic chemiluminescence (TC). This chapter both discusses the fundamentals of 4D tomography, and also reports the demonstration flame measurements obtained with this technique. Lastly, this chapter also discusses some practical aspects of the TC technique, such as the stopping criterion of the reconstruction algorithm and the spatial resolution. Finally, Chapter 5 summarizes this dissertation and outlines possible future research directions.

Chapter 2 2D Two-photon Laser-induced Fluorescence (TPLIF)

2.1 Background

Among the numerous laser diagnostics developed, techniques based on LIF (laser-induced fluorescence) offer several key virtues, including species selectivity, strong signal to enable two-dimensional imaging measurements of minor species, and relatively simply instrumentation [1, 2]. Due to these virtues, LIF-based diagnostics have been extensively applied in a wide range of areas. However, many species of great interest to combustion and plasma research have LIF transitions in the VUV (vacuum-ultraviolet) spectral range [32]. These species include most of the light atoms (e.g., hydrogen, carbon, oxygen, and fluorine) [32, 33], the noble gases (e.g., krypton and xenon) [34, 35], and some molecular species (e.g., carbon monoxide and ammonia) [36-38]. To circumvent the experimental difficulty encountered in the VUV range, multi-photon LIF techniques were developed to excite the target species via the absorption of two photons (i.e., two-photon LIF, TPLIF). Besides avoiding the experimental difficulty, TPLIF also enables a more comfortable spectral separation between the excitation wavelength (usually in the UV range) and the fluorescence wavelength (usually in the near infrared region) in comparison to one-photon LIF.

However, the two-photon process also creates complications [32]. One key issue involves the small two-photon cross-section area, which motivates the use of laser pulse with high radiance for excitation to enhance signal and to enable 2D (two-dimensional) measurements. The use of excitation pulse with high radiance can trigger several side effects, with photo-chemistry [39] and ASE (amplified stimulate emission) [40] being

two most notable ones. This chapter focuses on the ASE effect. As illustrated in Panel (a) of Figure 2-1, the laser field created by the excitation pulse, when strong enough, causes a non-negligible population inversion between the excited state 3 (with a population of n_3 and the same notation is used hereafter) and state 2. When such population inversion occurs, a LIF photon, as it propagates through the media, can stimulate a transition from the excited state to a state with lower energy and generate another photon. The photon generated subsequently stimulates other transitions and generate additional photons. When such process is sustained by the population inversion, an amplification of the stimulated photons occurs, a process often termed the amplified stimulated emission (ASE). When the ASE process occurs, the target species to be measured essentially behave as an active gain media.

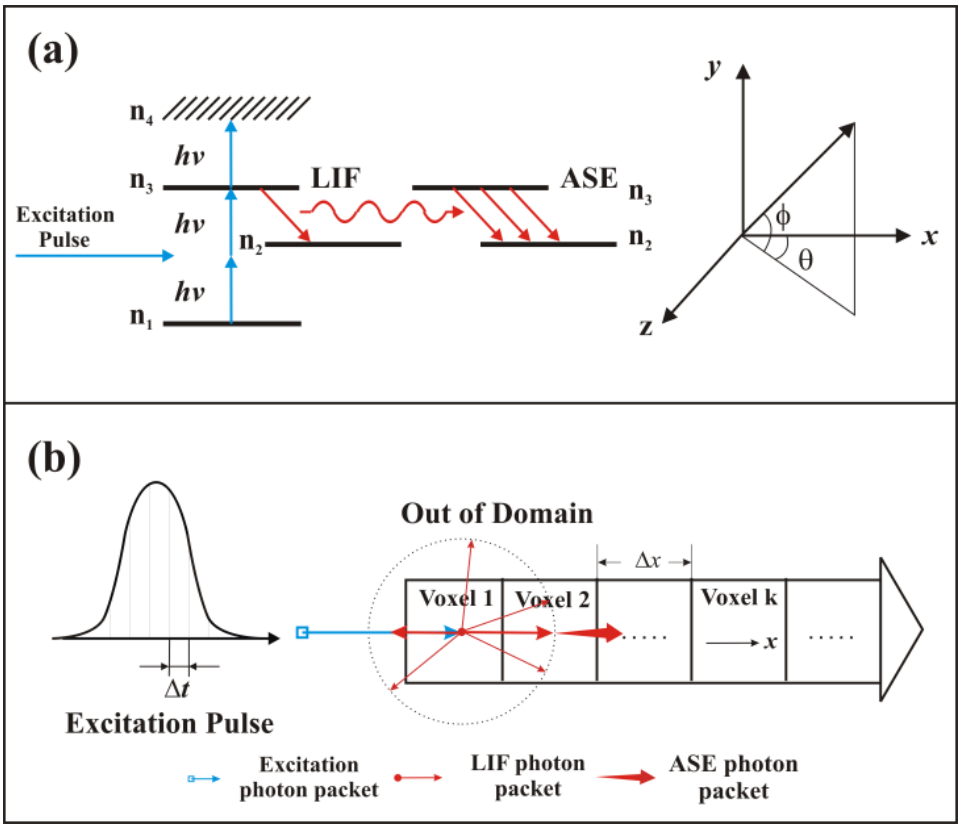

Figure 2-1. Panel (a) Illustration of the TPLIF process and ASE effects. Panel (b). schematic of the MC model in 1D. Panel (b). Schematic of the MC model in multi-dimensional.

The ASE process both represents an opportunity for a new diagnostic tool and poses a complication to the TPLIF diagnostic. The ASE signal can be a directional laser-like signal, and therefore is attractive for diagnostic purposes [40, 41]. However, the ASE signal depends nonlinearly on many factors, including the number density of the target species (i.e., n_1), the excitation radiance, the temporal behavior of the excitation pulse, etc. Therefore it is difficult to quantify the ASE signal. Furthermore, the ASE process depopulates the excited state (n_3), causing a nonlinear dependence of the LIF signal upon the factors aforementioned and complication the interpretation of the LIF signal [35, 42].

Therefore, there is a research need to model and quantitatively understand the ASE effects, so that its use as a diagnostic tool can be quantified and its effects on the LIF

signal can be corrected. Such consideration has motivated a large amount of modeling efforts around the ASE effects. Models based on the rate equation approximation represented a significant portion of past work due to their simplicity [43-50]. Rigorous models included those based on the density matrix formulation [51, 52] and the Maxwell-Bloch equations [53]. These models have thus far been mostly limited to relatively simple 1D applications and extension to realistic scenarios is not trivial. A model based on the Monte Carlo (MC) method was developed to simulate the ASE effects [31]. The MC method was validated against other models in 1D and pervious experimental data. The results obtained in [31] demonstrated that the MC method offer several distinct advantages, including the simplicity in implementation and the capability to model realistic conditions (e.g., temporal and spatial profile of excitation pulse, complicated 3D geometry, and non-ideal optical components).

Based on these previous efforts, this current research applied the MC model to examine the ASE effect and its influence on the LIF signal, with the goal of developing a method to quantitatively interpret TPLIF measurements. The major contribution of the research in this chapter is the numerical demonstration and evaluation of a method that can quantify the LIF signal in the presence of ASE effects. The method involves measuring the LIF signal twice: the first time with an excitation pulse at a low radiance and the second time with an excitation pulse at a high radiance. The first LIF signal is free from ASE distortion but is noisy due to the low excitation radiance. In contrast, the second LIF signal has high SNR (signal-to-noise ratio) but is distorted due to the ASE effects triggered by the high excitation radiance. Our proposed method combines these two measurements to produce a faithful LIF measurement with high SNR. This research

explains the method and its underlying physics in detail, and reports numerical results to demonstrate its application in flow diagnostics. Finally, this research also examines the practical considerations for implementing the method. These results are expected to be useful for the design and analysis of experiments involving TPLIF, and for the expanded use of TPLIF for quantitative flow measurements.

2.2 Description of Monte Carlo model

Panel (a) of Figure 2-1 illustrates the major processes in TPLIF, which involves a four-level system interacting with a laser pulse. An excitation laser pulse excites the target species from the ground level (level 1, with population denoted as n_1 and the same notation is used hereafter) to the excited level (level 3) via two-photon absorption. Atoms on the excited level can either absorb an additional photon to be ionized (level 4) or fluorescence to state 2 emitting a LIF photon. Then the LIF photon, as described in Section 2.1, triggers the ASE process when a population inversion exists. The coordinate system used in this chapter is also shown in Panel (a), with the positive x-axis defined in the propagation direction of the excitation laser pulse. These four levels are also coupled via collisional quenching, and stimulated and spontaneous emission (not shown in Figure 2-1). Spontaneous emission was not considered due to its relatively slow rate compared to other processes at the laser intensity under consideration here. All other processes were included in the mode.

The goal of any model development is to consider all the processes described above and to predict the temporal and spatial profiles of all the relevant physical properties, including the population at each level, the LIF photons, and the radiation field. Based on such understanding, various approaches have been proposed to model TPLIF process. In

this chapter, we used the MC method described in [31] due to its simplicity in implementation and its ability to incorporate non-ideal effects in the model.

Here we provide a brief summary of the MC model with the aid of Panel (b) in Figure 2-1 and more detailed description is provided in [31]. The measurement domain is discretized into voxels. Panel (b) uses a 1D array of voxels (with dimension Δx as shown) to explain the model, and extension of the MC model into multi-dimension is straightforward. The excitation pulse is discretized both temporally (with a step size of Δt as shown and $\Delta t = \Delta x / c$ where c represents the speed of light) and spatially so that arbitrary excitation profile can be considered in the model. The excitation pulse is modeled as N photon packets where $N = T / \Delta t$ with T representing the total duration of the excitation pulse.

The model starts by sending the 1st excitation photon packet into the 1st voxel. The absorption of this packet in the first voxel by the target species is calculated according to the 4-level model shown in Panel (a). The populations at all 4 levels (i.e., n_1 through n_4) in the first voxel due to the absorption are then updated. Then the number of LIF photons emitted in the first voxel during time Δt is calculated by $N^{LIF} = n_{3,1}\big|_{t=\Delta t} \cdot A_{32} \cdot \Delta t$ where $n_{i,k}|_t$ represents the population of the target species on level i in voxel k at time t, and A_{32} the Einstein A coefficients between states 3 and 2. These LIF photons are emitted randomly in all directions. Our MC model tracks these photons by 1) randomly generating M directions, and 2) dividing these LIF photons into M packets with each packet propagating in a direction generated in step 1. At this point, the MC model updates the populations at all levels in all voxels, the number of photons left in the first excitation packet, and the number and direction of all LIF photon packets.

Then the 2nd packet of excitation photons is sent into the first voxel cell, and similar calculations described in the above paragraph are repeated for these photons in the first voxel. The number of photons absorbed, the LIF photons emitted, and the populations at all levels are determined and updated. All these calculations are performed for the 2nd time step (i.e., for time $t=2\Delta t$). For the remaining photons in the 1st excitation packet (i.e., those transmitted through voxel 1), the MC model advances their position into voxel 2 and performs these same calculations described at voxel 2. For the LIF photon packets generated by the 1st excitation packet (in voxel 1), the MC model advances their position by Δx in the directions generated above and determines whether they exit the computational domain (as shown in Panel (b)). If a packet exits the computational domain, the MC model stops tracking it. If not, the new location of the LIF packet is determined and the ASE photons generated by the LIF photon packet in voxel 2 over a gain length of Δx are calculated. The ASE photons propagate in the same direction as the LIF photon packet that generates them.

At this point, the MC model updates the population on each level and each cell ($n_{i,k}$), the LIF photon packets and their directions, and the ASE photon packets and their directions. Temporally, such updates register the cumulative effects due to the 1st and 2nd packets of excitation photons; and spatially, such effects are limited within the first two voxels.

In this manner, subsequent packets of excitation photons are sent in one packet at a time. With the incident of each new excitation packet, the MC model 1) advances the spatial positions of the remaining photon packets (excitation, LIF, and ASE) caused by previous excitation packets by Δx, 2) advances the temporal step by Δt, and 3) repeat the

absorption, LIF emission, and ASE emission calculations described above. The MC model terminates when all photon packets (excitation, LIF, and ASE) have exited the computational domain. Extension of the MC model to the multidimensional domain is straightforward and has been detailed [31].

Figure 2-2 shows a set of sample results generated by the MC model to simulate the LIF and ASE signals generated by H atoms in a H_2/O_2/Ar flame [40]. Our MC model differentiates LIF and ASE signals: LIF signal is due to photons spontaneously emitted from state 3 to 2, and ASE signal is due to photons emitted by stimulated transitions from state 3 to 2. Specifically in Figure 2-2, the LIF signal represents LIF photons collected at a right angle, and the ASE signal ASE photons collected in the forward direction. Parameters used in the MC model were matched to the experimental conditions as described in [40]. Signals simulated by the MC model agree with the past experimental data both qualitatively and quantitatively. Qualitatively, the MC results agree with the well-known trend of the LIF and ASE signals [33, 40, 45, 48, 54]. For instance, the LIF signal first scales as I_L^2 when the excitation is weak, then scaling gradually becomes I_L^1 as the excitation energy increases, due to the increasing depopulation of level 3 caused by ionization and ASE at strong laser field. Note that the dashed lines on Figure 2-2 are only used to show the I_L^2 and I_L^1 scaling. Quantitatively, the experiments in [40] showed a $20\sim30\times$ increase in the ASE signal when the excitation energy increased from 0.2 to 0.6 mJ, compared to a $\sim20\times$ increase predicted by the calculations. Simulations were also conducted using the 1D rate equation extensively used previously simplicity [43-50]. The results are also shown on Figure 2-2, in good agreement with the MC model.

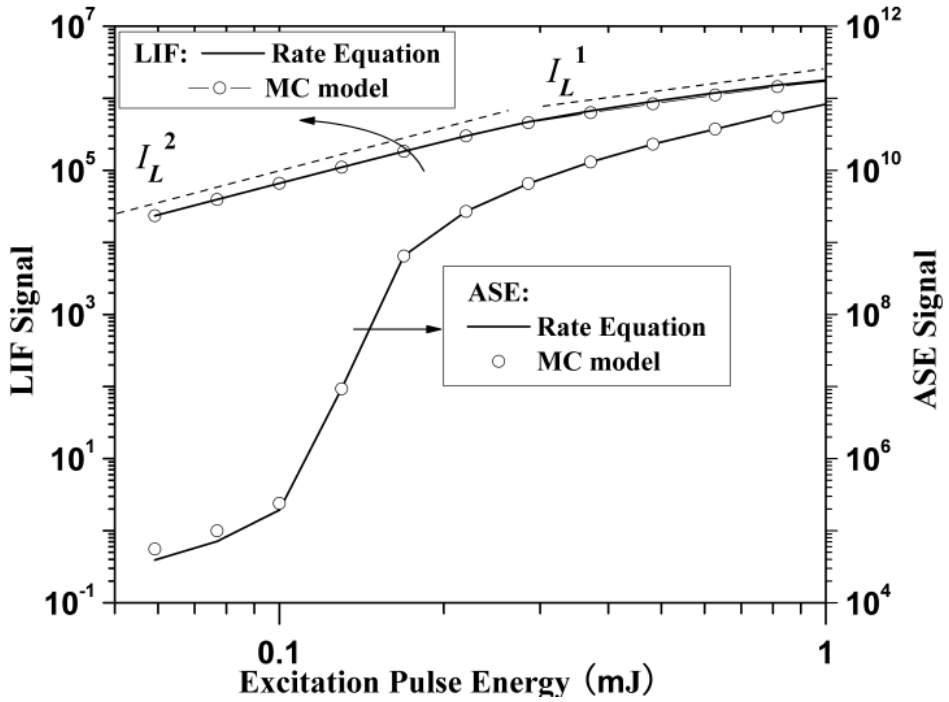

Figure 2-2. Comparison of the LIF and ASE signals calculated by the MC model and the rate equation. Calculations conducted to simulate the LIF and ASE signals from H atoms in a H2/O2/Ar flame.

Comparison of the MC model against previous experiments and the rate equation was also performed for H atom, under the conditions where experimental data are available [4, 16]. Good agreement similar to that shown in Figure 2-2 was obtained in all cases. A major reason for the good performance in these cases was attributed to the fact the measurement domain can be accurately approximated by a 1D domain. For example, in the H atom experiments [40], the measurement domain had a length of ~3 cm and a radius of ~120 μm, resulting in an aspect ratio of ~240. As the aspect ratio of the measurement domain decreases, the error caused by the 1D assumption in the rate equation increases [31]. This work chose to use the MC model for its straightforward extension to multi-dimensional. Other considerations also motivate the use of the MC model, including its simple implementation, the flexibility to incorporate non-ideal conditions (realistic geometries, laser profile, optical components, etc.), and its ability to

generate quantities that are difficult or even infeasible to obtain either experimentally or by the rate equation. These advantages will greatly facilitate the application of the method developed here in practice.

2.3 ASE effects in TPLIF measurements

To illustrate the effects of ASE in TPLIF measurements, the MC model was applied to a simple case where n_1 assumes a uniform (i.e., top-hat) distribution. The measurement domain was taken to be cylindrical with a length of 3 cm and a diameter of 250 μm, simulating typical conditions for 1D measurements in a laboratory flame.

Figure 2-3 shows the LIF and ASE signals calculated by MC model for H atom at an excitation wavelength of 205 nm and LIF/ASE photons at 656 nm. The ground state number density of H atom (n_1) was set to be 8.5×10^{14} cm^{-3}, obtained by an equilibrium calculation for a H_2/O_2/Ar flame. The excitation laser pulse was assumed to have a Gaussian temporal profile with a FWHM of 3.5 ns [48], the linewidth was assumed to be 6.88 cm^{-1} according to [55] and the diameter of the laser beam was assumed to be 250 μm. The quenching rates from level 2 and 3 were determined to be 8.1×10^{8} s^{-1} according to [56]. Other spectroscopic parameters are summarized in Table 2.1. In the MC model, the domain of interest (3 cm in length, 250 μm in diameter) was discretized into 120 cylindrical grids in the *x* direction. The grid's size was thus 250 μm in length and 250 μm in diameter. The time step Δt is set to be 0.83 ps.

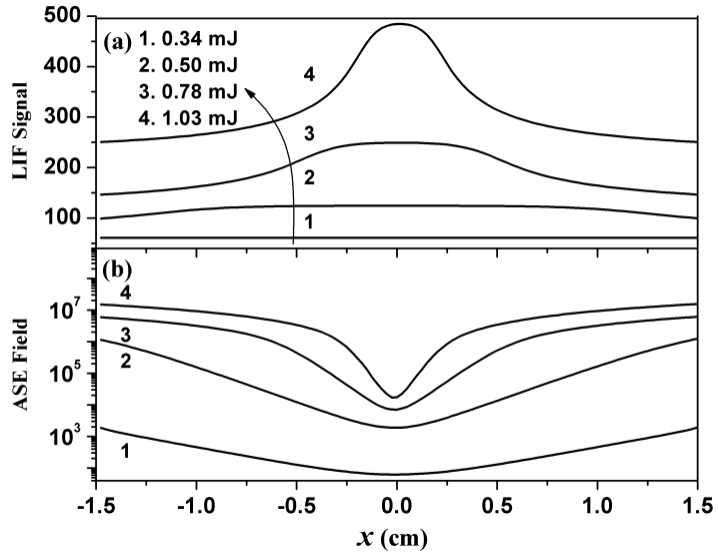

Figure 2-3. The LIF and ASE signals calculated by the MC model at various excitation pulse energy. The ASE field was represented by the number of ASE photons in each voxel at a time of 4 ns.

Table 2.1. Spectroscopic properties of H atom used

Parameters	Values	Units	References
Two photon absorption cross section	1.17×10^{-28}	cm^4/W	[27]
Ionization cross section	9.0×10^{-20}	cm^2	[30]
A_{32}	2.89×10^{7}	s^{-1}	[31]
A_{21}	4.7×10^{8}	s^{-1}	[31]

The results shown in Panel (a) of Figure 2-3 are intended to illustrate the signal level of a typical TPLIF measurement in practice. The LIF signal is in units of number of photons per pixel (ppp). In obtaining the LIF signal, the following parameters were assumed: an imaging system with 0.1% collection efficiency and 50% overall quantum efficiency, an integration time of 10 ns, a magnification of unity, and a pixel size of 10×10 μm^2. Panel (a) shows the LIF signal at four excitation energies, chosen to elucidate the onset and saturation of the ASE effects. At low excitation energy (case 1), the ASE field (shown in Panel (b) in units of ASE photons per voxel) was too low to generate appreciable distortion, and a flat LIF signal was observed, faithfully representing the true uniform distribution to be measured. As the excitation energy increases (cases 2, 3, and

4), the ASE fields grow rapidly and induce transition between n_2 and n_3 to compete with the quenching process. As a result, evident distortions in the LIF signal were observed. The LIF and ASE signals for these cases are shown on Figure 2-4 to illustrate the transition from the onset to the saturation of the ASE effects. The ASE signal in Figure 2-4 is in unit of photons per pulse and LIF signal is photons per pixel.

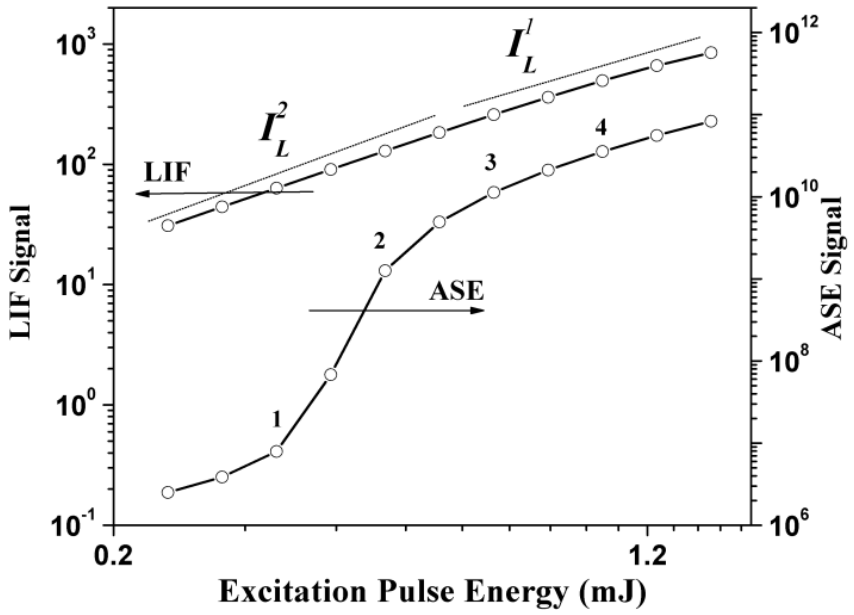

Figure 2-4. The LIF and ASE signal simulated for H atoms. The LIF signal corresponds to the number of LIF photons received on the voxel corresponding to $x = 0$. The ASE signal corresponds to the ASE photons received in the forward direction. An integration time of 10 ns was used for the calculation of both the LIF and ASE signals.

The results shown in Figure 2-3 also illustrate the dilemma in TPLIF applications. In practice, researchers typically design experiments to avoid the onset of significant ASE by using low excitation energy or by limiting the number density of target species to be measured. The LIF signal obtained in this case is free from distortion, at the cost of reduced signal level and hence low SNR. As shown in Figure 2-3, the LIF signal increased by a factor of ~8× when the excitation laser energy increase from 0.34 to 1.03 mJ. The complication in this case is that the LIF signal is distorted and no longer

represents the true distribution to be measured. The correction of such distortion is challenging because the distortion is non-linear (as shown here) and non-local, i.e., the distortion at one location depends on the conditions (such as n_1, temperature, etc.) at other locations. From this aspect, the correction of the ASE distortion is more difficult than the correction of quenching rate and ionization; and the correction of such distortion is the topic of the next section.

2.4 Correction of ASE distortion in TPLIF measurements

2.4.1 Introduction of correction method

Figure 2-5 illustrates the dilemma in TPLIF measurements discussed above. The LIF signals at relatively low and high excitation pulse energy are denoted as S_L and S_H, as shown in Panel (a) of Figure 2-5. Artificial noises were generated and added to the LIF signals to simulate practical measurements according to the following equations:

$$S_{LN} = P(S_L) + \varepsilon \text{ and } S_{HN} = P(S_H) + \varepsilon \quad (2.1)$$

where S_{LN} and S_{HN} represent the measured LIF signals with noise at low and high excitation energy, respectively; $P(S)$ represents a Poisson noise with an expectation of S and standard deviation of $\sqrt{S}$ to simulate the shot noise; and ε a Gaussian random noise with an expectation of zero and standard deviation of 10 counts to simulate the readout noise and dark noise typical to current CCD devices. Panel (a) of Figure 2-5 shows the simulated signals with and without noise, and Panels (b) and (c) show the relative noise for the LIF signals measured at low and high excitation energy, defined as S_{LN}/S_L and S_{HN}/S_H, respectively. As discussed above, the signal obtained at high excitation energy

enjoys a low noise (about ± 5%) compared to that obtained at low excitation energy (about ±30%). However, the signal at high excitation energy is distorted.

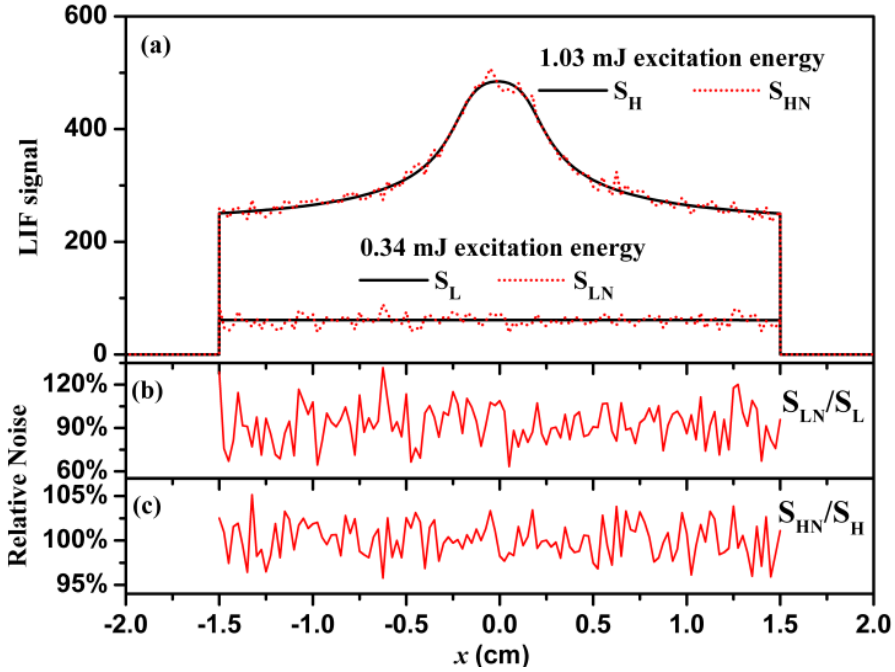

Figure 2-5. The LIF signals at relatively low and high excitation energies, with artificial noise added to simulate practical measurements.

Now we describe a method to correct the distorted signal and obtain a faithful measurement with high SNR. The method uses the LIF signals measured both with low and high excitation energies, as those shown in Panel (a) of Figure 2-5. Therefore, this method requires measuring the TPLIF signal twice, once with a low excitation energy and the second time with a high excitation energy. Admittedly, this requirement will result in additional implementation complication relative to the typical TPLIF setup, however the complication should be manageable. For the laser, a straightforward way of obtaining two measurements is to use two lasers to generate the two excitation pulses. Or alternatively, the output from one laser can be split into two beams, one with a low energy and one with a high energy. An optical delay is then introduced between these two

beams to take the measurements sequentially. For the camera, either two cameras or one camera (with double frame feature) can be used to capture the required measurements.

Our method to correct the distortion caused by ASE is built on an argument that is derived from the physics of ASE and confirmed by numerical simulations. The argument is that the ratio between the LIF signals obtained at low and high excitation energy has a relatively stable and smooth shape. As shown in Panel (a) of Figure 2-6, the ratio (R_{True} defined as S_L/S_H) has an inverted-bell shape. This shape (and its smoothness) is insensitive to the distribution of the target species to be measured (i.e., n_1), or the energy of the excitation pulses. This argument has been confirmed by extensive numerical simulations, and results for other example simulations will be shown later in this section. Here we explain the argument based on the physics of ASE. The shape of the ratio will be first explained, followed by the smoothness of the ratio.

2.4.2 Shape of ratio

The inverted-bell shaped is caused by the fact that the ASE effects are stronger at the two ends of the measurement region than in the mid, because the two ends offer more effective gain length [57]. Consequently, the depopulation will be more significant at the two ends than in the mid, in turn resulting in weaker LIF signal at the two ends than in the mid. Therefore, the distorted LIF signal, when normalized by an undistorted signal, exhibits the inverted-bell shape shown in Panel (a) of Figure 2-6. Here the flatness of the undistorted signal (due to the top-hat n_1 distribution) helps to understand this intuitive argument. But the argument holds for other distributions of n_1 also.

Further insights of this argument can be explained by analyzing the ASE radiation equations. Here we analyze the equations under steady state for the sake of brevity, and

similar analysis can be made for general cases. Under steady state, the gradient of the total ASE field (I_{ASE}) can be written as [45, 48]:

$$\frac{\partial}{\partial x} I_{ASE}(x) = \frac{B_{32}\Gamma}{c\Delta\nu_{ASE}} \left(I^{f}_{ASE}(x) - I^{b}_{ASE}(x) \right) \Delta n + A_{32}(\Delta\Omega_{f}(x) - \Delta\Omega_{b}(x)) n_3(x) h\nu_{ASE} \quad (2.2)$$

$$\Delta n = \left(n_3(x) - \frac{g_3}{g_2} n_2(x) \right) \quad (2.3)$$

where Δn represent the population inversion; g_i (i=1, 2, 3, 4) the degeneracy of each level; B_{32} the Einstein B coefficient from state 3 to state 2; Γ the overlap integral defined as $\int_{-\infty}^{+\infty} g(\nu) f(\nu) d\nu$ with $g(\nu)$ and $f(\nu)$ representing the line shape function of the absorption transition and the ASE radiation, respectively; $\Delta\nu_{ASE}$ the linewidth of the ASE radiation; I^{f}_{ASE} and I^{b}_{ASE} the irradiance of the ASE photons in the forward (i.e., positive x) and backward (i.e., negative x) directions, respectively; A_{32} the Einstein A coefficient for transition from state 3 to state 2; $\Delta\Omega_f$ and $\Delta\Omega_b$ the solid angle formed by the incident and exit surface of the domain of interests relative to the point at which the ASE photons are emitted; h the Planck constant; and ν_{ASE} the frequency of the ASE photons.

As can be seen, $I^{f}_{ASE}(x)$, $I^{b}_{ASE}(x)$ and $I_{ASE}(x)$ are coupled by Eq. (2.2). In the first term on the right hand side of Eq. (2.2), $I^{f}_{ASE}(x)$ increases monotonically with x while $I^{b}_{ASE}(x)$ decreases. Therefore, the first term starts from a negative value at the incident end and grows to a positive value at the exit end. The same trend also applies to the second term, i.e., $(\Delta\Omega_{f}(x) - \Delta\Omega_{b}(x))$ from simple geometrical consideration. Hence, $I_{ASE}(x)$ starts with a negative gradient from the incident end, and transitions to a positive gradient at the exit end, leading to the inverted-bell shape of the ratio. Also note that

$\Delta\Omega_f(x) = \Delta\Omega_b(x)$ at the center of the measurement domain, which suggests that the minimum of $I_{ASE}(x)$, and thusly the tip of the bell, tends to be located at the mid of the measurement domain. The location will be exactly at the middle point if $I^f_{ASE}(x)$ also equals $I^b_{ASE}(x)$ there (e.g., in the case of a symmetric n_1 distribution).

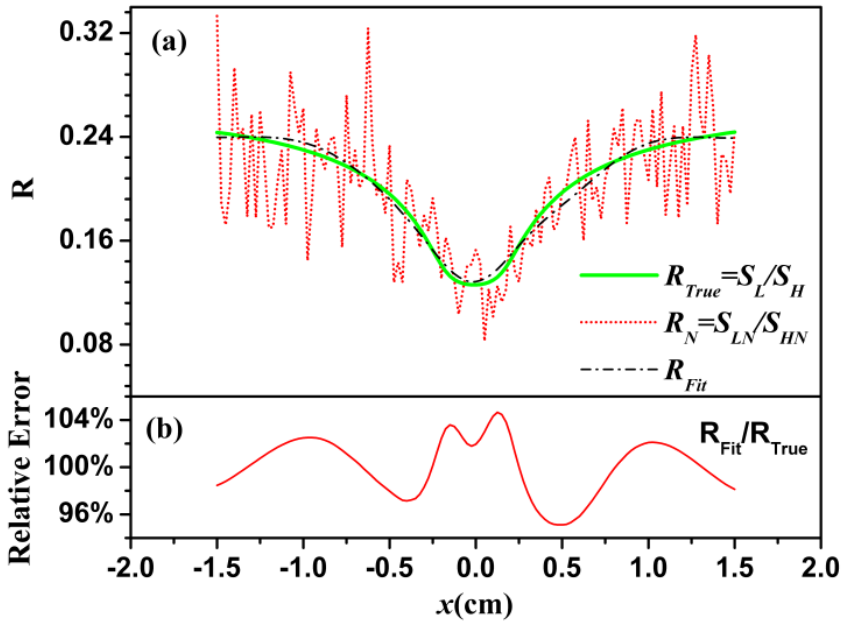

Figure 2-6. Panel (a): the ratio between the LIF signals obtained at low and high excitation energy. Panel (b). the relative error in the fitted ratio.

2.4.3 Smoothness of ratio

Having explained the shape of the ratio curve, we now examine the smoothness of this curve. This curve is smooth even if the n_1 distribution fluctuates significantly spatially. The reason is that the ASE effects are accumulative along the path. As a result, the fluctuations (or discontinuities) in n_1 will be smoothed out. This reasoning can be analyzed mathematically based on the ASE radiation equations. Here again, we analyze it under steady state for the sake of brevity. Similar analysis can be made for general cases. Under steady state, Eq. (2) is the governing equation for the ASE field. If only the field

caused by ASE photons in the forward direction is considered, then Eq. (2.2) is modified to:

$$\frac{\partial}{\partial x} I^{f}_{ASE}(x) = \frac{B_{32}\Gamma}{c\Delta\nu_{ASE}} \cdot I^{f}_{ASE}(x) \cdot \Delta n + A_{32} \cdot \Delta\Omega_{f}(x) \cdot n_3(x) \cdot h\nu_{ASE} \qquad (2.4)$$

Based on Eq. (2.4), we will show that the ratio cause by $I^{f}_{ASE}(x)$ is smooth, and a similar analysis can be made for $I^{b}_{ASE}(x)$.

Two assumptions can be made to simplify Eq. (2.4) and obtain an analytical solution: 1) Δn is assumed to be equal to n_3 because n_2 is typically insignificant compared to n_3, and 2) $\Delta\Omega_f(x)$ *is* assumed to be independent of x. The essence of this analysis is to show that the ASE effects and the ratio are smooth when n_1 is not. As to become more clear later, these assumptions are only needed to simplify the algebra and do not change the essence of this analysis (unless $\Delta\Omega_f(x)$ itself is a non-smooth or discontinuous function). Under these assumptions, solving Eq. (2.4) with the boundary condition $I^{f}_{ASE}(0)$ =0 yields:

$$I^{f}_{ASE}(x) = \frac{A_{32}\Delta\Omega_{f} h\nu_{ASE}}{B_{32}\Gamma / c\Delta\nu_{ASE}} \exp\left(\frac{B_{32}\Gamma}{c\Delta\nu_{ASE}} \int_0^x n_3(x)dx\right) - \frac{A_{32}\Delta\Omega_{f} h\nu_{ASE}}{B_{32}\Gamma / c\Delta\nu_{ASE}} \qquad (2.5)$$

Eq. (2.5) already illustrates that the ASE effects do not directly depend on $n_3(x)$, which can be non-smooth or discontinuous. Instead, the ASE effects depend on $\int_0^x n_3(x)dx$. Therefore, even when $n_3(x)$ is non-smooth or discontinuous (rooted from by $n_1(x)$), the integration smoothes out the distribution. The rate equation for the population on state 3 is:

$$0 = W_{13}\left(n_1 - \frac{g_1}{g_3} n_3\right) - \left(W^{f}_{32} + W^{b}_{32}\right)\left(n_3 - \frac{g_3}{g_2} n_2\right) - \left(W_{34} + A_{32} + Q_{3a}\right) n_3 \qquad (2.6)$$

$$W_{32}^{f} = \frac{B_{32} I_{ASE,f}}{c\Delta\nu_{ASE}}\Gamma \text{ and } W_{32}^{b} = \frac{B_{32} I_{ASE,b}}{c\Delta\nu_{ASE}}\Gamma \tag{2.7}$$

where W_{13} and W_{34} represent the transition rate coefficients of two-photon absorption and ionization, respectively; W_{32}^{f} and W_{32}^{b} the transition rate coefficients between levels 2 and 3 caused by the ASE photons in the forward and backward directions, respectively; and Q_{3a} the collisional quenching rates from state 3 to all other states. Since we are only analyzing the effects caused by the ASE photons in the forward direction, W_{32}^{b} does not concern us in this analysis. Substituting Eq. (2.5) into (2.7) and solving Eq. (2.6) yields:

$$n_3(x) = \frac{W_{13} n_1(x)}{\frac{A_{32}\Delta\Omega_f}{B_{32}\Gamma / c\Delta\nu_{ASE}}[\exp(\frac{B_{32}\Gamma}{c\Delta\nu_{ASE}}\int_0^x n_3(x)dx) - 1] + (W_{34} + A_{32} + Q_{3a}) + W_{13}\frac{g_1}{g_3}} \tag{2.8}$$

As mentioned earlier, $n_3(x)$ can be non-smooth and discontinuous as its shape correlates to that of $n_1(x)$. The ratio between LIF signals obtained at low and high excitation energy (i..e, R_{True}) is then:

$$R_{True} = \frac{n_{3,L}(x)}{n_{3,H}(x)} \tag{2.9}$$

where $n_{3,L}(x)$ and $n_{3,H}(x)$ represent the population of state 3 caused by the excitation pulse with low and high energies, respectively. When Eq. (2.8) is substituted into Eq. (2.9) , the n_1(x) on the numerator of Eq. (2.8) is cancelled, and $R_{True}(x)$ depends on $\int_0^x n_{3,L}(x)dx$ and $\int_0^x n_{3,H}(x)dx$, which are first-order continuous due to the integration. As a result, $R_{True}(x)$ *is* smooth and continuous even when $n_1(x)$ is not.

The above analysis also illustrates that $\int_0^x n_3(x)dx$ is a fundamental and useful parameter in the analysis of ASE effects. However, in practice, $n_3(x)$ is usually neither the

target quantity to be measured nor directly available. The LIF signals (i.e., S_{LN} and S_{HN}) are directly available. For practical purposes, we denote $\int_0^x n_3(x)dx$ by X, and argue that it can be approximated by $\int_0^x S_{LN}(x)\cdot dx$ due to the following two considerations. First, under low excitation energy, $n_3(x)$ will be proportional to $n_1(x)$. As elucidated in Eq. (2.8) under weak excitation $n_3(x)$ approaches zero, causing $\int_0^x n_3(x)dx$ to approach zero too. Therefore, the first term in the denominator of Eq.(2.8) vanishes, leaving $n_3(x)$ to be proportional to $n_1(x)$. As a result, $\int_0^x n_3(x)dx$ is proportional to $\int_0^x n_1(x)dx$. Second, under weak excitation, the LIF signal is free from distortion and is therefore proportional to $n_1(x)$. The use of $X=\int_0^x S_{LN}(x)\cdot dx$ in the analysis of TPLIF measurements will be illustrated in the next subsection. The accuracy of approximating $\int_0^x n_3(x)dx$ with X obviously depends on the noise level in S_{LN}, and a thorough investigation merits a separate publication.

2.4.4 Performance of correction method

Based on the above understanding, the experimentally measured ratio can be fitted into a smooth curve with an inverted-bell shape to retrieve the true ratio. As shown in Panel (a) of Figure 2-6, the experimentally measured ratio (defined as $R_N=S_{LN}/S_{HN}$) may not be smooth or appear to be an inverted-bell curve due to the measurement noise, especially the noise in the signal obtained with low excitation energy. Smoothing and fitting this noisy ratio can retrieve the true ratio based on our argument above. Here we used a simple third-order spline method to obtain the fitted ratio, R_{Fit}. A more elaborate fitting method can improve the fitting quality. Panel (b) of Figure 2-6 shows the relative

error in the fitting (quantified by R_{Fit}/R_{True}), which shows that the fitting retrieved the ratio within ±4%.

After the ratio is retrieved, then it is used to correct the distorted LIF signal (by multiplying it). The results of such correction are shown in Figure 2-7. Panel (a) compares the corrected LIF signal (labeled as S_C) to S_{LN} and the ideal signal (labeled as S_{True}), the signal with neither noise nor distortion. Panel (b) illustrates that the noise in the corrected signal is within ±10%, which is significantly lower than that in S_{LN}. The noise in S_C consists of two parts. The first part is the noise in S_{HN}, which can be reduced by increasing the excitation energy. The second part is due to the discrepancy between the fitted ratio and the true ratio, as shown in Figure 2-6. A more elaborate fitting method can reduce this discrepancy, and a more accurate measurement at low excitation energy will also help.

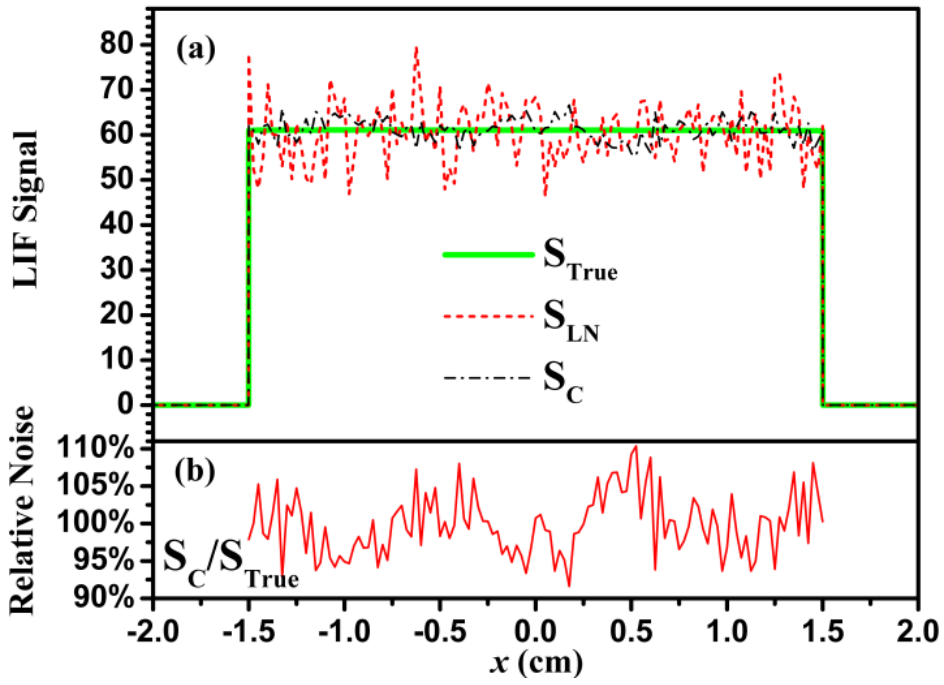

Figure 2-7. Panel (a) compares the corrected LIF signal to S_{LN} and S_{True}. Panel (b) illustrates that the noise in the corrected signal is significantly lower than that in S_{LN}

Figure 2-8 through Figure 2-10 show another set of sample results obtained under a different set of conditions. Panel (a) in Figure 2-8 shows the n_1 distribution (of H atom). This phantom distribution was taken from a measurement of a conserved scalar in a turbulent jet to simulate the fluctuations in both the large and small scale. The measurement domain was taken to be cylindrical with 2 cm length and 300 μm in diameter. The excitation pulse was assumed to be Gaussian with FWHM of 3.5 ns. The low and high excitation energies used were 0.059 and 0.169 mJ. The peak H number density was designed to be higher by ~10× than in the previous case, and therefore lower excitation energies were used. These parameters were chosen to illustrate that argument hold under different conditions. Panel (a) of Figure 2-8 shows S_{HN} scaled by a factor of 1/8 obtained according to Eq. (1) to illustrate the distortion caused by ASE. The S_{HN} is 8× stronger than S_{LN} in this case, which will cover the n_1 curve if shown. Panel (b) of Figure 2-8 shows the ratio of the LIF signal from low and high excitation energies. As argued above, the ratio is a smooth curve with an inverted-bell shape. Panel (a) of Figure 2-9 shows the ratios between of LIF signals. Note that Figure 2-9 used the new parameter $X = \int_0^x S_{LN}(x) \cdot dx$, whose units will be the units of the LIF signal (photons per pixel) multiplied by the length (cm). For the analysis of the top-hat distribution, X is equivalent to x. Since the physical meaning for R_N, R_{True} and R_{Fit} are unchanged, we use the same notation for ratios as functions of X. Similar to the results shown in Figure 2-6, a third-order spline fit of R_N was used to approximate R_{True}. The relative error of this fit was shown in Panel (b) to be within ±4%. Finally, Panel (a) of Figure 2-10 shows the comparison of the corrected LIF signal to S_{LN} and S_{True}, and Panel (b) illustrates that the relative error in the corrected signal. The relative error is within ±10% in the region (0.7

< x < 1.3 cm) where the n_1 is relatively high, in contrast to ±30% in S_{LN} in the same region. In region where n_1 is low, the relative error is large due to the large noise in both S_{LN} and S_{HN} in these regions. As mentioned above, increasing the excitation laser pulse can help to reduce errors in these regions.

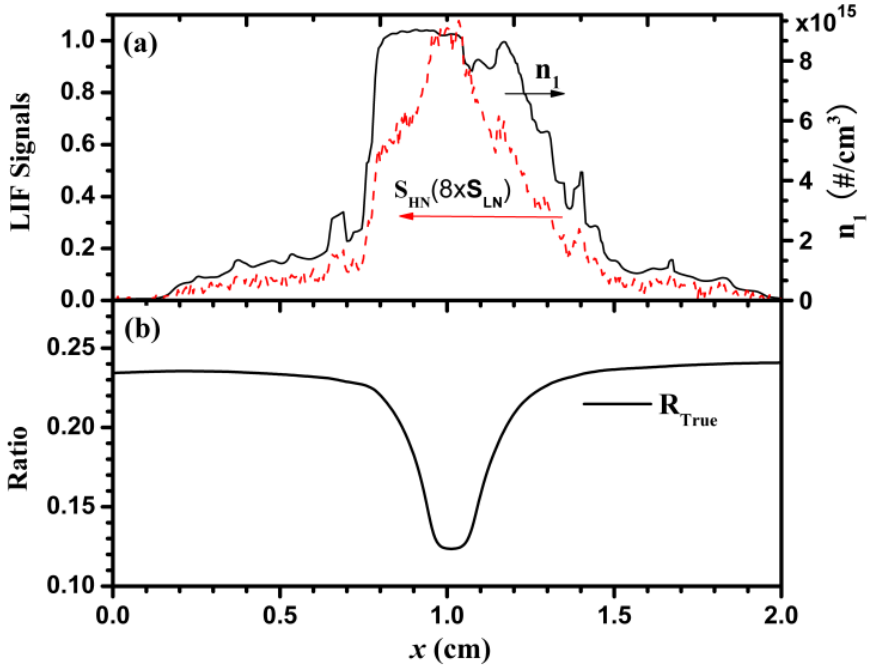

Figure 2-8. Panel (a) illustrates that the phantom n_1 distribution used and the distortion caused by ASE. Panel (b) illustrates that the shape of the ratio is insensitive to the n_1 distribution and the excitation energies.

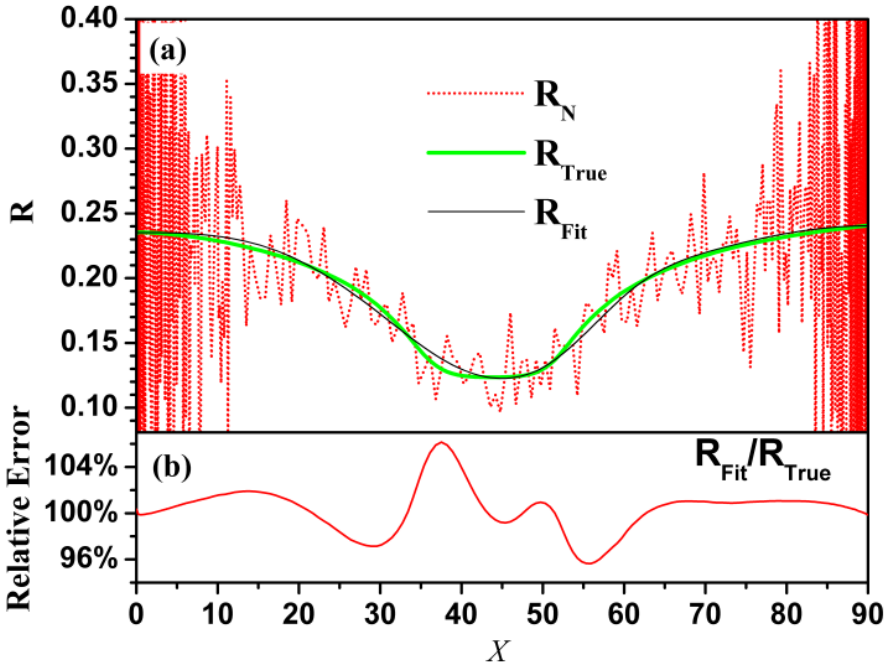

Figure 2-9. Panel (a): the ratio between the LIF signals obtained at low and high excitation energy. Panel (b). the relative error in the fitted ratio.

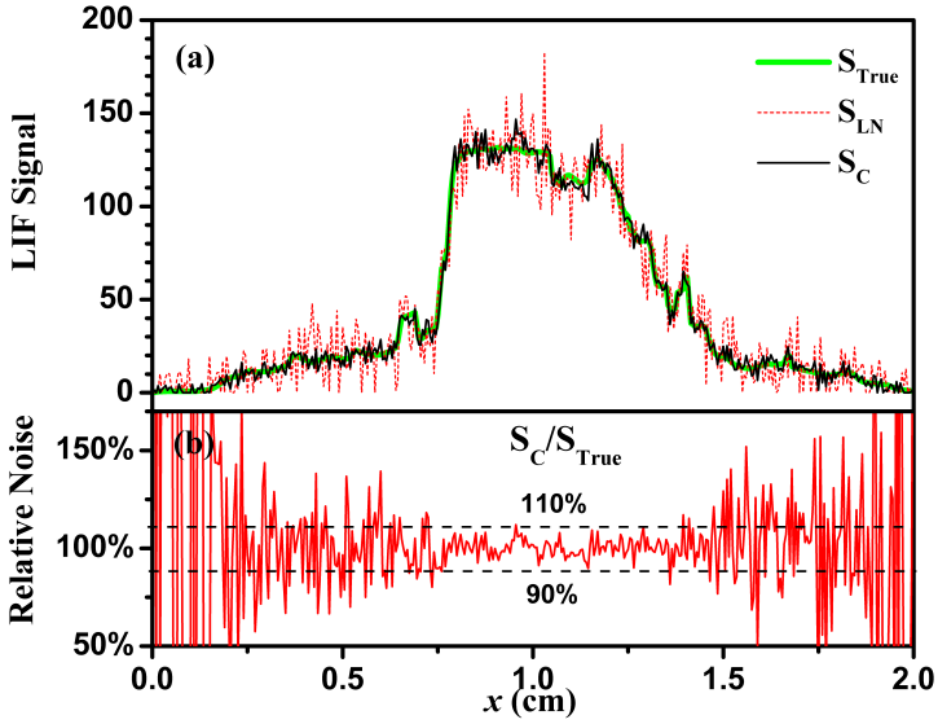

Figure 2-10. Panel (a) compares the corrected LIF signal to S_{LN} and S_{True}. Panel (b) illustrates that the noise in the corrected signal is significantly lower than that in S_{LN} .

Thus far, we have described the correction method, its physical background, and its demonstration on two distributions. For these two specific distributions, the correction method has been shown to reduce both noise and distortion. To systematically analyze its applicability and performance, we need to quantitatively define noise and distortion. Here we define noise as:

$$Noise = \frac{1}{L}\int_L \frac{|S_{LN} - S_L|}{|S_L|}dx \quad \text{or} \quad \frac{1}{L}\int_L \frac{|S_{HN} - S_H|}{|S_H|}dx \tag{2.10}$$

where L represents the measurement domain. Eq. (2.10) essentially defines a noise averaged in the measurement domain. Distortion is defined as:

$$Distortion = \frac{1}{L}\int_L \left|\frac{S_L}{An_1} - 1\right|dx \quad \text{or} \quad \frac{1}{L}\int_L \left|\frac{S_H}{Bn_1} - 1\right|dx \tag{2.11}$$

This definition quantifies the average deviation of the noise-free measurements (S_L or S_H) relative to n_1. The constants, A and B, in the equation are normalization factors determined according to:

$$\int_L S_L^2 dx = \int_L (A \cdot n_1)^2 dx \quad \text{and} \quad \int_L S_H^2 dx = \int_L (B \cdot n_1)^2 dx \tag{2.12}$$

These definitions need to be modified for the corrected signal (S_C), because S_C contains both the true signal and the noise. Here, we use $S_H \cdot R_{Fit}$ to represent the true signal in S_C, and noise and distortion are defined correspondingly as:

$$\text{Noise} = \frac{1}{L}\int_L \frac{|S_C - S_H \cdot R_{Fit}|}{|S_H \cdot R_{Fit}|}dx \tag{2.13}$$

$$\text{Distortion} = \frac{1}{L}\int_L \left|\frac{S_H \cdot R_{Fit}}{C \cdot n_1} - 1\right|dx \tag{2.14}$$

The constant, *C*, in the equation is again a normalization factor determined according to:

$$\int_L (S_{H} \cdot R_{Fit})^2 dx = \int_L (C \cdot n_1)^2 dx \tag{2.15}$$

With these definitions, simulations were made for many cases under various conditions, including n_1 distribution, excitation pulse energy, geometry, etc. The n_1 distributions used were specifically chosen to represent a wide range of flows. For each case, 1) the LIF signals at low and high excitation energies were simulated according to Eq. (2.1) , 2) then the correction method was applied to each case using the simulated signals, and 3) the noise and distortion of the simulated signals (S_{LN} and S_{HN}) and the corrected signal (S_C) were calculated according to Eqs. (2.10) - (2.15). Figure 2-11 shows the results obtained for 150 cases. The large red symbols in Panel (a) of Figure 2-11 correspond to the noise and distortion for the n_1 distribution shown in Figure 2-10; and the symbols in Panel (b) correspond to those of the top-hat distribution shown in Figure 2-5. As shown here, the correction method reduced both the noise and distortion for all these cases. Note that even though the noise in S_C was reduced in all cases compared to that in S_{LN}, the noise of S_C appears to be higher than that in S_{LN} for some cases because Figure 2-11 does not show the corresponding relationship among the cases. For example, the arrow in Panel (a) illustrates a corrected signal and the S_{LN} that it corresponds to. Also note that for some cases, the n_1 distributions used have some regions with low values, like the two sides of the distribution shown in Figure 2-10. The noise in these regions was exceedingly high, causing the high average noise seen on Figure 2-11. In practice, measurements made in these regions are usually discarded due to the unacceptable low SNR.

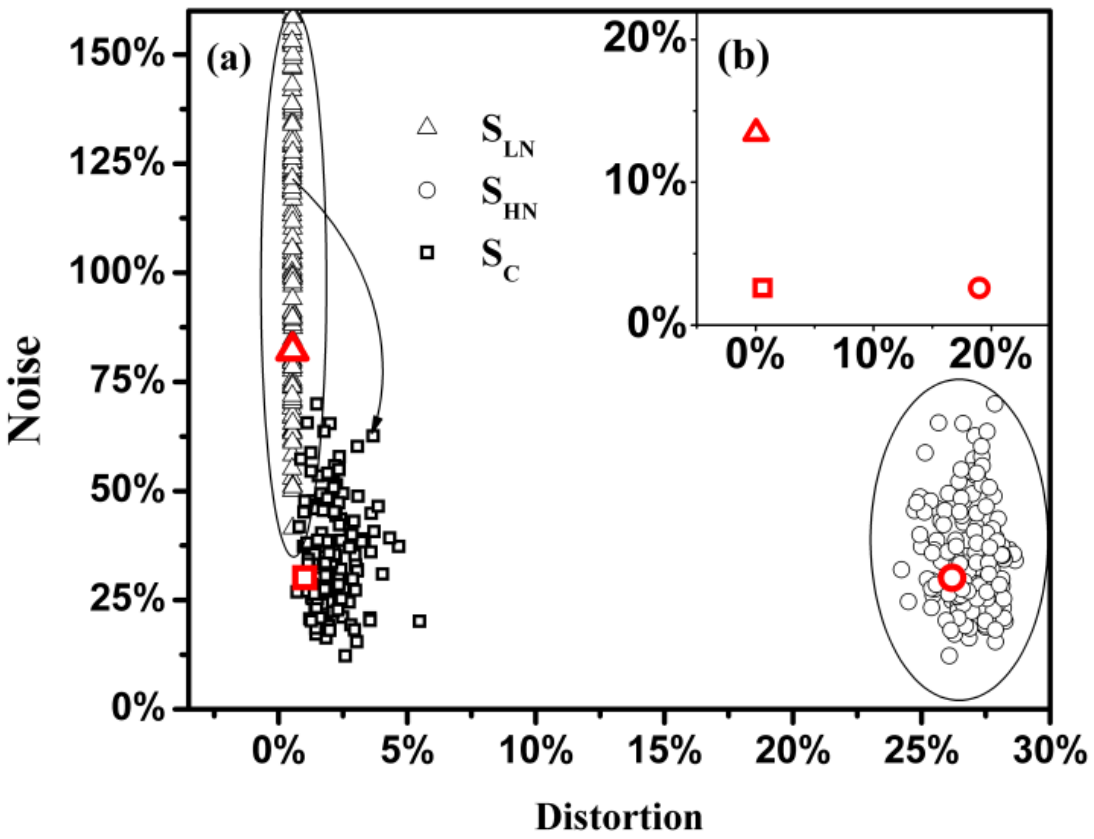

Figure 2-11. Performance of the correction method simulated for various distributions. The large red symbols in Panel (a) correspond to the noise and distortion for the n1 distribution shown in Figure 2-10; and the large red symbols in Panel (b) correspond to those of the top-hat distribution shown in Fig. 5.

In summary, this section describes the correction method and its physical background. Extensive numerical simulations were conducted to evaluate the performance of the correction method, and the method was demonstrated to be able to reduce noise and distortion in a wide range of conditions.

2.5 Summary

This chapter examined the effects of ASE in TPLIF measurements using a MC model. The ASE effects represent a major challenge to the application of TPLIF as a flow diagnostics that is more difficult to correct than quenching due to its non-linear and non-local nature than quenching and ionization. The ASE effects cause distortion to the target

LIF signal, the distortion depends nonlinearly on a range of parameters (e.g., the number density of the target species, laser excitation energy, temporal and spatial profile of the excitation pulse, etc.), and the distortion at one location depends on conditions at other locations.

A correction method was developed and demonstrated to correct for the distortion caused by ASE effects. The method was based on a physical understanding of the ASE effects, i.e., the ratio between the LIF signal obtained at low and high excitation energies should have a smooth shape, which is insensitive to experimental parameters. Based on this physical understanding, the correction method uses two LIF measurements, one with low SNR (signal-to-noise ratio) and negligible ASE distortion and another with high SNR but significant distortion, to generate a faithful measurement with high SNR. Extensive simulations were performed to evaluate the performance of this method, demonstrating its ability to reduce noise and distortion in TPLIF measurements across a wide range of conditions. We expect this method to be a valuable tool for the application of TPLIF techniques in flow diagnostics.

Chapter 3 3D Hyperspectral Tomography (HT)

3.1 Background

The study of reactive flows continues to challenge diagnosticians with the need for non-intrusive techniques that can provide quantitative measurements with adequate temporal and spatial resolution [58]. Such measurements have been repeatedly shown to be invaluable for the validation of existing models and also for the inspiration of new models. These techniques are furthermore desired to be robust and suitable for *in situ* monitoring and control purposes in practical combustion and propulsion systems to improve their efficiency and performance [2].

Among the properties important for reactive flows, temperature and concentration of chemical species are two most important ones; and the corresponding developments of diagnostic techniques have attracted a tremendous amount of research efforts. This chapter reports a 3D laser diagnostic that can measure two-dimensional (2D) distribution of temperature and concentration of water vapor (H_2O) simultaneously at high-speed. The HT technique utilizes multiple line-of-sight-averaged measurements of the absorption spectra of H_2O vapor to infer the distribution of temperature and H_2O concentration.

Here we have to limit the review of related work to recent efforts that aim at high-speed and 2D spatial imaging of temperature and chemical species for two reasons. First, a complete survey, even a brief one, will be beyond the scope of this current research because of the volume of past literature. Second, there already exist excellent monographs [1, 59] and dedicated reviews [58, 60] that provide a thorough discussion of past research in the non-intrusive measurement of temperature and chemical species.

For 2D spatial measurement of the concentration of chemical species, the well-established technique is planar laser-induced fluorescence (PLIF) [1]. The temporal resolution of PLIF is largely driven by the availability of high-speed lasers, cameras, and intensifiers. With such hardware becoming commercially available recently, multi-kHz PLIF systems have gradually become at more and more researchers' disposal [61-63]. Customer-built laser systems can further extend PLIF measurements to tens of kHz [64, 65], comparable to that of the HT technique reported here. The spatial resolution of PLIF is typically well below a millimeter, significantly superior to the HT technique demonstrated in this current research. Note however that 1) the spatial resolution of the HT technique is fundamentally limited by the size of the laser beam and can be dramatically improved, and 2) our current implementation of the HT technique essentially trades spatial resolution for the field-of-view (FOV). The spatial resolution can be improved by decreasing the size of the FOV, a trade-off that PLIF faces too.

For 2D measurement of temperature, Rayleigh scattering represents a well-established technique [1]. The comparison between Rayleigh scattering and the HT technique is similar to that between PLIF and HT. The temporal resolution of Rayleigh scattering is again largely driven by the availability of hardware, and can reach comparable level as reported here. The spatial resolution of typical Rayleigh scattering is superior to that of the HT technique reported here, and trade-off between spatial resolution and the size of the FOV applies to Rayleigh scattering too.

Comparison of HT to PLIF and Rayleigh scattering in other aspects (besides temporal and spatial resolution and the FOV) provides further motivation for the HT technique. For example, quantitative interpretation of PLIF measurements requires independent

information of temperature and local quenching rates, which can be difficult or even impossible to obtain in practical reactive flows. The Rayleigh signal depends on local gas composition, which can make the signal indecipherable in reactive flows. Furthermore, Rayleigh signal is relatively weak because of its non-resonant and elastic nature. As a result, conventional Rayleigh scattering is susceptible to interference due to particulate/droplet scattering and surface reflection, restricting its practical applications, and laser diagnosticians have been investigating techniques such as filtered Rayleigh scattering [66] to overcome these issues. Lastly, the laser equipments involved in PLIF and Rayleigh scattering are typically not fiber coupled, requiring their implementation to be in close proximity to the target test rig. Such requirements often pose significant challenges in practice because of the harsh environment created by combustion and propulsion systems, and these challenges are further compounded by the relatively bulky size of the laser equipment involved with PLIF and Rayleigh techniques.

The HT technique described in this chapter addresses these practical issues mentioned above. The HT technique provides simultaneous temperature and H_2O concentration measurements, with no requirement of other additional measurements or calibrations. The technique is fully fiber coupled, portable, and robust for practical applications. These advantages will become evident when the experimental arrangement is described below. In the next section, we briefly introduce the background of absorption tomography and the mathematical formulation of the HT technique.

The HT technique combines the use of tomography with hyperspectral absorption spectroscopy to extend the capabilities of traditional absorption-based diagnostics. Compared with previous work on absorption-based tomography, the HT technique

exploits the spectral information at a large number of absorption transitions whereas previous work relied on spectral information at a limited number of transitions (typically one or two) [67-71]. Hence, the HT technique essentially adds wavelength as a new dimension to the traditional tomography problem, which primarily focused on the use of spatial information [72]. Our study thus far [4, 17, 25, 73, 74] has suggested that the increased spectral information content offer several important advantages including the reduction of the number of projections required for a faithful tomographic reconstruction, improved resistance to measurement noise, and the ability to obtain simultaneous temperature and concentration imaging.

The concept, mathematical formulation, numerical evaluation, demonstration, and validation of the HT technique have been detailed in a series of previous work. The concept and mathematical formulation were introduced in [25, 73], the numerical evaluation was described in [25, 74], a prototype HT sensor was demonstrated in a laboratory flame in [4], and the validation of the full-scale sensor used in this research was reported in [17]. With these previously documented efforts, this section intends only to provide a brief summary of the physics and mathematics of HT to facilitate the discussion in the rest of the dissertation.

Figure 3-1 depicts the HT problem. A hyperspectral laser beam is directed along the line of sight, denoted by l, to probe the domain of interest as shown in the left panel. Absorption by the target species will attenuate the probe laser beam, and the absorbance at a certain wavelength (e.g., λ_i) generally contains contributions from multiple transitions centered at various wavelengths (including that centered at λ_i itself), as schematically shown in the right panel. Here, we use $p(L_j, \lambda_i)$, termed a projection, to denote the

absorbance at a projection location L_j and a wavelength λ_i. The projection, $p(L_j, \lambda_i)$, is expressed by the following integral:

$$p\left(L_j,\lambda_i\right)=\int_a^b\sum_k S\left(\lambda_k,T\left(\ell\right)\right)\cdot X\left(\ell\right)\cdot\Phi\left(\lambda_k-\lambda_i\right)\cdot P\cdot d\ell \tag{3.1}$$

where a and b are the integration limits determined by the line of sight and the geometry of the domain of interest, $S(\lambda_k, T(l))$ is the line strength of the contributing transition centered at a wavelength λ_k and depends nonlinearly on temperature (T); $T(l)$ and $X(l)$ are the temperature and mole-fraction profile of the absorbing species along the line of sight, respectively; F is the Voigt lineshape function; and P is the pressure, assumed to be uniform. The summation runs over all the transitions with non-negligible contributions. In this research, the domain of interest is discretized by superimposing a square mesh in the Cartesian coordinate, as shown in the left panel of Figure 3-1; and the integration in Eq. (3.1) is also discretized accordingly.

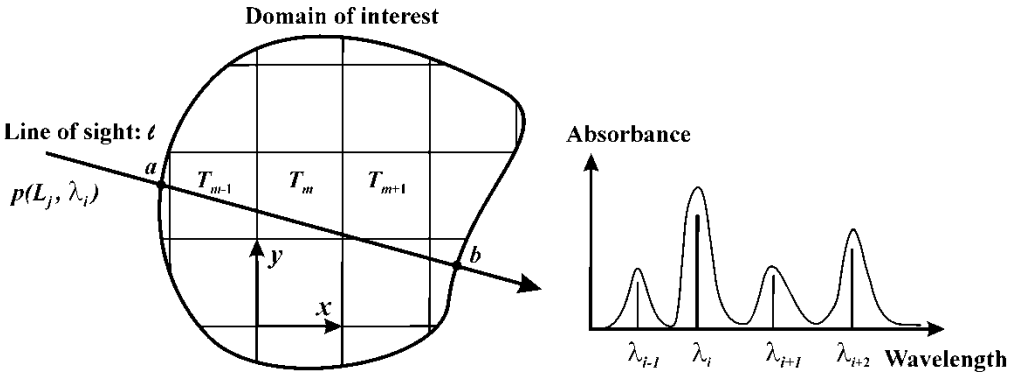

Figure 3-1. The mathematical formulation of the hyperspectral tomography problem.

The HT problem seeks to determine the distributions of T and X over the discretized domain with a finite set of projections as described in Eq. (3.1). We developed a method to cast the inversion problem into a nonlinear optimization problem, where the T and X distributions are retrieved by minimizing the following function:

$$D(T^{rec}, X^{rec}) = \sum_{j=1}^{J} \sum_{i=1}^{I} \frac{[p_m(L_j, \lambda_i) - p_c(L_j, \lambda_i)]^2}{p_m(L_j, \lambda_i)^2} \tag{3.2}$$

where $p_m(L_j, \lambda_i)$ denotes the measured projection at a location L_j and a wavelength λ_i; $p_c(L_j, \lambda_i)$ the computed projection based on a reconstructed T and X profile (denoted by T^{rec} and X^{rec}, respectively); and J and I the total number of wavelengths and projection locations used in the tomography scheme, respectively. This function, D, provides a quantitative measure of the closeness between the reconstructed and the actual temperature and concentration profiles. The contribution from each wavelength to D is normalized by the projection at this wavelength itself, such that projections measured at all wavelengths are weighted equally in the inversion. In an ideal case where the measurements are noise free, D reaches its global minimum (zero) when T^{rec} and X^{rec} match the actual profiles.

The formulation in Eq. (3.2) allows the flexible incorporation of available *a priori* information via regulation. For instance, in practice, the T and X distribution sought are non-negative, bounded, and smooth to a certain degree because of thermal and mass diffusion. All such information is included in minimizing Eq. (3.2) [25, 74]. More specifically, the non-negativity and boundedness regularizations are incorporated in the minimization algorithm (the simulated annealing algorithm), and the smoothness regularization is implemented by modifying the target function D into:

$$F(T^{rec}, X^{rec}) = D(T^{rec}, X^{rec}) + \gamma_T \cdot R_T(T^{rec}) + \gamma_X \cdot R_X(X^{rec}) \tag{3.3}$$

where R_T and R_X are the regularization factors for temperature and concentration, respectively; γ_T and γ_X are positive constants (regularization parameters) to scale the magnitude of R_T and R_X properly. More details of the use of regularization factors, the

determination of the optimal regularization parameters, and the simulated annealing algorithm can be found in [25, 73, 74]. Finally, the solution of the minimization problem described in Eq. (3.3) provides the tomographic reconstruction of the T and X distributions.

It is not trivial to find a robust algorithm to minimize the nonlinear function F, defined above, due to the complexity and high non-linearity of the hyperspectral problem. Take a 15×15 problem for example, there will be 450 variables in F (225 unknown Ts and 225 unknown Xs), and the number of variables increases with the degree of discretization. Function F exhibits a great many local minima and we have observed that the number of local minima also increases rapidly with the degree of discretization since the problem becomes more complex with more unknowns. These characteristics of F pose significant challenges to minimization algorithms using the derivative information, because these algorithms will have a great change to be trapped in one of the local minima and thus unable to provide the correct T and X reconstruction. Since the HT problem is non-linear, iterative, deterministic algorithms such as algebraic reconstruction technique (ART) will fail in solving HT problem. A powerful algorithm that can address complex, non-linear problem is strongly desired.

3.2 Simulated annealing algorithm

The SA algorithm, introduced in 1983 [75], was initially developed for minimizing large scale combinatorial problems. The algorithm was extended to continuous problems shortly afterwards [76, 77]. The algorithm has been extensively demonstrated in various studies as an effective algorithm for large scale and complicated problems, with the global minimum hidden among numerous confusing local minima [76, 78-80]. The SA

algorithm roots from an analogy to the way liquids are annealed, i.e., cooled slowly to arrive at a low energy and crystallize. During the annealing process, the energy of the liquid is lowered gradually such that the system can escape from a local energy minimum due to random thermal fluctuations. On the contrary, if cooled rapidly (i.e., quenched), the liquid is usually forced into a state of local energy minimum. In function minimization, the value of the target function (*f (x)*) is the counterpart of the energy of the liquid under annealing; and a parameter, *TSA*, is introduced to be the counterpart of the temperature of the liquid. The random thermal fluctuation is implemented by the following Metropolis criterion:

if $\Delta f = f(x_{New}) - f(x_{Old}) \geq 0,$ accept x_{New}

else accept x_{New} with probability $P_{SA} = \exp(-\frac{\Delta f}{T_{SA}})$ (3.4)

where x_{Old} and x_{New} represent the variables of f (either continuous or discrete) in the previous and current iteration. Eq. (3.4) elucidates the essence of the SA algorithm: a new solution (x_{New}) is always accepted if it results in a lower f (energy); but a new solution (a seeming worse-off solution) is not always rejected if it results in a higher f , and is instead accepted with a certain probability p_{SA} (random thermal fluctuation). The probability, p_{SA}, decreases with T_{SA}. The SA algorithm converges to the global minimum of f by "annealing" it, i.e., by gradually reducing T_{SA}. In contrast, deterministic minimization algorithms based on derivative gradient information always accept a new solution if it results in a lower f , and reject it otherwise. Consequently, these algorithms cannot escape a local minimum once they enter it. The diagram shown in Figure 3-2 illustrates the above discussions. The SA algorithm starts by initializing its parameters (the initial value of the variables, the initial T_{SA}, the termination criterion, etc.). The remainder of the

algorithm is composed of a loop. The loop starts with repeating the following steps for N_T times: 1) a new point of the variables (x_{New}) is generated, and 2) the value of the function at the new point is evaluated and the Metropolis criterion is applied. Then the termination criterion is examined; and, if not reached, T_{SA} is reduced and a new iteration of the loop is executed at the reduced T_{SA}. The above discussion describes the generic structure of the SA algorithm. In practice, many variations of the algorithm are implemented. These implementations mainly vary in the way of reducing T_{SA}, determining the initial temperature, and generating x_{New} [76, 77, 81].

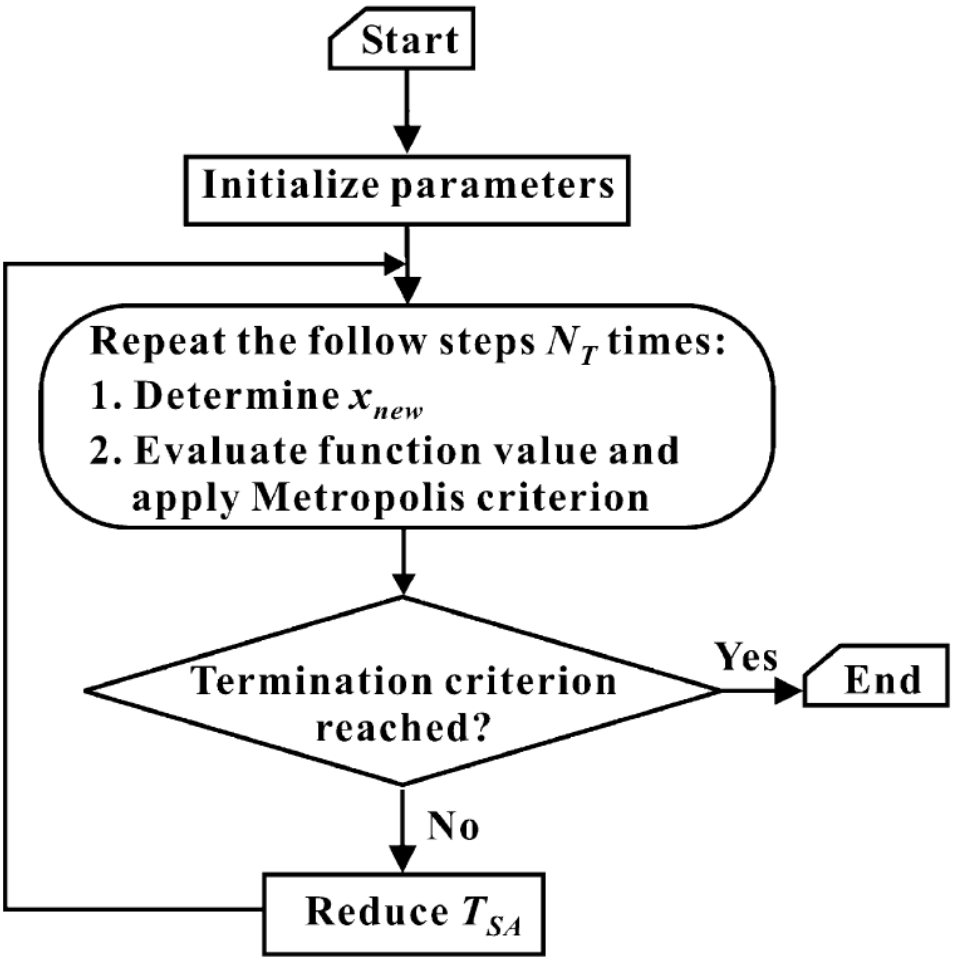

Figure 3-2. An Illustration of the structure of the SA algorithm.

3.3 Experimental setup

A measurement campaign was conducted to apply the HT technique to the exhaust stream of the augmenter-equipped J85-GE-5 gas turbine engine located at the University of Tennessee Space Institute (UTSI). This engine is operated by personnel affiliated with the Air Force Arnold Engineering and Development Center (AEDC) and has been developed and used as a test bed for the evaluation of advanced diagnostic techniques [82].

An overview of the experimental arrangement is shown in Figure 3-3. The UTSI test facility consists of a high-bay room which contains the J85 engine and a control room located in an adjacent building. The HT sensor was installed on a tomography frame, which held the sensor at the exhaust plane of the engine as shown. The HT sensor utilized 32 laser beams, generated by a laser system consisting of three independent Fourier-domain mode-locked (FDML) lasers [83]. These lasers were placed in the control room, and their operation was synchronized and controlled by a master clock and three function generators (FG). The laser beams generated were then delivered to the measurement location by single-mode fibers (SMF), with length of ~60 m. A 4×32 multiplexer was used to combine and distribute the laser beams over the required 32 channels needed for the experiment. The multiplexer was placed near the engine to minimize the length needed for the test-section delivery fibers. A total of 30 laser beams coming out of the multiplexer were used for the actual measurements: 15 of them installed to probe the measurement plane horizontally and 15 vertically (more details shown in Figure 3-4), forming a square mesh of 225 grid points over which the tomography reconstruction was performed according to the method described in Section 3.2. The remaining two laser

beams coming out of the multiplexer were used for laser referencing: one of them was sent to a photodiode to record the laser intensity and the other directed to a Mach-Zehnder interferometer to monitor the wavelength scan. The data-acquisition system was placed near the engine (~15 m away from the engine) to minimize the required length of coaxial cable. Cost was the primary motivation for minimizing the length of the fiber and cable.

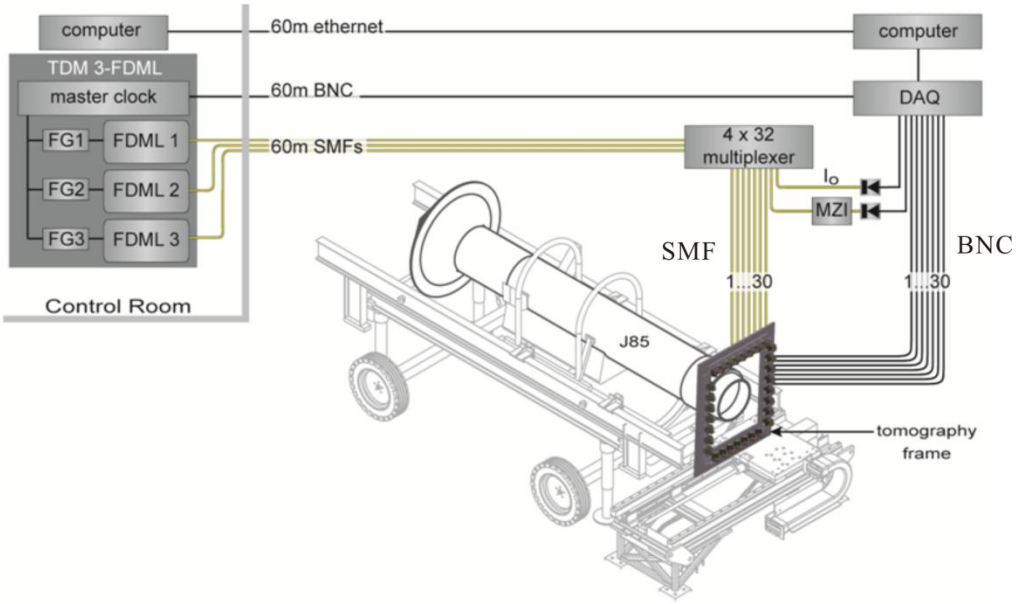

Figure 3-3. Overview of the experimental setup with a 30-beam HT sensor applied at the exhaust stream of a J85 engine. The laser system (labeled as TDM 3-FDML) was operated from the facility control room and 60-m-long optical fibers were used to transmit the laser signals to the engine location. A 4×32 multiplexer located near the engine was used to combine and split the three laser signals into 32 independent outputs. A customer-built tomography frame was mounted at the measurement location (the exit plane of the exhaust nozzle), holding the probe laser beams in position to create the 15×15 grid pattern for the tomographic reconstruction.

Figure 3-4 provides a more detailed illustration of the HT sensor and its installation. The 30 probe beams were installed on a customer-built aluminum frame, which was designed both to hold the probe beams at the measurement plane and also to protect the electro-optic components from the high-temperature and -velocity combustion flow. Panel (a) shows the configuration of the probe beams: 15 installed horizontally and 15

vertically, with a spacing of 38.3 mm (1.5 inches) between probe beams. Panel (b) shows a photograph of the frame and the optical components (with a measured temperature distribution superimposed in the middle). The frame consisted of a square base plate with an opening sized to match the diameter of the exit shroud of the J85 engine 45.72 cm (18 inches). On each of the four sides of the frame, two sets of rails were fabricated and used to mount the fiber collimators and detectors. Each of the 30 probe beams consisted of a laser delivery fiber (Corning SMF-28), a collimating lens, free-space path across the test section, a collection lens, and a photodetector. The collimating lens used was a 1.25-mm-diameter plano/convex fused silica rod-shape lens with a designed working distance of 92 mm at a wavelength of 1310 nm. The plano side of the collimating lens was fused directly to the end of the SMF, and the entire collimating assembly was held in a kinematic stage for beam-alignment purposes. A plano-convex lens with a diameter of 25.4 mm was used to collect and focus light onto the photodetector (Thorlabs PDA10CF, with an active area with 0.5-mm diameter). Panel (c) depicts the location of the measurements plane in the exhaust and a sample measurement of the 2D distribution of the temperature measured at this location. The analog voltage signal from the detector was transferred via coaxial cable to a National Instruments PXI-5105 data-acquisition board for digitization and subsequent data storage on a personal computer.

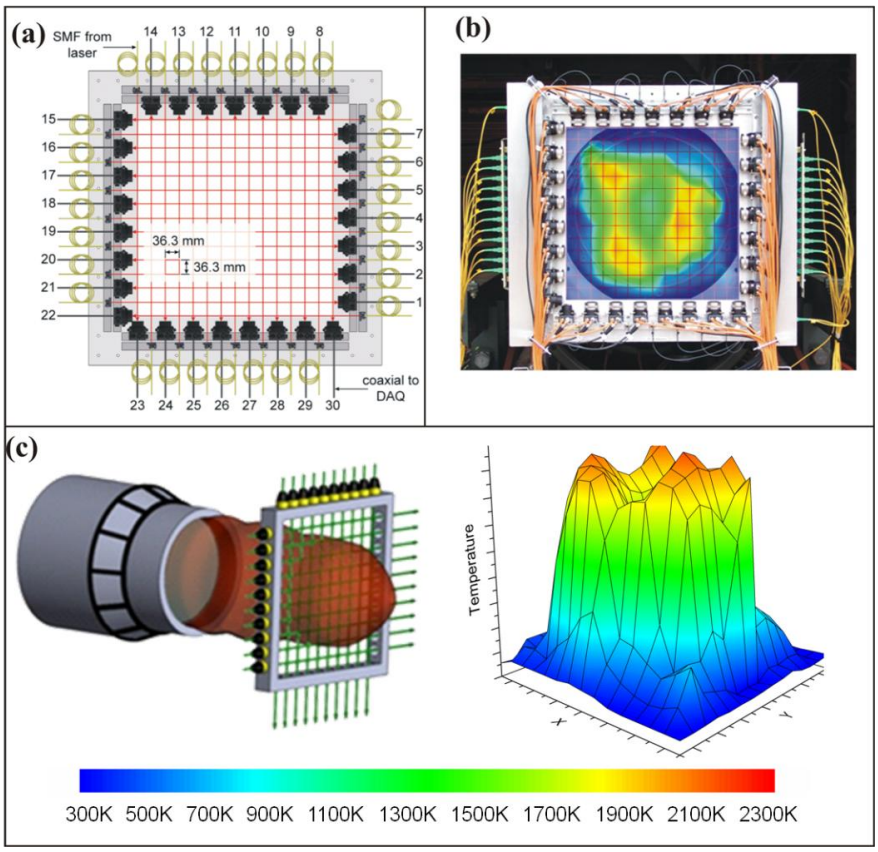

Figure 3-4. Schematic representation of the optical test section hardware. A 15 x 15 crossing beam grid pattern with a 36.3-mm beam spacing was used for the tomographic reconstruction. Light from the laser was delivered to the test section via single-mode fibers (SMF) and was collimated and transmitted across the engine exhaust flow. 1-in collection lenses were used on the receiving side and focused the laser light onto photodiodes. Panel (a): configuration of the probe beams. Panel (b): a photograph of the frame and the optical components overlaid by a sample reconstruction to illustrate the location of the flowfield. Panel(c): schematic of the location of the measurements plane in the exhaust and a sample measurement of the 2D distribution of the temperature measured at this location.

A key component in the HT sensor is the hyperspectral laser source, which enabled the measurement of a large number of absorption transitions across a wide spectral range at high repetition rate. The laser source chosen for this research was a time-division-multiplexed (TDM) combination of three FDML lasers, hereafter referred to as the TDM 3-FDML system. This system operates near 1350 nm to monitor H_2O vapor absorption features. TDM has been used in H_2O vapor absorption spectroscopy for years [84]. Recently developed TDM lasers for H_2O absorption spectroscopy offer enhanced

capabilities. For example, a recent TDM laser concept enabled rapid monitoring of numerous (10s to 100s) discrete spectral channels [85] and was successfully used to monitor gas temperature and H_2O and CH_4 concentrations in a high-pressure gas turbine combustor rig operated at the Air Force Research Laboratory (AFRL) [86].

Structurally, the three FDML lasers used in this research were virtually identical. Each was configured to output a high-repetition-rate (~ 50 kHz) wavelength sweep over a unique ~ 10 cm^{-1} spectral range. In our earlier work where one FDML laser was used for H_2O absorption spectroscopy for the first time [83], a single FDML was configured to sweep a much broader range (~150 cm^{-1}). By multiplexing 3 FDMLs in this research, we focused on three spectral regions of the H_2O spectrum with the highest temperature sensitivity to reduce the data-acquisition load relative to our initial work. Because the center wavelength and sweep range of each of the 3 FDMLs can be independently adjusted [87], the TDM 3-FDML source can be optimized for each test article of interest. For example, when the gas pressure within the test environment is high (e.g., 30 bar) the sweep range of each FDML is generally increased to allow more complete monitoring of the shapes of spectral features. When the gas temperatures within the test environment are confined to some limited range, the center wavelengths of the 3 FDMLs can be chosen to offer maximum temperature sensitivity within that range. In this research, the test gas was near atmospheric pressure, so we chose relatively narrow wavelength sweeps (~10 cm^{-1} each); the temperatures were expected to span 300–2300 K, so we chose features that maximized the overall temperature sensitivity over this wide range of temperatures, following an approach similar to that described in reference [88].

Because each FDML sweeps a ~10 cm^{-1} range, absorption baselines can be accurately determined along with *in situ* feature lineshapes. The latter capability reduces the need to rely on auxiliary measurements of gas pressure and offers the potential for gas pressure measurements in addition to the usual targets (gas temperature and H_2O mole fraction).

The TDM 3-FDML laser was designed for multi-beam tomographic measurements based on H_2O absorption spectroscopy. The three FDML cavity lengths were matched to within 3 cm (cavity lengths: ~3020 m) in order to operate the fiber Fabry-Perot tunable filters (FFP-TFs) at the same frequency: 50.24337 kHz (the overall repetition rate of the TDM 3-FMDL system). Because of the high number of output beams, each of the three FDML output signals was amplified with an external-cavity semiconductor optical amplifier (SOA) to compensate for the multiplexing loss (-15 dB for 32 fiber-coupled outputs, neglecting excess loss). Pulsing each of these SOAs at ~33% duty cycle facilitated time-division multiplexing of the 3 FDMLs and allowed selection of the middle of the blue-to-red sweep of each laser. The injection current to each external-cavity SOA was provided by an off-the-shelf diode laser controller (Wavelength Electronics, LDTC 2/2 E, 2-MHz modulation bandwidth). The gate signals to the diode-laser controllers were provided by a pulse generator (Berkeley Nucleonics Corporation, BNC555) that was locked with the three FFP-TF drive signal generators (FG, Agilent 33220A) to a synthesized clock generator (Stanford Research Systems, SRS CG635). The entire laser system was housed in a transportable 19-inch rack enclosure.

3.4 Results and discussions

Measurements were performed on the J85 engine under different conditions including ground-idle, full-military, and full-afterburner operation. Figure 3-5 shows a sample set

of the spectra measured by the TDM 3-FDML laser during one single scan under full-afterburner operation. Each panel shows the spectra measured by one FDML laser during that scan at two beam locations (illustrated by the red and blue arrows in the right panel). These two beams locations were chosen to represent a “hot beam” and a “cold beam, beams 4 and 22 illustrated by the red and blue arrow in the right panel, respectively. The hot beam (beam 4) passes through the center of the engine exhaust, along which the temperature distribution varies significantly more than that along the cold beam, which passes through the edge of the exhaust stream. As a result of such different temperature distributions, the spectra measured at the hot and cold beam locations also differ as shown in Figure 3-5. Such difference forms the basis for the tomographic reconstruction discussed in Section 3.2.

A smaller set of absorption transitions can be selected out of those monitored by the three FDML lasers, as shown in Figure 3-5, for two considerations. First, not all the transitions shown in Figure 3-5 are equally valuable for the tomographic reconstruction [89]. Second, consideration of computational cost also motivates the use of a smaller set of transitions [4], because the computational cost is approximately proportional to the number of transitions used in the tomographic reconstruction. In this research, we selected a total of 12 transitions out of those shown in Figure 3-5 according to the method described in [89] for the tomographic reconstruction. Absorption measured at these 12 selected wavelengths was then used as inputs to Eq. (3.3) to perform the tomographic inversion.

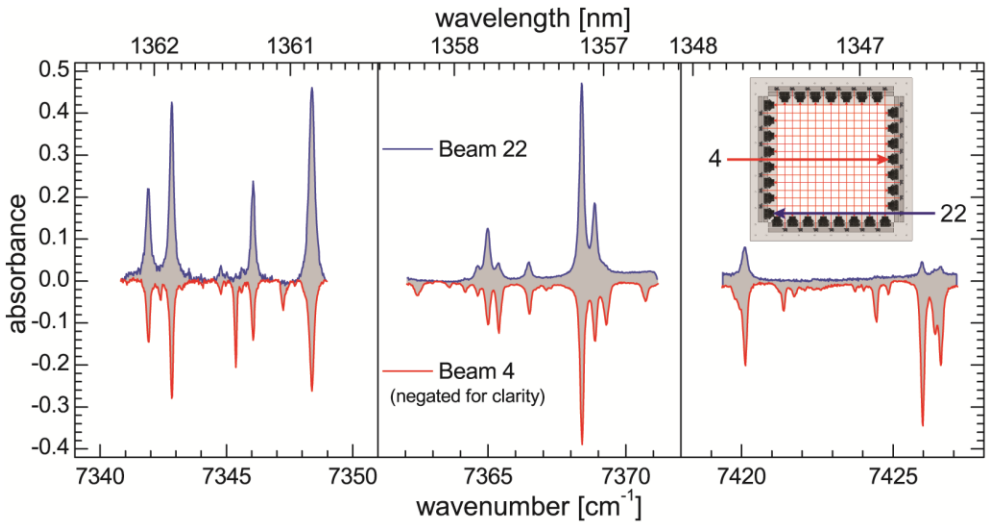

Figure 3-5. Absorption spectra measured during a single scan of the TDM 3-FDML laser operating at 50.24337 kHz (~20 microseconds). Each panel shows the spectra measured by one of the three FDML lasers.

Figure 3-6 shows a set of sample results of the temperature and H_2O mole-fraction distributions measured under representative conditions in the J85 engine. Under all conditions, the measurements were taken at 50 kHz; and the tomographic algorithm was applied to process the measurements frame by frame to obtain distributions of temperature and H_2O mole fraction. Under each representative operation condition (ground idle, full military, and full afterburner).

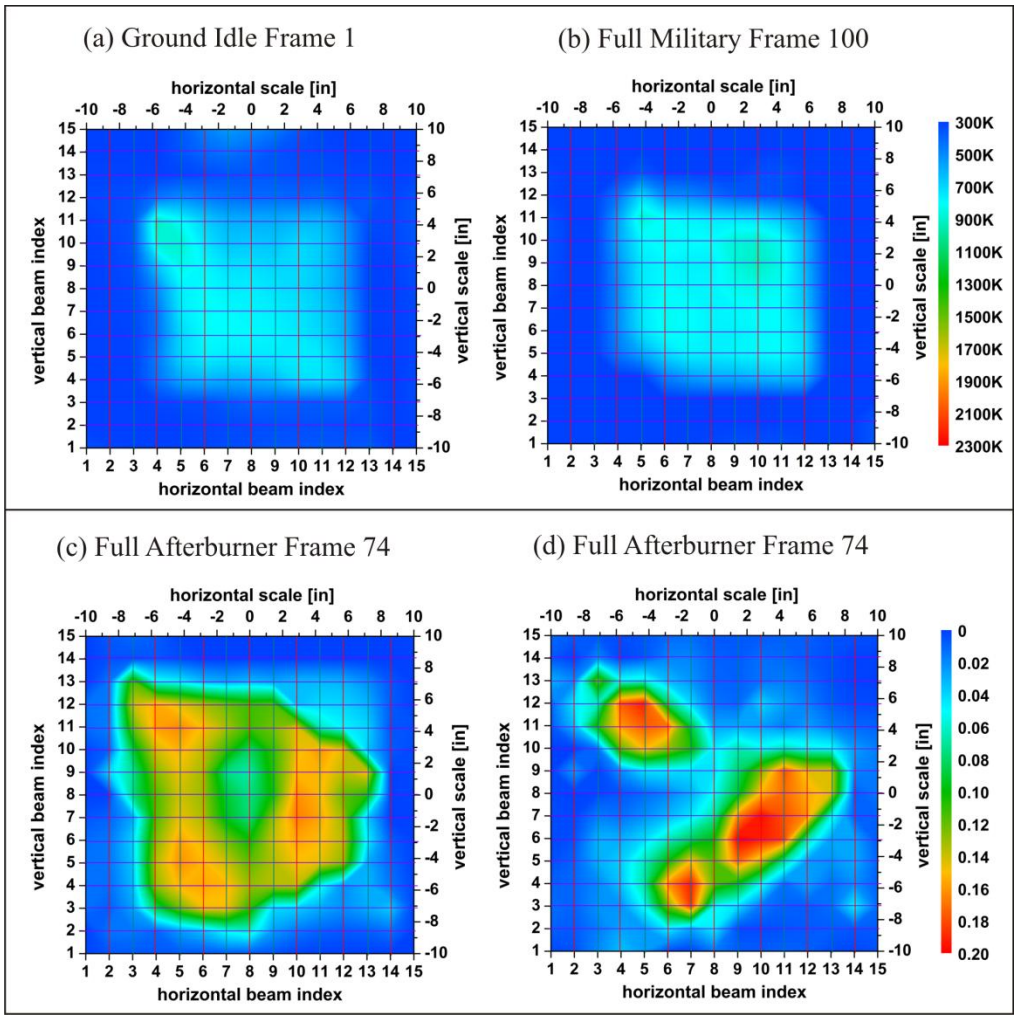

Figure 3-6. A set of sample results obtained in the J85 engine. Each panel shows one frame, arbitrary chosen out of 100 frames of measurements, corresponding to 2 ms of measurement duration. Panel (a): frame 1 of temperature distribution under ground-idle operation. Panel (b): frame 100 of temperature distribution under full military operation. Panel (c): frame 74 of temperature distribution full-afterburner operation. Panel (d): frame 74 of H_2O mole-fraction distribution under full-afterburner operation.

The reconstructions shown in Figure 3-6 were obtained based on a square domain of measurement, even though the flow field was circular. This work defined a square domain of measurement by the tips of the collimating lenses and the tips of the collection lenses, as shown in Panels (a) and (b) of Figure 3-4. This square region was then discretized into grids of size 36.3 × 36.3 mm as shown in Panel (a) of Figure 3-4 for the tomographic reconstruction.

As noted in the introduction, several key advantages of the HT technique were demonstrated in these applications in comparison to other well-established techniques such as PLIF and Rayleigh scattering. First, the HT technique extensively utilizes fiber technologies, which greatly facilitate its application in practical combustion devices and field measurements as depicted in Figure 3-3 and Figure 3-4. Second, the HT technique enables a temporal resolution that is comparable to planar techniques using state-of-the-art laser and camera techniques. Third, the HT technique, though unable to compete with planar techniques in terms of the spatial resolution, provides the ability to monitor a relatively large FOV. Based on these previous applications, with additional capital investment, it is relatively straightforward to add additional laser beams to enhance the spatial resolution. Because of these advantages, we expect the HT technique to play unique roles in the study of high-speed reactive flow, in the diagnosis of practical propulsion devices, and eventually in the active control and monitoring of such devices.

3.5 Summary

This research reports a new 3D laser diagnostic that can measure 2D distribution of temperature and H_2O concentration simultaneously with a temporal resolution of 50 kHz at 225 spatial grid points. To our knowledge, it is the first time that such measurement capabilities have been reported. The diagnostic technique leverages recent developments in hyperspectral laser sources and fiber technologies, so that 1) a large number of absorption transitions can be measured over a relatively wide spectral range with a rapid repetition rate, and 2) the probe laser can be split and delivered to perform measurements at multiple spatial locations. A mathematical formulation and a corresponding algorithm

have been developed to exploit the multi-spectral and multi-spatial information, yielding 2D tomography imaging of the temperature and H_2O concentration distribution.

The HT technique has been demonstrated in the exhaust plane of a practical aero-propulsion engine (General Electric J85). Simultaneous imaging measurement of the distribution of temperature and H_2O concentration were obtained at a rate of 50 kHz under different engine operation conditions. The application in a practical aero-propulsion engine demonstrated several unique advantages of the HT technique, including its robustness and ease of implementation in practical systems, and its ability to perform measurements across a relatively large FOV. These advantages are expected to contribute to some critical issues in aero-propulsion systems, such as combustion instability and thermal-acoustic coupling.

Chapter 4 4D Tomographic Chemiluminescence (TC)

4.1 Background

Chemiluminescence from combustion radicals (e.g., OH^*, CH^*, CO_2^*, and C_2^*) represents a unique diagnostic opportunity in reactive flows, both for fundamental study and practical deployment. Diagnostics based on chemiluminescence can be substantially simpler and easier to implement than other optical diagnostics, yet provide measurements which are otherwise challenging to obtain. Most combustion diagnostics require laser sources and/or external seeding, which are usually costly, cumbersome, or even infeasible [90, 91]. In contrast, diagnostics based on chemiluminescence bypass such requirements since chemiluminescence is emitted naturally in combustion processes. In spite of the simplicity, chemiluminescence provides information about key combustion quantities which are challenging to obtain, with the rate of heat release and local equivalence ratio being two notable examples. Both quantities are critical for the fundamental understanding of combustion instability, a phenomenon that can lead to reduced efficiency or even the destruction of gas turbines and aero-propulsion systems [92].

Here, we briefly review common techniques from our perspective to motivate chemiluminescence-based techniques. Existing techniques for the measurement of local equivalent ratio are typically based on 1) laser induced fluorescence (LIF) to track a fuel marker [91, 92], 2) Raman scattering to measure fuel concentration [91, 92], or 3) chemiluminescence from two combustion radicals (e.g., OH^* and CH^*) [92-94]. All three types of techniques have been relatively well-established, and have become standard diagnostic tools for combustion research. Both LIF and Raman techniques require high

power lasers. The fuel marker introduced may not faithfully track the fuel vapor due to its different physical and chemical properties than the fuel vapor [90, 95, 96]. Furthermore, the quantification of LIF signal is complicated due to specie- and temperature-dependent quenching rates. Application of Raman techniques is restricted to "clean" environment (free from particulates, soot, and background luminosity) due to the relative low signal level of Raman scattering [90, 91]. For the rate of heat release, existing techniques are typically based on 1) LIF measurements of two species which are the reactants of a reaction whose rate correlates with rate of heat release [97, 98], and 2) chemiluminescence measurements of radicals (typically OH^* and CH^*) whose concentration correlate with rate of heat release [94, 99]. The simultaneous LIF measurements of two flame species again require high power lasers, and the quantitative interpretation of LIF measurements is non-trivial due to species- and temperature-dependent quenching rates.

The above discussion motivates the consideration of chemiluminescence for measuring local equivalence ratio and rate of heat release. Compared to LIF- or Raman-based techniques, chemiluminescence does not require laser sources and the interpretation of signal is relatively straightforward. These advantages significantly simplify the alignment and implementation, and are especially appealing for application in practical systems.

The limitations of chemiluminescence-based techniques have also been well recognized. Chemiluminescence signal is also difficulty to quantity and its applicable range has been extensively investigated in terms of temperature, pressure, equivalence ratio, and strain rate [92, 94, 100-102]. Out of all the limitations, the lack of spatial

resolution perhaps represents the most important limitation of chemiluminescence-based techniques.

Therefore, this chapter addresses the issue of spatial resolution of chemiluminescence-based techniques. Chemiluminescence is naturally emitted from the entire volume of combustion zones, resulting in its line-of-sight averaged nature. In contrast, LIF- or Raman-based techniques utilize signals artificially generated by laser illumination, and the illumination volume provides well-defined spatial resolution. Since spatially resolved measurements are highly desired for model validation and development, research efforts have been invested by several groups to achieve spatial-resolved chemiluminescence measurements. These efforts can be broadly divided into two approaches.

The first approach approximates point-measurement of chemiluminescence by designing the collection system so that only the chemiluminescence emitted from a well-defined and relatively small volume is collected to the detector. This approach seems to originate from an intrusive probe first demonstrated in 1991 [103]. Non-intrusive implementations subsequently have been demonstrated using Cassegrain telescope optics [92-94, 100, 104, 105]. These implementations have achieved nominal spatial resolution on the order of 100-200 μm in diameter and 800-1600 μm in length [92, 104]. Extension of this pointwise approach to multiple dimension measurement could be accomplished by scanning the probe if the target flame is steady, or by employing multiple probes simultaneously.

The second approach involves combining chemiluminescence with tomography to obtain spatially-resolved measurements in two-dimensional (2D) or 3D. Compared to the

above pointwise approach, the tomographic chemiluminescence (TC) approach can provide 2D or 3D measurements directly (i.e., without scanning), thusly providing valuable or even critical structural information of turbulent flames. Early efforts, limited by hardware, typically relied on sequentially recorded projections or a few number of simultaneously projections to obtain 2D measurements [106, 107]. Recent advancements in digital cameras, fiber optics, and computing technologies have provided the opportunity to simultaneously record projections from a relatively large number of view angles at high speed (thusly enabling high temporal resolution also), and subsequently process the projections via tomographic reconstruction to obtain 3D measurements. For instance, a customized camera with multiple lenses was reported in 2005 to capture projections from 40 view angles, based on which 3D tomographic reconstructions were performed to obtain 3D flame structure at 500 frame per second (fps) [108]. Similar implementation of this multi-lens camera system can also be realized using image fibers, as reported more recently [99, 109], to collect multiple projections to the same camera. Alternatively, multiple cameras can also be used to collect multiple projections [14], an attractive option given the increasingly affordable consumer/industrial cameras. These past efforts have demonstrated TC's potential for 3D measurement with sub-millimeter spatial resolution and temporal resolution on the order of tens of microsecond, representing diagnostics capabilities solely needed.

4.2 Mathematical formulation

Figure 4-1 illustrates the mathematical formulation of the TC problem. Here we use $F(x,y,z)$ to denote the 3D distribution of the chemiluminescence emission to be measured, which is proportional to the concentration of the radicals that emit the

chemiluminescence (e.g., CH* or OH*). To perform tomography computationally, F is discretized into voxels in a Cartesian coordinate system (x-y-z) as shown. An imaging system records the 2D images of F on a camera (a CCD array in this research), and the image formed on the CCD array depends on its relative distance and orientation, specified by r (distance), θ (azimuth angle), and ϕ (inclination angle). Once the components in the imaging system (i.e., specifications of the lenses) are fixed, the image formed on the CCD array is uniquely determined by F, r, θ, and ϕ. We call the 2D images recorded on the CCD array projections, denoted as $P(r, \theta, \phi)$. The relationship between P and F is:

$$P(r,\theta,\phi) = \sum_{i_x}\sum_{i_y}\sum_{i_z} F(x_i, y_i, z_i) \cdot PSF(x_i, y_i, z_i; r, \theta, \phi) \tag{4.1}$$

where i_x, i_y, i_z are the indices of the voxel centered at (x_i, y_i, z_i); and PSF is the point spread function defined as the projection formed by a point-source located at (x_i, y_i, z_i) with unity intensity. Physically, Eq. (4.1) states that the projection is a weighted summation of the *PSF* across all voxels, and the weights are the value of the sought distribution. Now the 3D TC problem can be formally formulated as:

Given a set of projections (*Ps*) measured at various distances and orientations, find $F(x,y,z)$.

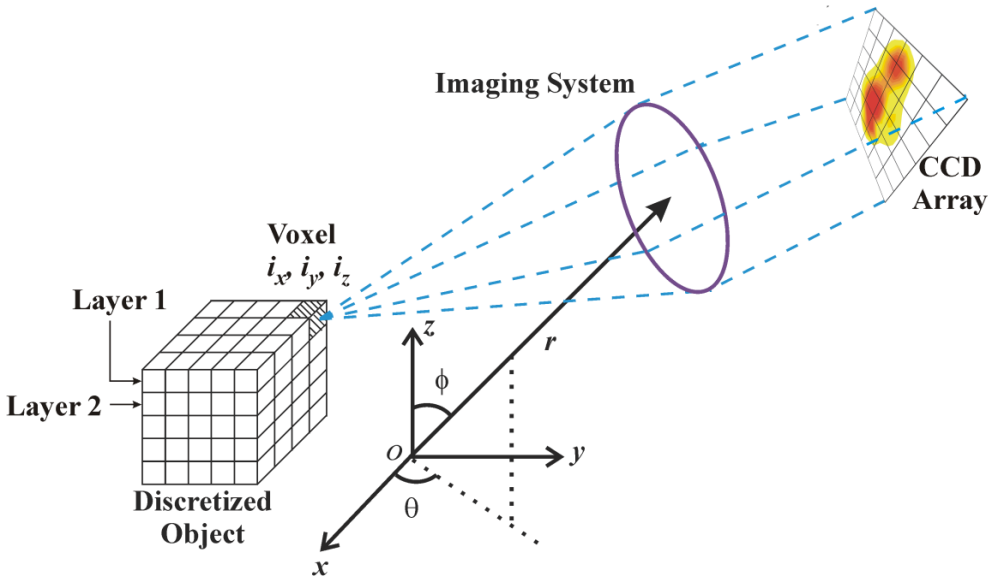

Figure 4-1. Illustration of the mathematical formulation of volumetric tomographic.

The *PSF* does not depend on the sought *F*. Therefore computationally, the *PSFs* are pre-calculated for the measurement locations and orientations (defined by r, θ, and ϕ). However, the *PSF* requires relatively large memory due to the 3D nature of the problem. The size of the *PSF* depends (almost linearly) on the degree of discretization of *F* and the projection, i.e., the number of effective pixels on which a projection is recorded and resolved. In our work, with *F* discretized into $30\times30\times30$ voxels and the projections recorded on $\sim1.6\times10^5$ pixels (a 400×400 CCD array), the *PSF* at each view angle required more than 2 GB of memory. Similar memory demands were also reported in [14]. Strategies to mitigate such memory demand will be discussed in a separate publication, so that this current dissertation stays focused on the fundamental issues of solving the 3D TC problem.

4.3 Tomographic inversion algorithm and regularization

Various algorithms have been developed to solve the tomographic inversion problem as formulated above [106, 110]. In our opinion, a systematic comparison of these

algorithms, which admittedly is a tremendous endeavor and is beyond the scope of this dissertation, will be highly valuable for a wide spectrum of applications. This research developed a hybrid algorithm combining ART (Algebraic Reconstruction Technique) and minimization technique, in which the ART algorithm was used to provide an initial guess for the minimization algorithm. This hybrid algorithm is motivated by the following two observations made from previous tomography work under the context of combustion diagnostics, both from our own and other research groups.

First, combustion applications, due to optical access and the dynamic nature combustion processes, typically have limited number of projections available, ranges from 2 [24, 111] to about 50 [14, 99, 108, 109, 112]. In contrast, other applications (e.g., medical imaging) have significantly more projections (thousands and more) available. Well-established (and also mathematically exact) algorithms such as filtered back projection and Fourier reconstruction [110] do not work optimally with such limited projections available in combustion diagnostics. With the limited projections in combustion diagnostics, past results suggest that inversion method based on minimization can solve the tomography problem effectively in the presence of measurement noises [24, 99, 112-114]. The tomography problem is cast into the following minimization problem:

$$\min \sum_{r,\theta,\Phi} [P_m(r,\theta,\phi) - P_c(r,\theta,\phi)]^2 \text{ with respect to } F(x,y,z) \qquad (4.2)$$

where Pm represents the measured projections at (r, θ, ϕ), Pc the projection calculated at (r, θ, ϕ) with a given distribution according to Eq. (4.1), and the summation runs over all locations and orientations of measurements. Eq. (4.2) essentially seeks the F that best (in the least squares sense) reproduces the projection measurements.

Second, certain properties of the sought distribution F are often known a *priori* in combustion diagnostics. For instance, the concentrations of radicals are nonnegative and bounded within a certain range, and the distribution is smooth due to heat and mass transfer. Therefore it is desirable to have an algorithm that can incorporate such a *priori* information when available to improve the reconstruction fidelity. The minimization technique described in Eq. (4.2) allows the flexible incorporation of a priori information via regularization. As shown below, instead of only minimizing the difference between measured and calculated projections as shown in Eq. (4.2) , a regularization term (R) can be added:

$$\min \sum_{r,\theta,\Phi} [P_m(r,\theta,\phi) - P_c(r,\theta,\phi)]^2 + \gamma \times R(F) \text{ with respect to } F(x,y,z) \qquad (4.3)$$

The regularization term is a function of F, and various mathematical expressions can be developed to quantify different types of a priori information of F [114, 115]. The regularization parameter, γ , is a preset constant that balances the relative weights of the first term and the regularization term [116]. In this research, γ was chosen using the guidelines provided in [31], and the optimal choice of γ is a nontrivial topic that deserves a spate treatment. Incorporation of a priori information via regularization has been demonstrated effective to ameliorate the ill-posedness of the inversion problem due to limited projection data [115, 116].

These observations were confirmed by extensive numerical simulations for the TC problems. Some of these results are shown Figure 4-2 using various phantoms and variations of different algorithms, including ART as described in [14], our hybrid algorithm, MART (Multiplicative Algebraic Reconstruction Technique) as described in [117], and OSEM (Ordered Subset Expectation Maximization) as described in [118].

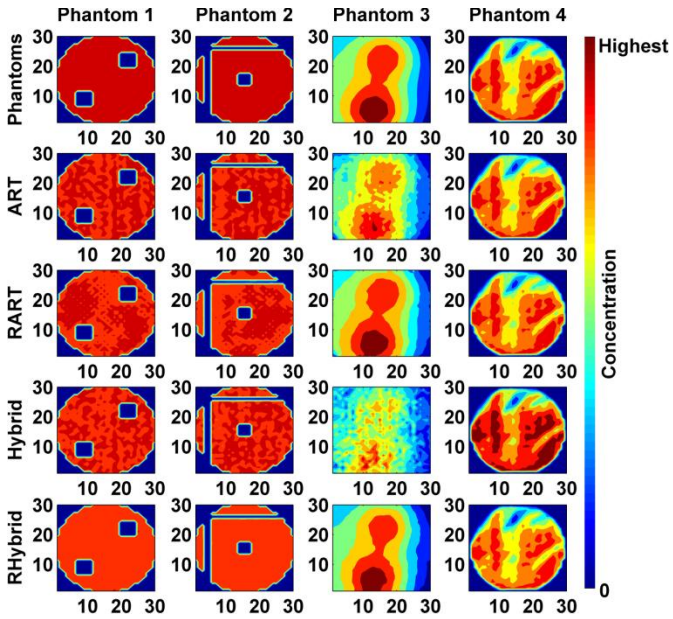

Figure 4-2. Comparison of phantoms and reconstructions

The top row of Figure 4-2 shows four of the phantoms tested in our numerical simulations. The four phantoms shown in Figure 4-2 include (from left to right) 1) a circular and uniform distribution with two square regions having zero value (The color scale is such that dark red and dark blue, respectively, indicates highest and zero concentration of the target radical. The same color scale is used hereafter), 2) a circular and uniform distribution with a square region and two lines with different thickness having zero value, 3) a smooth and continuous distribution with two peaks, and 4) a CH* distribution obtained by simulating a turbulent opposed-flow flame. All phantoms are discretized into 30×30×30 voxels. Figure 4-2 shows the fifteenth layer of the distribution. For phantoms 1, 2, and 3, the distribution is the same (as shown in the top row) on all layers to facilitate visualization; and for phantom 4, the distribution varies from layer to layer to simulate a turbulent flame. Phantoms 1 and 2 are created to simulate the flames experimentally tested, as detailed in Section 4.5.

Rows 2 through 5 in Figure 4-2 show the reconstruction obtained using ART and the hybrid algorithm, with and without regularization on the fifteen's layer. Results obtained with regularization are labeled as RHybrid and RART (regularized-Hybrid and -ART). Figure 4-3 shows the overall reconstruction error across all layers as defined by:

$$e = \frac{\sum_{i_x}\sum_{i_y}\sum_{i_z} | F^{rec}_{i_x,i_y,i_z} - F_{i_x,i_y,i_z} |}{\sum_{i_x}\sum_{i_y}\sum_{i_z} | F_{i_x,i_y,i_z} |} \tag{4.4}$$

where F_{Rec} represents the reconstructed distribution of the target radical.

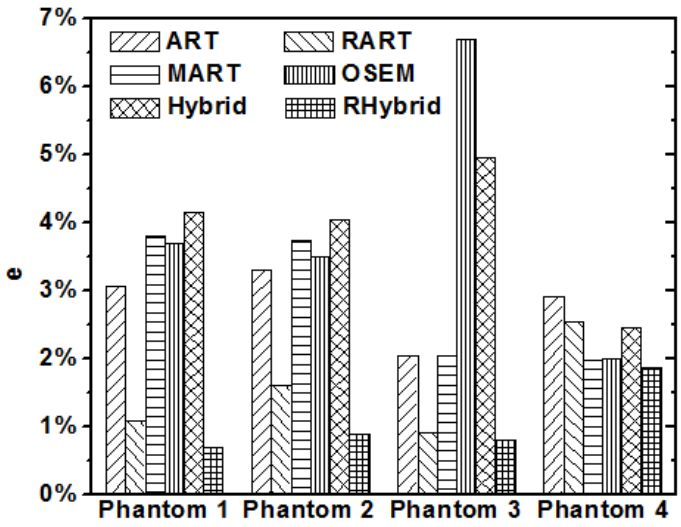

Figure 4-3. Comparison of overall reconstruction error using different algorithms

These results were obtained using projections measured from 8 view angles randomly chosen (but once chosen, these view angles were used in all algorithms to make the results comparable). To simulate practical conditions in our experiments, a 5% Gaussian noise was artificially added to the projections in these simulations. All algorithms were terminated when the relative change between two consecutive iterations was less than 10^{-3}.

There are multiple criteria that can be used to quantify the reconstruction fidelity across algorithms other than the overall *e* defined in Eq.(4.4). For example, the correlation between the phantoms and reconstructions can also be used to quantify the reconstruction fidelity [23]. In all our tests, the RHybrid algorithms also outperformed other algorithms under the correlation criterion. Figure 4-4 examines the reconstruction fidelity by another criterion: the distribution of reconstructions on each voxel. Both the overall *e* as shown in Figure 4-3 and the correlation criterion essentially averages the reconstruction error among all voxels in the measurement domain. However, the flame may not exist in all voxels and hence can bias both criteria. Therefore, Figure 4-4 provides a detailed illustration of the reconstruction error. Here the error is defined as the absolute value of reconstruction discrepancy at each voxel, normalized by the maximum value of sought function over the measurement of interest. As Figure 4-4 shows, both the RART and RHybrid algorithm improved the reconstruction fidelity within the flame zone, and the RHybrid algorithm did not only reduce the overall e as shown in Figure 4-3 but also the peak error.

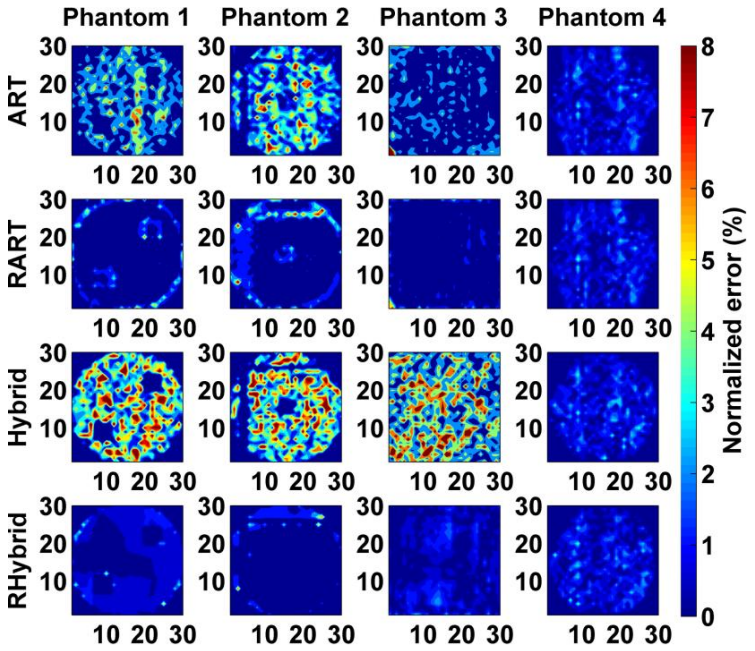

Figure 4-4. Distribution of reconstruction errors for phantoms shown in Figure 4-2.

As seen from Figure 4-2 to Figure 4-4, both ART and the hybrid algorithm can reconstruct all phantoms with reasonable fidelity, and the application of regularization significantly improved the fidelity. In all our numerical tests, the RHybrid algorithm yielded best reconstructions with smallest e, and was chosen for the rest of this chapter. The regularization used here is a so-called total variation (TV) regularization as described in [115]. The TV of the target function F is defined as:

$$R_{TV}(F) = \sum_{i_x,i_y,i_z} \sqrt{(F_{i_x,i_y,i_z} - F_{i_x-1,i_y,i_z})^2 + (F_{i_x,i_y,i_z} - F_{i_x,i_y-1,i_z})^2 + (F_{i_x,i_y,i_z} - F_{i_x,i_y,i_z-1})^2} \qquad (4.5)$$

According to Eq. (4.5), the *TV* of *F* represents the summation of the gradient magnitude of *F* over all voxels. Inclusion of R_{TV} in the reconstruction can preserve the smoothness or the edges of the sought *F* [115]. Therefore, as expected, the improvement was more dramatic on phantoms 1-3 than phantom 4, because phantoms 1 and 2 have clear edges and phantom 3 is smooth and continuous. In the RHybrid algorithm, the RTV term as described in Eq. (4.5) is simply used in Eq. (4.3). In the RART algorithm, the R_{TV}

term is minimized at the end of each ART iteration with respect to F, and the updated F is used as the input for the next ART iteration. Note that in this approach, the regularization and the ART iteration (which minimizes the difference between the calculated projections and the measurements) are essentially performed separately. Whereas in contrast, the RHybrid algorithm considers the regularization and the minimization of the difference between calculated and measured projections simultaneously (or holistically). We believe this contributes to the smaller e obtained by the RHybrid than the RART algorithm.

4.4 Numerical verification

Extensive numerical simulations have been conducted to verify the use of the RHybrid algorithm using various phantoms and noises. Figure 4-5 summarizes the results obtained on phantom 2 and 4 shown in Figure 4-2, with phantom 2 representing one of the experimental flames tested in this chapter and phantom 4 a turbulent flame. These simulations were performed under various noise levels, ranging from 0% to 10%, intended to encompass the range of noise expected in practical measurements. The experimental noise in this research is estimated to be about 5%. These results were obtained under similar configurations as those used in Figure 4-2 and Figure 4-3. Specifically, 8 projection measurements from 8 randomly chosen orientations were used in the reconstruction. But again, once chosen, these view angles were used in both the RART and RHybrid algorithms to make the results comparable.

As seen from Figure 4-5, the RHybrid algorithm consistently outperformed the RART algorithm in terms of the overall reconstruction error for all phantoms tested at all noise levels. Based on these numerical verifications, the RHybrid algorithm was chosen to

process the data obtained in this work. We have also processed the experimental results shown and examined the effects of view angles shown in Section 4.6 using other inversion algorithms, and the trend of the results obtained agreed with those obtained by the RHybrid algorithm as reported in Section 4.5 and 4.6.

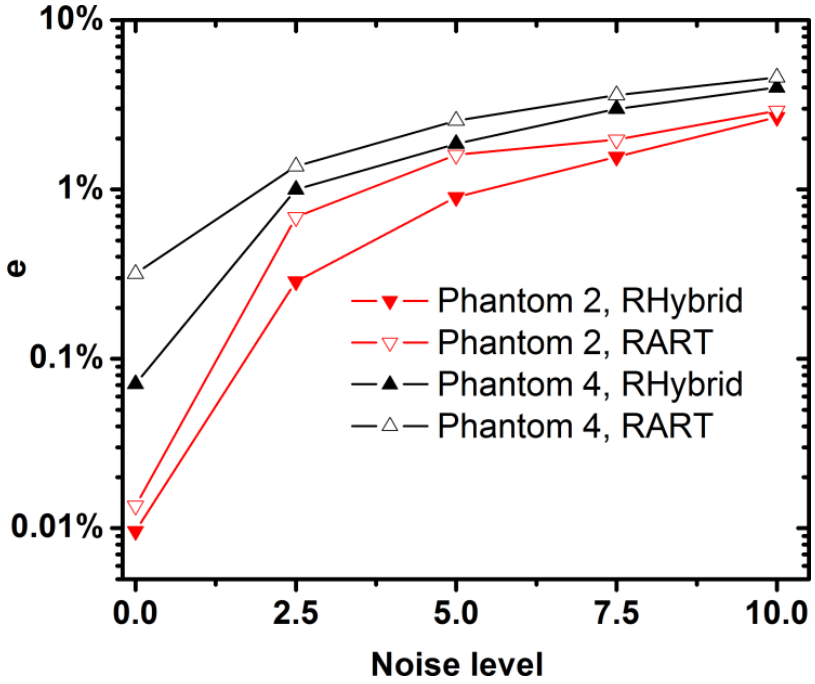

Figure 4-5. Comparison of RHybrid and RART at various noise levels.

Before leaving this section and proceeding to the experiments, note that 1) with accurate projections measurements (e.g., with noise level less than 2.5%), both the RART and RHybrid algorithms can provide reconstructions with high fidelity, and 2) in this work, the lower *e* from the RHybrid algorithm was achieved at a significantly higher computational cost (more than 10×) than the RART algorithm. This work solved Eq. (4.3) using a simulated annealing (SA) algorithm [116]. The SA algorithm is well recognized for its ability to minimize complicated functions. However, the SA algorithm is a stochastic algorithm and suffers from high computational cost, and we have been

exploring possible approaches to reduce the computational cost of solving Eq. (4.3). Possible approaches include parallelizing the SA algorithm [119], combining SA with proper orthogonal decomposition to reduce the dimension of the problem [120], or finding a deterministic algorithm to replace the SA algorithm.

4.5 Experimental arrangement

The TC technique was demonstrated using the experimental setup shown in Figure 4-6. The setup was designed to create flames with controlled patterns so that the TC technique can be validated experimentally. The setup used a McKenna burner (illustrated in panels (a) and (b)) to produce a stable and disk-like flame with a diameter of ~61 mm and a thickness of ~1 mm. Photos of a sample flame taken from the side and top are shown in panels (c) and (d). The fuel used in this study is methane (CH_4) and the oxidizer is air. To create asymmetric flame to demonstrate the 3D nature of TC technique, a honeycomb was place on the burner (panel (a)). The honeycomb's cells are squares with size of 1.25×1.25 mm (panel (b)) and certain cells were blocked to create the desired asymmetric pattern. Various patterns have been created and studied in this research. For example, phantom 1 shown in Figure 4-2 illustrates one of the patterns created by blocking two rectangular regions of the honeycomb. Panel (b) of Figure 4-6 here shows another pattern, where we block a rectangular region with a size of 8.75×10 mm, a column of cells to form a vertical line with 1.25 mm thickness, and two rows of cells to form a horizontal line with and 2.5 mm thickness. Phantom 2 shown in Figure 4-2 simulates this flame.

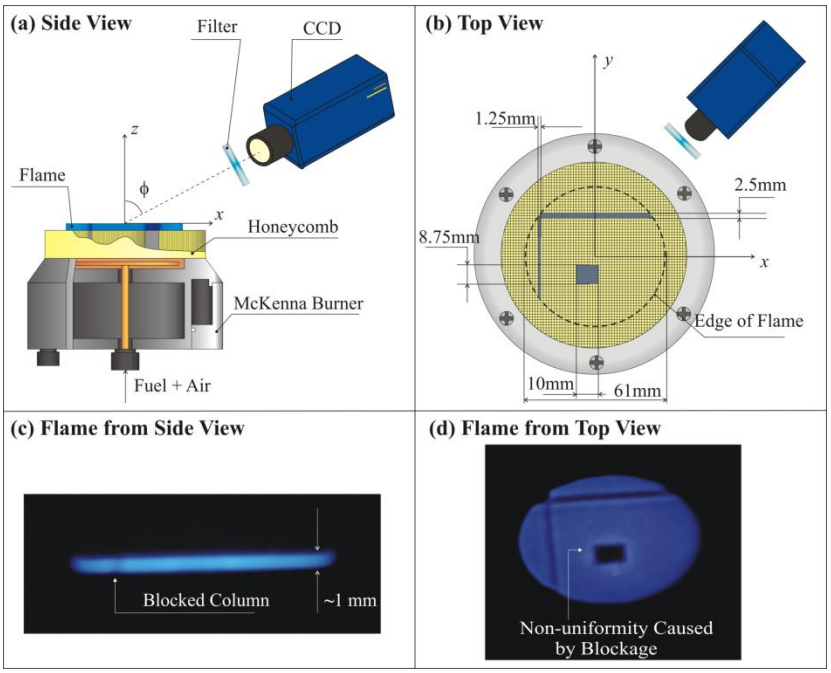

Figure 4-6. Experimental setup for demonstrating the TC technique.

A CCD camera (PCO Sensicam) was used to take projection measurements of the chemiluminescence emitted from CH^* radicals in the flame from various view angles sequentially. The camera was installed on a rotation stage (Newport 481-A), which was used to set the desired pitch angles. The stage was then fixed on an optical rail to adjust r's and θ's. The lens used has a focal length of 35 mm and the numerical aperture was set at 1.7 during the measurements. A band pass filter (Thorlabs MF434-17, 434±8.5 nm) was applied to block the background luminosity. Each projection measurement was taken with a 50 ms exposure time. Simultaneous measurement from multiple view angles can be achieved using multiple cameras as demonstrated elsewhere [14]. The exposure time can be shortened using a different camera or different image systems. For example, in our test, an intensified CMOS camera (Photron Fastcam SA4) reduced the exposure time to tens of μs with good signal to noise ratio.

In this research, we decided to use one CCD camera to take the projection measurements sequentially at a relatively lower temporal resolution to study several fundamental aspects of the TC technique, such as the tomographic algorithm, the placement of the view angles, and spatial resolution. Other aspects of the TC technique, such as signal level and temporal resolution, will be discussed in a separate publication. Using one camera instead of multiple cameras eliminates the uncertainty caused by calibration across cameras, and CCD cameras provide better linearity than CMOS cameras. The sequential measurements with 50 ms exposure time is justified by the stability of the flame, which was measured to be stable within 4% both in the short term (~50 ms) and long term (~10 minutes, the time needed to measure a complete set of projections). The stability of the flame represents the major uncertainty in the projections, which is the reason that results shown in Figure 4-2 were obtained with 5% artificial noise.

As mentioned before, the purpose of this setup is to create controlled flame patterns. These patterns will be binary under ideal conditions, i.e., if the flame is perfectly uniform and blocked area creates a step change of the concentration of target radical (CH^* in this chapter). However, such an ideal binary patterns were only approximated in our experiments due to convection, diffusion, and disturbance of the flow caused by the blockage. These non-ideal conditions are manifested in panels (c) and (d). For instance, if the flame pattern is perfectly binary, then the blocked column should be a completely dark region when viewed from the side as shown in panel (c). In practice, this region was darker (i.e., with lower CH^* concentration) relative to other regions, but not completely dark (i.e., with zero CH^* concentration). Also, the edges of the block region are not

ideally sharp and uniform. As seen from panel (d), the blockage increases the flow rate in the adjacent cells and creates a non-uniform distribution in that region.

Despite of these above non-ideal features, the flames created via this approach still provide us with well-controlled patterns, and it is highly desirable to have such experimental "phantoms" to quantitatively validate the TC technique. The quantitative value of these experimental phantoms will be further elucidated later when we report the tomographic results.

4.6 Experimental results

Projection measurements were performed on flames created using the setup shown in Figure 4-6 from various view angles. Eight of these view angles are listed in Table 4.1. The orientation (θ and ϕ) and location (r) of the projection measurements were determined using the method described in [121] using a reference target. A pitch angle was defined as 90^0- ϕ to describe the angle formed by the optical axis with the x-y plane. The location r was defined as the distance from the center of the burner to the center of the camera lens.

Table 4.1. Orientation and location of the projection measurements.

Projection index	(degree)	. (degree)	Pitch angle	r (cm)
1	74.88	-46.76	15.12	55.36
2	71.20	-10.40	18.80	42.20
3	71.76	45.40	18.24	42.80
4	74.84	86.40	15.16	55.28
5	71.20	90.80	18.80	42.20
6	74.60	121.60	15.40	54.60
7	71.04	153.04	18.96	42.00
8	74.60	176.40	15.40	54.60

Figure 4-7 shows a sample reconstruction using the projections tabulated above. In this reconstruction, the domain of interested (DOI) considered was a cylindrical region with a diamter of 67.5 mm and a height of 2.5 mm to encompass the flame (the flame has a diameter of ~61 mm and a thickness of ~1 mm). The DOI was descretized into 54 (x direction) $\times$ 54 (y direction) $\times$ 10 (z direction) voxels, resulting in a total of 29,160 voxels. Each voxel has a dimension of 1.25 mm in both the x and y directions and 0.25 mm in the z direction. The orgin of the x-y-z cooridate is at the center of the burner as shown in Figure 4-6. The reconstructed flame is sampled at four different z positions. Panel (a) of Figure 4-7 shows the reconstruciton for the first layer right above the surface of the honeycomb (i.e., $0 < z < 0.25$ mm), and panel (b) through (d) of Figure 4-7 the second, fourth, and eighth layers, respectively. Note that the results are displayed in layers simply for the sake of convenience and clarity. All algorithms in this chapter are implemented in 3D, and these algorithms solve the TC problem as a 3D problem. The results in this work were not obtained by stacking a series of 2D solutions layer by layer. The advantages of decomposing a 3D problem into a series of 2D problems and solving them separately include simplicity and reduced computational requirements; however this approach also has disadvantages, both practical and fundamental. Practically, the experiments need to be designed to allow the conversion of 3D problems to 2D problems, resulting in complicated hardware, alignment, and loss of signal [108, 109]. A fundamental disadvantage involves consideration of regularization. When the problem is solved in 3D, regularization in all three directions can be considered simultaneously, which is difficult or even impossible when the problem is solved as a series of 2D problems.

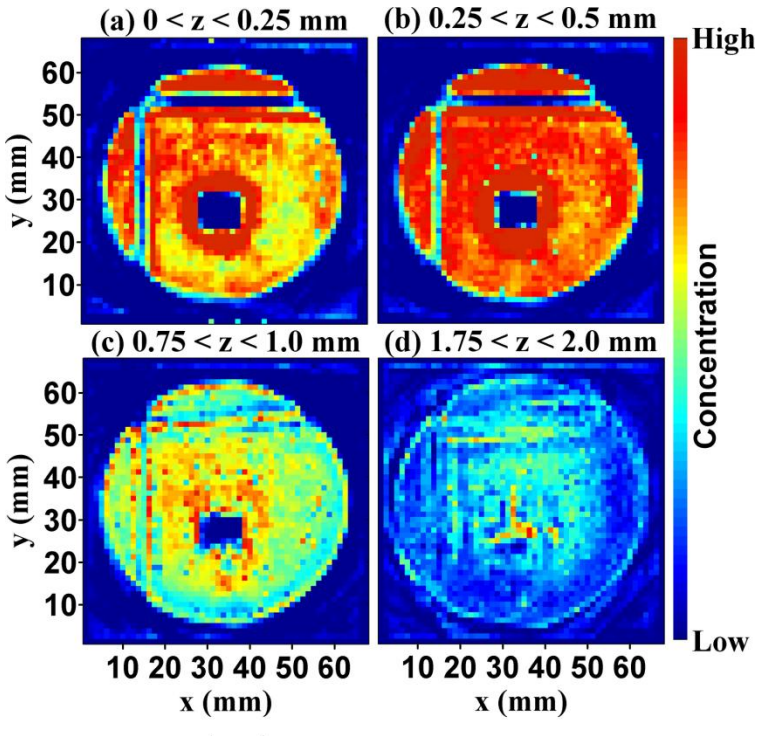

Figure 4-7. Reconstructed flame at different *z* positions.

As shown in Figure 4-7, the flame pattern created by the blockage was clearly resolved in the first two layers above the honeycomb. The TC technique successfully reconstructed the size and thickness of the flame, the size, shape, and location of the blocked regions. As the flame propagates further in the *z* direction, transport phenomena cause the pattern to be blurred, as suggested by the reconstruction at the fourth and eighth layers shown in panels (c) and (d), respectively.

Figure 4-8 analyzes the reconstruction fidelity quantitatively by examining the size of the blocked areas. Panel (a) through (d), respectively, shows the thickness of the blocked column and row, and the width and the height of the blocked rectangle of the flame pattern. These quantitative information were obtained by calculating the gradient of the reconstruction at each layer (e.g., those shown in Figure 4-7) to determine locations of sharpest CH^* concentration change, which were then subsequently used to calculate the

size of the blocked areas as shown here in Figure 4-7. At each layer, multiple values were obtained along the edge of the block region; and the square symbol represents the median of these values for a given layer and the error bar represents the std (standard deviation) of these values.

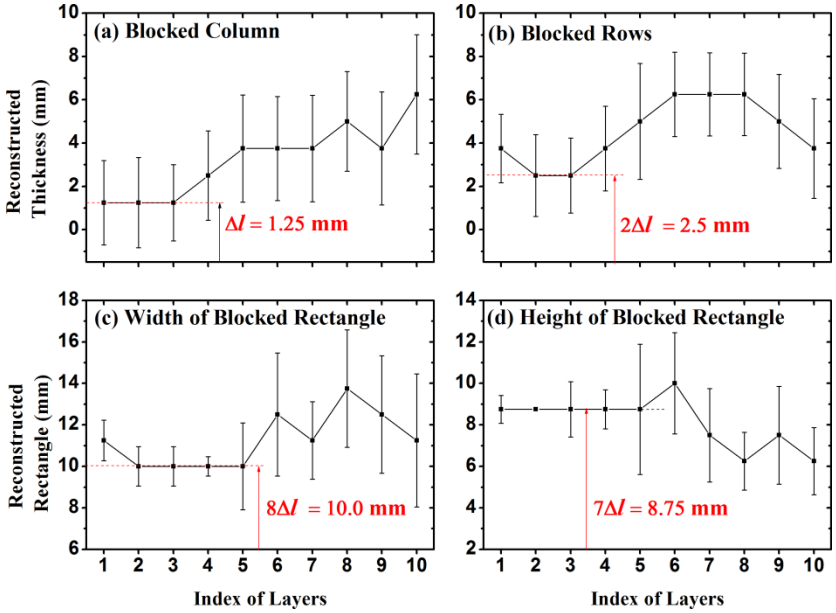

Figure 4-8. The reconstructed size of blocked areas.

Figure 4-8 further elucidates the visual observations made in Figure 4-7, illustrating the blurring of the flame pattern as it propagates along the *z* direction. For example, panel (a) shows the reconstructed thickness of the blocked column, created by blocking on column of the cells on the honeycomb. As mentioned in Section 4.5, these cells are square and have a size of Δl = 1.25 mm. The reconstructions yielded a median thickness of 1.25 mm for the first three layers, equal to the thickness of the blocked region, illustrating the limited blurring caused by transport. The std on these three layers were caused by a combination of four factors: the blurring due to transport, the non-uniformities caused by the blockage, measurement uncertainty, and the reconstruction artifacts. We argue that the first two factors are the major causes based on the simulations

results reported in Figure 4-2 and Figure 4-7. Those results demonstrated that the RHybrid algorithm can reconstruct the thickness of a block column accurately under the measurement uncertainty expected here. Starting on the fourth layer, the difference between the reconstructed thickness and Δl gradually increases with the layer index, and so does the std. Such increasing difference and std suggest the more and more pronounced blurring of the flame pattern caused by the transport phenomena. Similar interpretations can be made for results shown in panels (b) to (d).

These results demonstrate the TC's ability to resolve flame structures (and also potentially transport physics). Here we focus on the spatial resolution of the TC technique. Sub-millimeter spatial resolution has been reported previously [14] for the TC technique based on a combination of theoretical analysis and experimental observations. The results in panel (a) of Figure 4-8, in contrast, provide direct experimental data to demonstrate a spatial resolution on the order of 1.25 mm. Research work is underway to experimentally investigate the spatial resolution of the TC technique beyond 1.25 mm using the current experimental approach.

Our results suggest that for an unknown flame, it is advantageous to use random view orientations rather than coplanar orientations as typically used in the past. These findings are expected to illustrate the importance of optimizing view orientations, which is of both practical and fundamental relevance. Practically, combustion applications often have limited optical access and such access should be designed and used optimally. Fundamentally, it is desirable that projections obtained from different view orientations, especially when only a small number of view orientations are available, should provide complementary information, not redundant information.

Here, coplanar is defined as the TC configuration where the optical axes along which projections are obtained fall on the same plane. Such coplanar configuration seems to be natural, especially for a flame with open optical access. However, a coplanar configuration essentially poses a restriction on the view orientations, and may not provide the optimal information for the reconstruction. As a simple example, consider the flame pattern shown in panels (c) and (d) of Figure 4-10. For this flame, views from the side (with a 0^0 pitch angle) largely provide redundant information (e.g., about the shape, size, and thickness of the flame). In contrast, a view from the top (with a 90^0 pitch angle) provides a wealth of key information about the flame structure: the shape, size, and location of the blocked areas besides the shape and size of the flame. As a result, two views, one from the side and another from the top, provide complimentary information for the reconstruction, which can be much more valuable than many coplanar views taken from the side. Therefore, generally, when the target flame is unknown, projections taken from random view orientations are statistically more likely to provide complementary information than coplanar view orientations. From a mathematical point of view, arbitrary view angles are more likely to provide projections that are more linearly independent from each other and reduce the ill-posedness of the problem.

The results shown in Figure 4-9 confirm these intuitive arguments using both simulation (panel (a)) and experimental (panel (b)) studies. In panel (a), simulations were conducted using the RART and RHybrid algorithm to reconstruct the phantoms shown in Figure 4-9 using eight projections, and 5% of artificial noise was added to the projections. Two sets of projections were used here: a set generated under the coplanar configuration and another set generated randomly. As can be seen, the reconstruction error from the

coplanar configuration is consistently and substantially larger than that from the random view orientations. The reconstruction error from the coplanar configuration is also substantially larger than those reported in Figure 4-3, which used randomly generated view orientations.

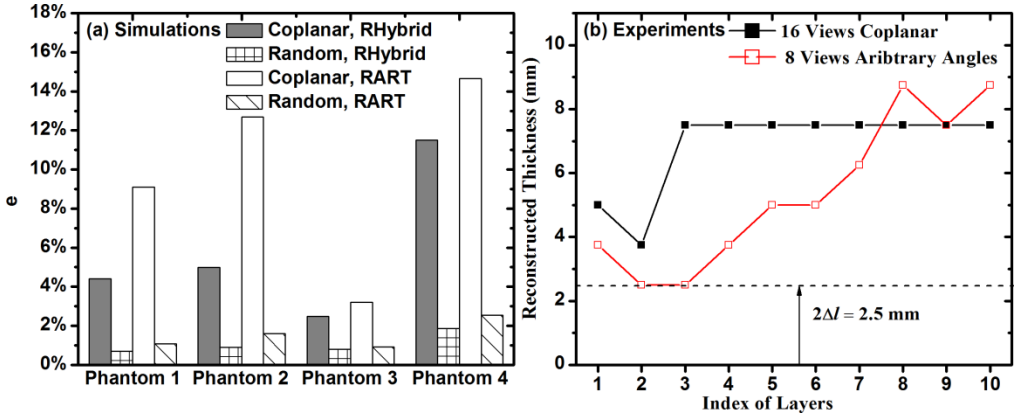

Figure 4-9. Panel (a): comparison of e using coplanar and arbitrary view angles from numerical simulation. Panel (b): Reconstructed thickness using coplanar and non-coplanar view angles from experimental data.

In panel (b), the experimentally-measured projections were used to reconstruct the flame patter by the RHybrid algorithm. We first used projections all obtained with a pitch angle of 0^0 (a coplanar configuration). Under such coplanar configuration, eight projections were insufficient to produce satisfactory reconstruction. Panel (b) shows the reconstructed thickness of the two blocked rows using sixteen coplanar projections. To elucidate the advantage of random orientations, we then used eight projections, randomly picked from a pool of projections measured at the orientations shown in Table 4.1 and also 0^0 degree pitch angle. As shown in panel (b), these eight projections provide complementary information to reconstruct the thickness significantly more accurately than the sixteen coplanar projections. Examination of other blocked areas reveals similar

or more dramatic superiority of the randomly chosen orientations over the coplanar orientations.

4.7 Practical aspects of TC

So far, both numerical and experimental studies have been performed to understand the capability of TC. In this section, we discuss practical aspects, such as stop criterion, regularization, spatial resolution, and binning, in implementing TC. For this purpose, we create a new set of phantoms to approximate practical flames. For example, phantom 1 in Figure 4-10 was created to simulate the patterned McKenna burner flame generated experimentally, phantom 2 to simulate the stable Bunsen flame, phantom 3 to simulate a turbulent jet flame, and phantom 4 to simulate a turbulent flame stabilized by a v-gutter. Though Figure 4-10 shows one layer of each phantom, all phantoms were created and used volumetrically in this research.

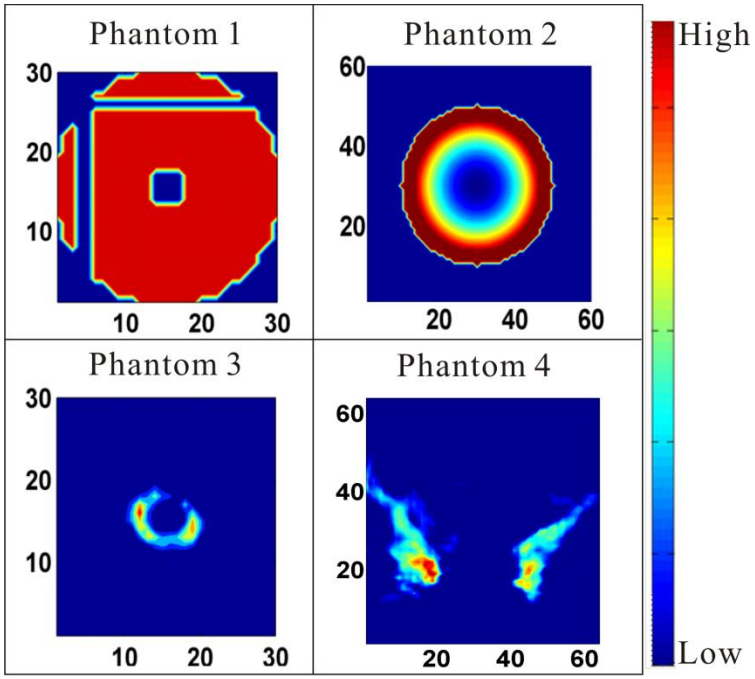

Figure 4-10. Phantoms used for numerical simulations

4.7.1 Termination criterion

An effective termination criterion is important for any inversion method because it directly affects the computational cost and also the reconstruction accuracy. An ideal termination criterion is one that guarantees convergence while aborts immediately when further calculation provides negligible improvements. Unfortunately, there is no universal criterion to our knowledge that works effectively for all practical applications, where empirical criteria are often used. As an example, the following termination criterion has been used for the ART algorithms [122]:

$$\left|\sum_{i_x}^{N_x}\sum_{i_y}^{N_y}\sum_{i_z}^{N_z}F^k(x_i,y_i,z_i)-\sum_{i_x}^{N_x}\sum_{i_y}^{N_y}\sum_{i_z}^{N_z}F^{k-1}(x_i,y_i,z_i)\right|\le\varepsilon\cdot\beta\cdot\sum_{i_x}^{N_x}\sum_{i_y}^{N_y}\sum_{i_z}^{N_z}F^k(x_i,y_i,z_i) \quad (4.6)$$

where F^k and F^{k-1} are the reconstructed F in the k^{th} and $(k-1)^{\text{th}}$ iteration, respectively; ε is a small positive number and was empirically suggested to be in the range of $[10^{-6}, 10^{-3}]$; and β is the relaxation factor in the ART algorithm. This criterion essentially terminates the ART algorithm when the overall change in F during two consecutive iterations is below a small proportion of the overall magnitude of the reconstructed F. Figure 4-11 illustrates the limitation of this criterion by simultaneously tracking D and e during ART iterations. Here D refers to the overall difference between the measured and calculated projections during the k^{th} iteration, i.e.:

$$D=\sum\nolimits_{r,\theta,\phi}\left|P_m^k(r,\theta,\phi)-P_c^k(r,\theta,\phi)\right|^2 \quad (4.7)$$

where P_m^k and P_c^k P_m stand for measured and calculated projection obtained by the end of the k^{th} ART iteration. As Figure 4-11 shows, D decreases monotonically with k, which increases monotonically with decreasing ε because more iterations are needed to find F

that can better match the calculated projections to the measured ones. However, *e* does not decrease monotonically with increasing *k* (and consequently not decreasing ε either). In the results shown in Figure 4-11, setting $\varepsilon = 10^{-3}$ terminated the inversion too early, before it the minimal *e* was reached. In contrast, setting $\varepsilon = 10^{-4}$ terminated the inversion too late, after it passed the minimal *e* and resulted in a less accurate reconstruction after almost $4\times$ more computational cost compared to the criterion with $\varepsilon = 10^{-3}$. The results in Figure 4-11 were obtained phantom 1, eight randomly positioned views, 5% artificial Gaussian noise in projections. The ART, MART, and OSEM algorithms were tested on various phantoms with different termination criteria. The results confirmed the difficulty of designing an effective termination criterion. All the algorithms showed success on some cases, and also encountered issues like those illustrated in Figure 4-11 on other cases.

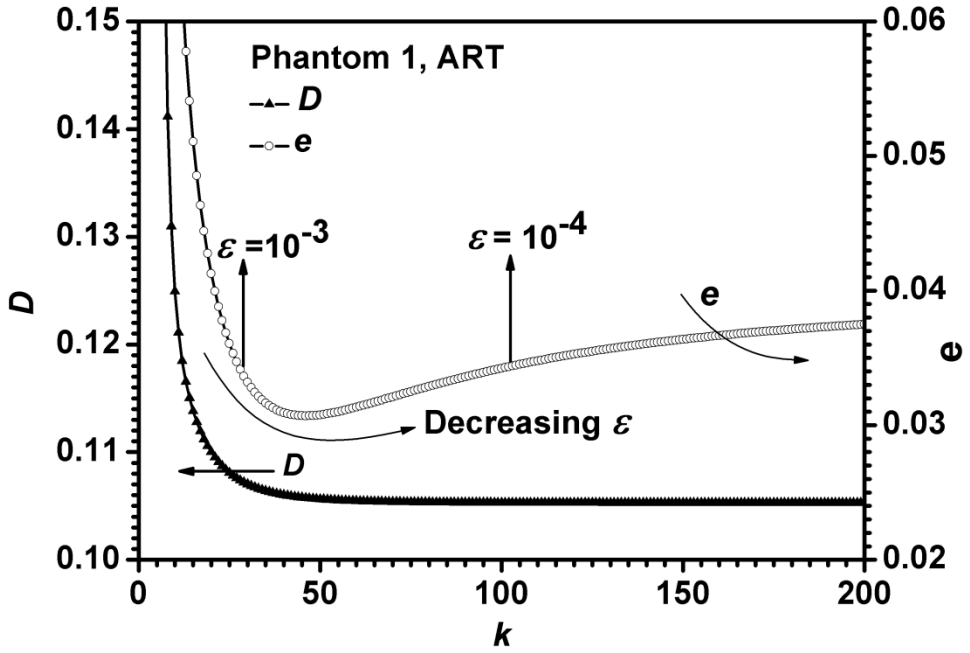

Figure 4-11. Evolution of *e* and normalized residual illustrating issues with termination criterion in the ART algorithm.

In comparison, the new TISA algorithms that we developed can be terminated consistently with a simple criterion in all the cases we tested. The TISA algorithm solves Eq. (4.2) by the Simulated Annealing (SA) algorithm. The SA algorithm minimizes D defined in Eq. (4.2) also by iterations, and the following criterion was found to be effective:

$$\left|D^k - D^{k-1}\right| \le \varepsilon \cdot D^k \tag{4.8}$$

where D^k *and* D^{k-1} are the difference between the simulated and measured projections as defined in Eq. (4.2) during the k^{th} and $k\text{-}1^{th}$ iteration, respectively. Similar to Figure 4-11, Figure 4-12 tracks D (normalized by D^1) and e simultaneously under the same conditions as those used in Figure 4-11. The results in Figure 4-12 show that, with Eq. (4.8), both D and e decreased monotonically with decreasing ε (i.e., increasing k and computation cost) in the TISA algorithm. Results obtained in other cases with the TISA algorithm showed the same trend as seen in Figure 4-12.

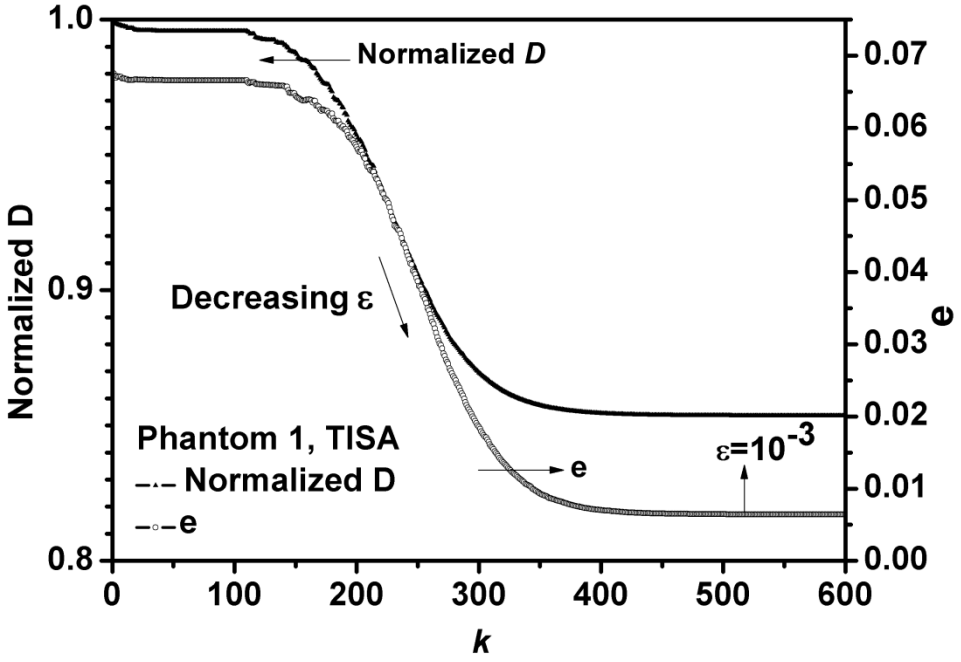

Figure 4-12. Evolution of *e* and normalized *F* illustrating the monotonic decrease of *e* in the RHybrid algorithm.

4.7.2 Regularization

It has been well recognized that *a priori* information, if available, can be incorporated in the tomographic inversion via regularization to improve the inversion [74, 115, 116]. Here we studied the regularization of the ART and TISA algorithms (the regularized algorithms were code named RART and RTISA, respectively). Two types of regularizations were studied: smoothness and total-variation. The smoothness regularization considers the degree of smoothness of the sought *F* in the inversion, as detailed in [73, 74]. The total variation (TV) regularization of the target function *F* is defined as [115]:

$$R_{TV}(F) = \sum_{i_x,i_y,i_z} \sqrt{(F_{i_x,i_y,i_z} - F_{i_x-1,i_y,i_z})^2 + (F_{i_x,i_y,i_z} - F_{i_x,i_y-1,i_z})^2 + (F_{i_x,i_y,i_z} - F_{i_x,i_y,i_z-1})^2} \quad (4.9)$$

According to Eq. (4.9), the *TV* of *F* represents the summation of the gradient magnitude of *F* over all voxels. Inclusion of R_{TV} in the reconstruction has been shown to preserve the

smoothness or the edges of the sought F [15, 115]. In the RART algorithm, the R_{TV} term was minimized at the end of each ART iteration with respect to F, and the updated F was then used as the input for the next ART iteration. In the RTISA algorithm, the R_{TV} term was simply added to the difference defined in Eq. (4.2) to form a new master function to be minimized, i.e.:

$$\min \quad f = D + \gamma \cdot R_{TV} \tag{4.10}$$

where f is the new master function and γ the regularization parameter to adjust the relative importance between the D and R_{TV} terms. The optimal selection of γ is critical for the application of any regularization technique, which controls the relative weights of the *a priori* information (e.g., smoothness or total variation) and the *a posteriori* knowledge (i.e., the measurements) in the tomographic inversion process [116]. This research found that the so-called L-curve method developed for solving ill-posed linear equations [123] to be effective in determining the optimal γ for relatively simple flames.

Before detailing the choice of γ, Figure 4-13 first shows a set of results to illustrate the usefulness of regularization (and also its limitations). We applied the ART algorithms to various phantoms with and without the TV regularization, and two sets of example results are shown in Figure 4-13 . These results were obtained with phantoms 2 and 4 as shown in Figure 4-10. Eight simulated projections were used in the simulations, with 5% Gaussian noise artificially added to the projections to simulate measurement uncertainty. The upper panel of Figure 4-13 shows the reconstruction of phantom 2, which as mentioned earlier, was created to simulate a cone-shaped stable laminar flame generated by a Bunsen burner. Note that even though the phantom is axially symmetric, the

tomographic reconstruction did not assume such *a priori* knowledge. From left to right are the phantom itself, the ART reconstruction, and the RART reconstruction, respectively. As can been seen, The ART reconstruction had artifacts (e.g., the discontinuities and cavities in the reconstruction) and the overall error was e=5.6%. The application of the TV regularization significantly reduced the overall error to e=2.8% and eliminated much of the artifacts seen in the ART reconstruction.

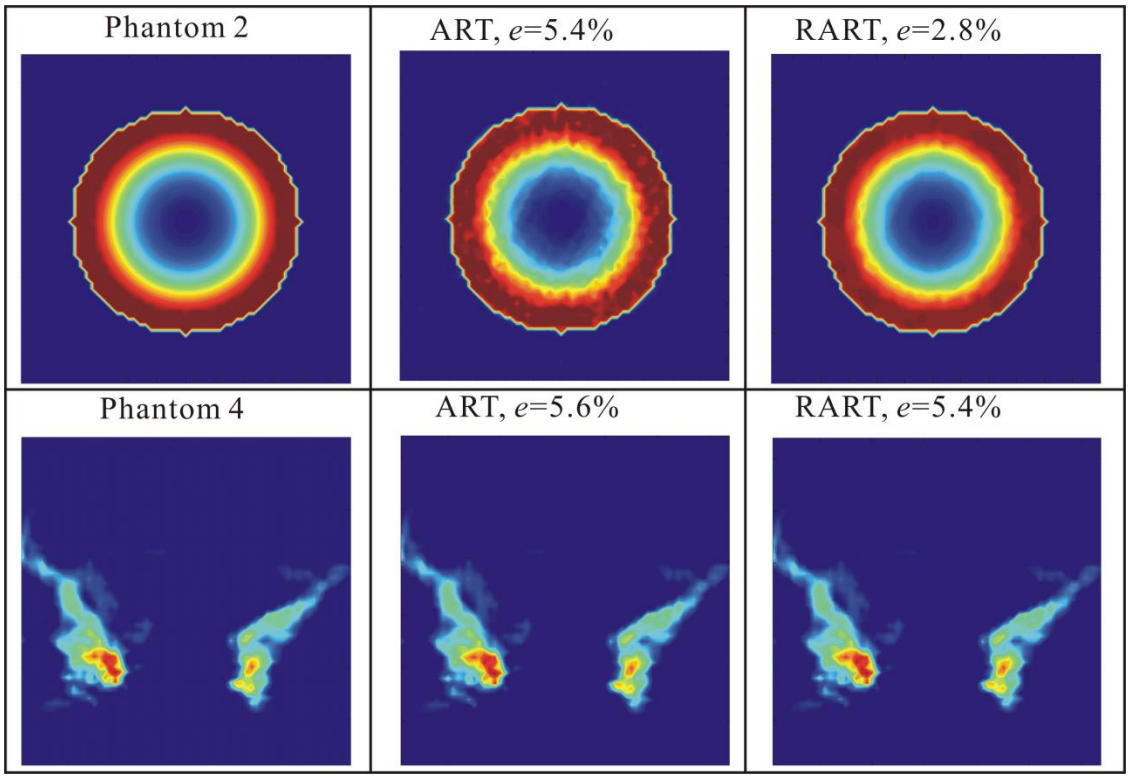

Figure 4-13. Application of regularization in the TC technique. Projections from eight random views were used with 5% Gaussian noise added (these same conditions were used in the results in Figure 4-14 and Figure 4-15).

The lower panel of Figure 4-13 shows the reconstruction of Phantom 4, which was created to simulate a turbulent flame stabilized on a V-gutter. Again from left to right are the phantom itself, the ART reconstruction, and the RART reconstruction, respectively. As can be seen, the ART and RART reconstructions were almost identical to each other.

The overall error of the ART reconstruction was e=5.6%, and that of the RART reconstruction is e = 5.4%.

Several observations can be made from the results shown in Figure 4-13, and these observations were valid when we applied regularization to other algorithms (e.g., the TISA algorithm) and other phantoms. First, with a proper choose of γ (to be discussed immediately below), the application of regularization reduced e for all algorithms on all phantoms tested. Second, however, the reduction was more pronounced on smooth (or "laminar") phantoms than on irregular (or "turbulent") phantoms, because the TV regularization preserves the smoothness and sharp edges. In the examples shown in Figure 4-13, phantoms 2 is smooth and has clear edges and therefore the TV regularization is effective, but phantom 4 does not feature any clear edge or smooth distribution, causing the ineffectiveness of the TV regularization as reflected in Figure 4-13. It is an important research topic to find a regularization that can work effectively on turbulent targets, and we are exploring the incorporation of governing equations as regularization in our ongoing work.

Figure 4-14 and Figure 4-15 provide more insights into results shown in Figure 4-13, and also illustrate the selection of γ using the L-curve method. In practice, the sought F is unknown, and therefore e is not available to guide the selection of γ. The L-curve method recognizes this issue and therefore relies on quantities that can be practically obtained to determine γ: the difference between the measured and calculated projections (D) and the regularization term itself (e.g., R_{TV}). In the L-curve method, the inversion problem is solved multiple times, each time with a different γ; and D and the regularization term are

recorded each time. Panel (a) of Figure 4-14 shows a set of results of D and R_{TV} recorded when the TV regularization was applied to phantom 2 using the RTISA method. The plot had an approximate L shape, and the L-curve method used the γ corresponding to the corner of the L curve as the optimal values. This work calculated the maximum curvature to determine the corner, and the points near the corner were shown as solid square symbols in Panel (a) of Figure 4-14. Panel (b) of Figure 4-14 shows the e obtained under the γs used (because a known phantom was used here so e can be calculated). The solid triangle symbols correspond to the γs near the corner of the L-curve shown in Panel (a), illustrating that the minimal e indeed occurred at the γs determined by the L-curve method. The L-curve exemplified in Panel (a) of Figure 4-14 is essentially a trade-off curve. When γ is negligibly small (i.e., 1.5×10^{-5}), the inversion was performed only to minimize D without considering the regularization, resulting in small D and large R_{TV}. When γ is exceedingly large (i.e., 15), the inversion was performed only based on the regularization (i.e., to minimize the TV) without considering the measurements, resulting in large D and small R_{TV}. The success of the L-curve method in the case shown in Figure 4-14 lies in the existence of a distinct corner during the transition from small to large γ, as shown in Panel (a). Such a distinct corner represents an optimal balance between D and R: any further increase in γ leads to a sharp rise in D, and any decrease in γ results in negligible change in D. Therefore, the γs near the corner represent a state where the maximum "amount" of regularization that can be added in the inversion without affecting the role of the measurements.

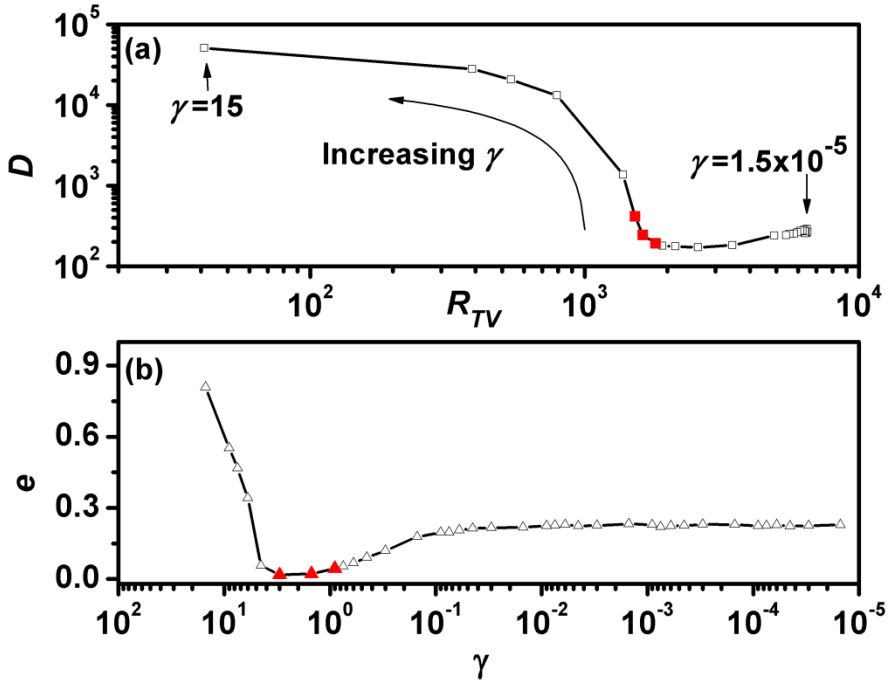

Figure 4-14. The L-curve for phantom 2 (a smooth flame).

In contrast, the data shown in Figure 4-15 obtained on a turbulent phantom do not exhibit such a distinct corner. As shown in Panel (a), the transition from small to large γ was gradual in this case, resulting in the failure to identify the optimal γ and explaining the marginal usefulness of regularization observed in Figure 4-13.

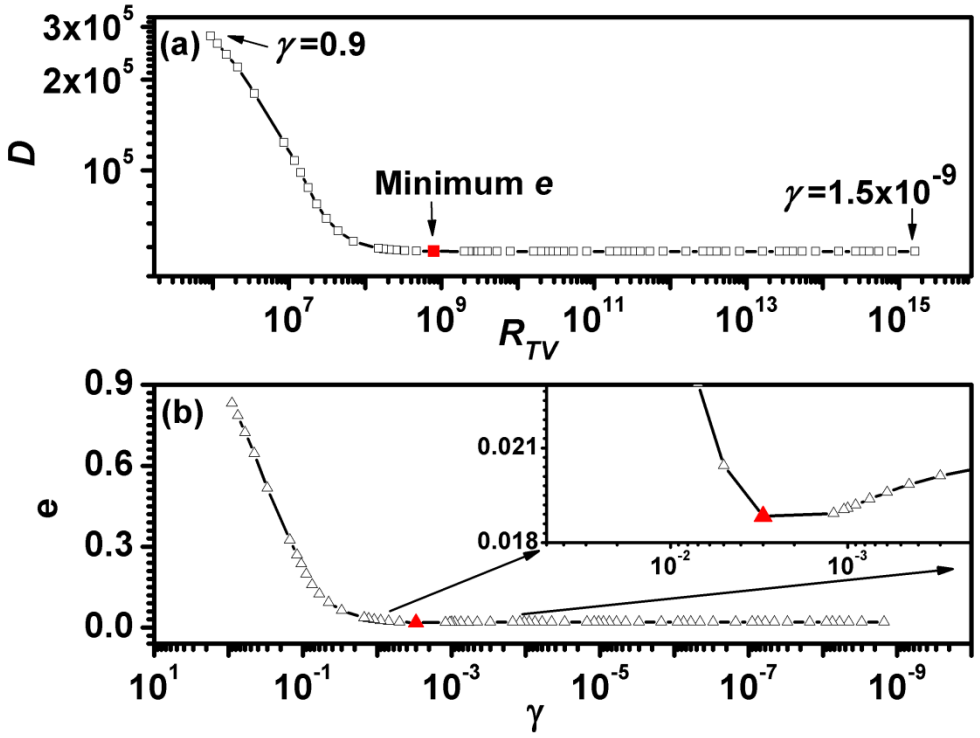

Figure 4-15. Application of regularization to phantom 4 (a turbulent flame).

Application of the smoothness regularization to the phantoms showed similar trend as seen in Figure 4-14 and Figure 4-15. Both the smoothness and TV regularization were effective in improving the inversion on phantoms that are smooth and/or have clear edges, but not effective on turbulent phantoms. The design of an effective regularization technique for turbulent objects is an important research need.

Lastly, the studies described in Section 4.7.1 and 4.7.2 were also performed using experimental data, and the same observations were made as those made with numerical phantoms. The experimental flames were not as accurately known as the numerical phantoms. Therefore, the studies involving experimental data relied on some characteristic features extracted from the flames, and such extraction is best explained in Sections 4.7.3 below.

4.7.3 Number of views and resolution of projection measurements

The number of views and resolution of the projection measurements are also two important aspects for the practical implementation of 3D diagnostics. They directly impact the requirement of optical access and cost (both hardware cost and computational cost). Therefore, this section investigates their effects on the quality of the 3D measurements.

Figure 4-16 shows the reconstruction using experimental data of a flame generated using the setup discussed in Section 4.2. To examine the effects of number of views (N) and resolution of the projections measurements, the reconstruction was performed under four different cases by varying the number of views (N=4 and 8) and applying binning to the projections (2×2 binning and no binning). Without binning, projections measured by the CCD camera (1376×1040 pixels with 6.45×6.45 μm pixel size) were directly used in the inversion. The measurement domain was discretized into 64×64×16 voxels (a total of 65,536 voxels). Under these conditions, the *PSD* described in Eq. (1) at one view angle was about 8 GB in size when stored in double precision. The size of the *PSD* is approximately proportional to the number of pixels in the projection measurements. Therefore with 2×2 binning, the size of the *PSD* reduced to 2 GB per view angle. Such memory requirement and computational cost underline the importance to carefully design the number of views and resolution of the projections in practice. Figure 4-16 shows that 1) 8 views resulted in an overall more accurate reconstruction than 4 views, and 2) with a fixed number of views, reducing the resolution of the projections via binning does not significantly deteriorate the overall quality of the reconstruction. One explanation for the second observation is that while binning reduced the resolution and thusly reduced the

number of measurements available as inputs for the inversion, it also reduced the uncertainty in the measurements at the same time.

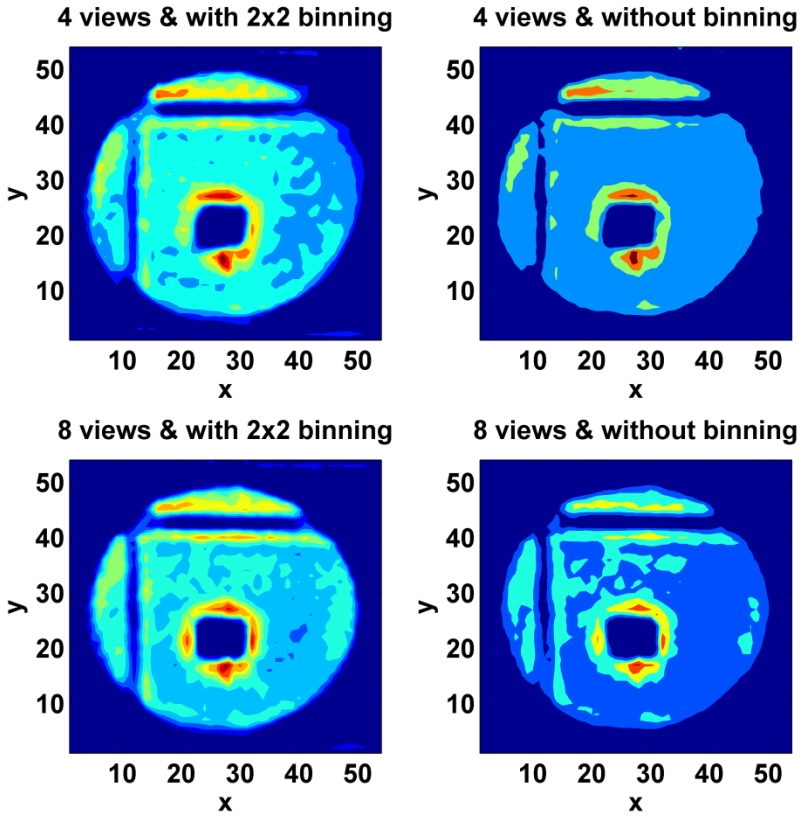

Figure 4-16. Layer 1 of the reconstructions from experimentally measured projections

Figure 4-17 shows a quantitative analysis of the results in Figure 4-16 by focusing on the vertical column blocked in the flame. As mentioned in Section 4.2, the blocked column had a width of 1.25 mm, representing the smallest spatial feature created in the experiments. Based on the reconstructions shown in Figure 4-17, we extracted the width of the column by calculating the gradient of the reconstruction and locating the sharpest CH^* concentration change. Figure 4-17 shows the reconstructed width of the column under the conditions used in Figure 4-16. Note that the reconstructed width may vary along the column (i.e., at difference *y* locations). Therefore, multiple values were

obtained from each layer and Figure 4-17 shows the median (the solid symbols) and standard deviation (the error bars) of these values.

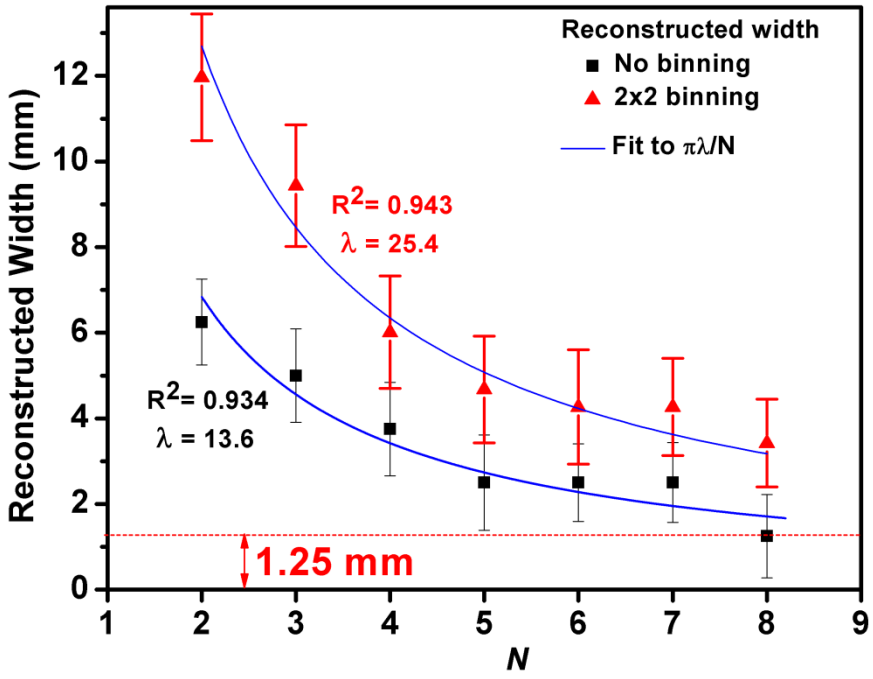

Figure 4-17. Reconstruction of experimental data with and without binning the measured projections.

Several observations can be made based on the results shown in Figure 4-17. First, the spatial resolution of the reconstruction, quantified by the width of the blocked column, improved with increasing number of views used. Figure 4-17 also shows the fit of the results to the Fourier Slice Theorem [124, 125], which predicts the spatial resolution of the reconstruction to be $\pi\lambda/N$, where λ is a characteristic spatial scale. As seen, the data were accurately captured by the theorem. Second, different λ was determined when binning was applied to the measured projections, leading to a different resolving power of the tomographic inversion. Therefore, even though the results shown in Figure 4-16 suggest that binning did not cause significant degradation to the overall reconstruction quality, the quantitative analysis shown in Figure 4-17 show that binning does affect the

resolving power of the tomographic inversion. Third, when projection data from 8 views were used without binning, the tomographic inversion was able to resolve the minimum feature in the flame (1.25 mm), demonstrating the spatial resolution of the 3D diagnostic technique.

Figure 4-18 and Figure 4-19 show numerical results performed using phantoms to simulate the experiments described above. As can be seen, the same observations can be made from these numerical results as those made from the experimental results. Finally, we make two notes before leaving these discussions. First, in the numerical simulations, both the width of the blocked column and *e* can be calculated due to the precisely known phantoms. The reconstructed width and its fit showed the same trend as those seen in Figure 4-17 from the experimental data. Therefore, here Figure 4-19 shows *e* from the numerical simulations rather than the width of the blocked column. The results in Figure 4-19 show that *e* can be fitted accurately by the Fourier Slice Theorem too, which could be useful for quantifying the inversion accuracy of targets with no distinct spatial features. Second, the Fourier Slice Theorem was developed for the ART algorithm, and results obtained in this work suggested that it also applies to the TISA algorithm.

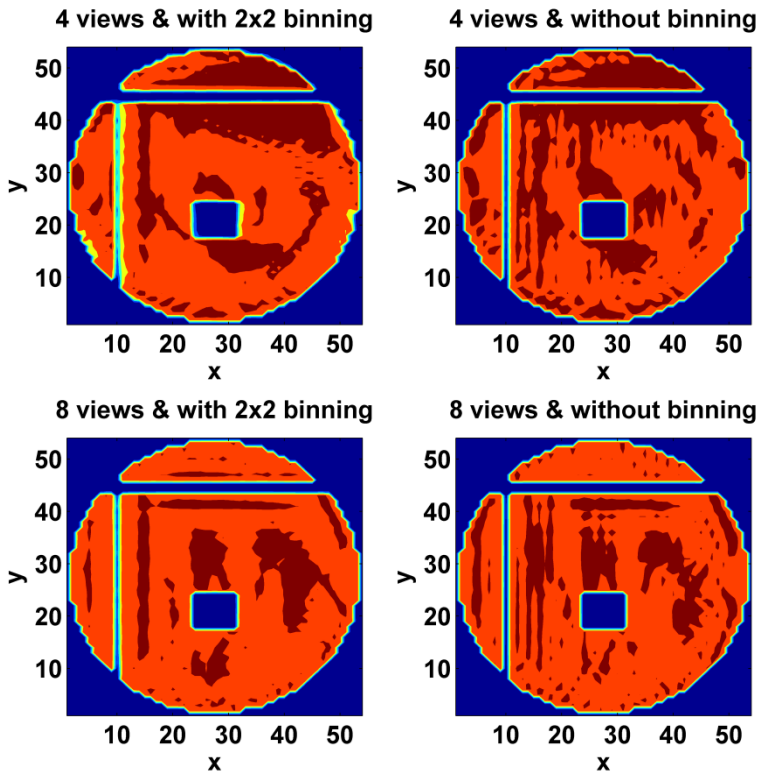

Figure 4-18. Layer 1 of the reconstructions from simulated projections.

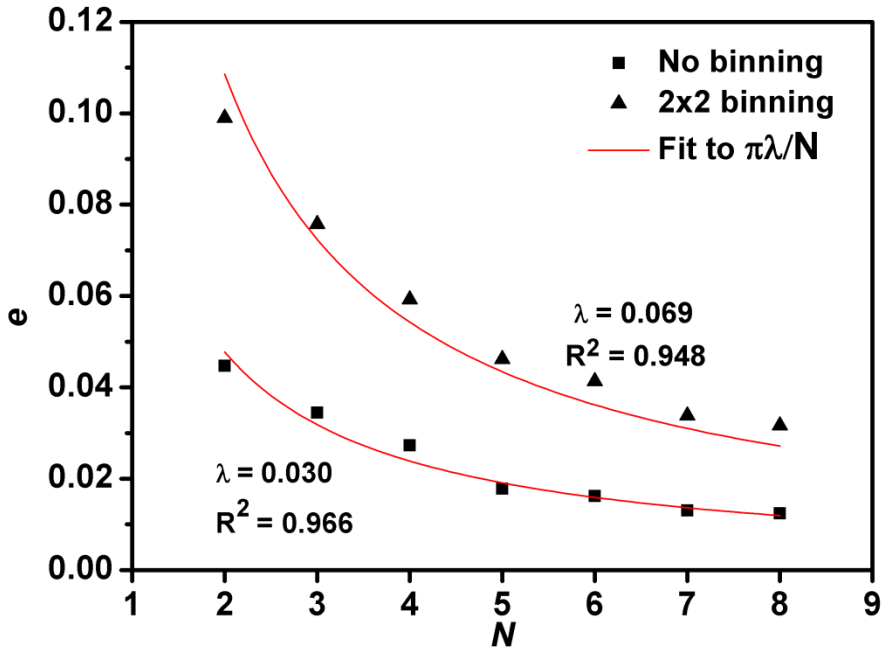

Figure 4-19. Reconstruction of experimental data with and without binning the simulated projections

Lastly, in practice, the number of views is an important parameter in the design of tomographic combustion diagnostics. These observations made here illustrate the practical factors that should be considered in determining the optical number of views. These factors include fundamental considerations such as the desired spatial resolution and pragmatic factors such as the computational cost and optical access. The results shown here should provide valuable guidance to the holistic consideration of these factors.

4.8 Summary

In summary, this chapter discusses a 3D combustion diagnostic based on tomographic chemiluminescence (TC). The TC techniques have several distinct advantages when compared to other non-intrusive laser diagnostics. The major contributions of this research are threefold. First, a hybrid algorithm is developed to solve the 3D TC problem. The algorithm is validated by extensive numerical simulations and experimental data. The hybrid algorithm outperformed other algorithms that we surveyed in terms of the reconstruction error, and was demonstrated to perform reconstruction with high fidelity using a limited number of view angles in the presence of noises. Second, a set of experiments were designed to both demonstrate the 3D TC technique, and also to examine its performance quantitatively. The experimental approach involves creating controlled flame patterns using a McKenna burner. These flame patterns enable quantifiable metrics to experimentally examine several critical aspects of the TC technique, such as the spatial resolution and reconstruction accuracy. The experimental results provide data that directly demonstrate a spatial resolution on the order of 1.25 mm and reconstruction with good fidelity with a limited number of projections. Third, based on the reconstruction algorithm and experimental results, we investigated the effects of

the view orientations. The results suggested that for an unknown flame, it is better to use projections measured from random orientations than restricted orientations (e.g., coplanar orientations) because projections from random orientations are statistically more likely to provide complimentary information. Lastly, note that the second and third contributions are independent of the first one. We have examined our experimental data and the effects of view angles using different inversion algorithms, and the trend of the results obtained agreed with those obtained by the hybrid algorithm as reported.

Four practical aspects for implementing 3D tomographic inversion under the context of volumetric flame imaging were investigated. These aspects include: 1) the termination criteria of the inversion algorithm; 2) the effects of regularization and the determination of the optimal regularization factor; 3) the effects of number of views, and 4) the impact of the resolution of the projection measurements. Both numerical simulations and controlled experiments were performed to study them. The results obtained have shown the difficulties of designing an effective termination criterion, and suggested that the new TISA algorithm can be terminated effectively on all the cases tested. Regularization has been demonstrated to significantly enhance the accuracy of inverting smooth flames and/or flames with clear edges. An L-curve method was found to be able to determine the optimal regularization parameter. Increasing the number of views and the resolution of the projections has been shown to improve both the accuracy and the resolving power, which agreed with theoretical predictions. The results obtained have illustrated the effects of these practical aspects on the accuracy and spatial resolution of 3D diagnostics based on tomography inversion. Furthermore, these aspects, for instance the number of views and the resolution of the projection measurements, are all related to the complexity and

implementing cost (both hardware cost and computational cost). Therefore, we expect the results obtained in this chapter to facilitate the practical implementation of 3D combustion diagnostics. For example, in our ongoing work, we are designing temporally-resolved 3D diagnostics for practical combustors, which pose several challenges including restricted optical access, large measurement volume, and large data volume. The results discussed in this chapter provide key information to many aspects of the design, which aims at obtaining an optimal balance of spatial resolution, temporal resolution, hardware cost, and computational cost.

Chapter 5 Conclusion and Future Work

So far, in this dissertation, we have introduced three novel techniques for multi-dimensional, non-intrusive flow and combustion diagnostics. These techniques used advanced numerical algorithms, such as Monte Carlo algorithm, simulated annealing, and algebraic reconstruction technique, to predict and reconstruct multi-dimensional distributions of temperature, species concentrations, etc. These techniques have been numerically verified and experimentally validated, and their practical applications in non-reacting flows, jet engine combustion, and other types of flames have been demonstrated. These methods have exhibited great potential to solve practical industrial problems and future investigation on these techniques is necessary to improve these existing techniques.

The future work will focus on improving the existing techniques in the aspect of computational cost, signal level, optical access, resolution, etc. To improve the efficiency of existing techniques, the algorithms implemented in these techniques should be optimized and new optimization algorithms, such as genetic algorithms, should be explored to cut the computational cost and allow *in-situ* measurement and reconstruction. Different experimental setup and the implementation of new hardware, such as high-speed cameras and camera intensifiers can significantly improve the signal level. New target species that provides stronger signals can also be used to measure non-species feature, such as temperature, pressure, flow and flame structure, etc. Furthermore, increasing the signal level can also improve the temporal resolution of the proposed techniques since the exposure time can be reduced with higher signal. To circumvent limited optical access, optical imaging fiber bundles can be used to achieve two-

dimensional measurement with a certain level of attenuation. Some preliminary investigations and researches have been done using imaging fiber bundles to perform TC measurement and satisfactory results in flame structure and spatial resolution have been demonstrated. To enhance the spatial resolution, improvements in both hardware and software are required. In the aspect of hardware, more compacted sensors (for HT techniques) and high-resolution imaging cameras (for TC technique) are recommended. In the aspect of software, more robust and efficient algorithms are needed to handle inversion problems with thousands or millions of unknowns since the number of unknown will increase with a smaller spatial resolution. Some of the preliminary results in spatial resolution can be found in [126] .

References

1. A. C. Eckbreth, *Laser diagnostics for combustion temperature and species*, Gordon and Breach Publishers, The Netherlands (1996).
2. K. Kohse-Hoinghaus, R. S. Barlow, M. Alden, and E. Wolfrum, "Combustion at the focus: laser diagnostics and control," Proceedings of the Combustion Institute **30**, 89-123 (2005).
3. H. Schiff, G. Mackay, and J. Bechara, "The use of tunable diode laser absorption spectroscopy for atmospheric measurements," Research on chemical intermediates **20**, 525-556 (1994).
4. L. Ma and W. C. Cai, A.W.; Kraetschmer, T.; Sanders, S.T.; Roy, S.; Gord, J.R, "Tomographic imaging of temperature and chemical species based on hyperspectral absorption spectroscopy," Optics Express **17**, 8602-8613 (2009).
5. J. R. Mourant, I. J. Bigio, J. Boyer, R. L. Conn, T. Johnson, and T. Shimada, "Spectroscopic diagnosis of bladder cancer with elastic light scattering," Lasers in surgery and medicine **17**, 350-357 (1995).
6. X. Sun, X. Li, and L. Ma, "A closed-form method for calculating the angular distribution of multiply scattered photons through isotropic turbid slabs," Optics Express **19**, 23932-23937 (2011).
7. S. Nie and S. R. Emory, "Probing single molecules and single nanoparticles by surface-enhanced Raman scattering," science **275**, 1102-1106 (1997).
8. F. Wang, M. Y. Sfeir, L. Huang, X. H. Huang, Y. Wu, J. Kim, J. Hone, S. O'Brien, L. E. Brus, and T. F. Heinz, "Interactions between individual carbon nanotubes studied by Rayleigh scattering spectroscopy," Physical review letters **96**, 167401 (2006).
9. A. Zumbusch, G. R. Holtom, and X. S. Xie, "Three-dimensional vibrational imaging by coherent anti-Stokes Raman scattering," Physical review letters **82**, 4142-4145 (1999).
10. J. M. Seitzman, G. Kychakoff, and R. K. Hanson, "Instantaneous temperature field measurements using planar laser-induced fluorescence," Optics letters **10**, 439-441 (1985).
11. R. J. Santoro and C. R. Shaddix, "Laser-induced incandescence," Applied combustion diagnostics, 252-286 (2002).
12. D. A. Lyn, S. Einav, W. Rodi, and J.-H. Park, "A laser-Doppler velocimetry study of ensemble-averaged characteristics of the turbulent near wake of a square cylinder," Journal of Fluid Mechanics **304**, 285-319 (1995).

13. R. J. Adrian, "Particle-imaging techniques for experimental fluid mechanics," Annual review of fluid mechanics **23**, 261-304 (1991).
14. J. Floyd and A. M. Kempf, "Computed tomography of chemiluminescence (CTC): high resolution and instantaneous 3D measurements of a matrix burner," Proceedings of the Combustion Institute **33**, 751-758 (2011).
15. X. L. Weiwei Cai, Fei Li, and Lin Ma, "Numerical and experimental validation of a three-dimensional combustion diagnostic based on tomographic chemiluminescence," Optics Express **21**, 7050-7064 (2013).
16. M. Sommerfeld and H.-H. Qiu, "Detailed measurements in a swirling particulate two-phase flow by a phase-Doppler anemometer," International Journal of Heat and Fluid Flow **12**, 20-28 (1991).
17. X. An, T. Kraetschmer, K. Takami, S. T. Sanders, L. Ma, W. Cai, X. Li, S. Roy, and J. R. Gord, "Validation of temperature imaging by H2O absorption spectroscopy using hyperspectral tomography in controlled experiments," Applied Optics **50**, A29-A37 (2011).
18. M. Kang, Li, X., Ma, L., "Three-dimensional flame measurements using fiber-based endoscopes," Submitted to 35th International Symposium on Combustion (2014).
19. D. Elson, I. Munro, J. Requejo-Isidro, J. McGinty, C. Dunsby, N. Galletly, G. Stamp, M. Neil, M. Lever, and P. Kellett, "Real-time time-domain fluorescence lifetime imaging including single-shot acquisition with a segmented optical image intensifier," New Journal of Physics **6**, 180 (2004).
20. R. Wellander, M. Richter, and M. Aldén, "Time resolved, 3D imaging (4D) of two phase flow at a repetition rate of 1 kHz," Optics Express **19**, 21508-21514 (2011).
21. M. Harker, T. Hattrell, M. Lawes, C. Sheppard, N. Tripathi, and R. Woolley, "Measurements of the Three-Dimensional Structure of Flames at Low Turbulence," Combustion Science and Technology **184**, 1818-1837 (2012).
22. C. Lindstrom, C.-J. Tam, D. Davis, D. Eklund, and S. Williams, *Diode laser absorption tomography of 2D supersonic flow* (American Institute of Aeronautics and Astronautics, 2007).
23. F. Wang, K. Cen, N. Li, J. B. Jeffries, Q. Huang, J. Yan, and Y. Chi, "Two-dimensional tomography for gas concentration and temperature distributions based on tunable diode laser absorption spectroscopy," Measurement Science and Technology **21**, 045301 (2010).

24. L. Ma, W. Cai, A. W. Caswell, T. Kraetschmer, S. T. Sanders, S. Roy, and J. R. Gord, "Tomographic imaging of temperature and chemical species based on hyperspectral absorption spectroscopy," Optics Express **17**, 8602-8613 (2009).
25. L. Ma and W. Cai, "Numerical investigation of hyperspectral tomography for simultaneous temperature and concentration imaging," Applied Optics **47**, 3751-3759 (2008).
26. G. E. Elsinga, F. Scarano, B. Wieneke, and B. Van Oudheusden, "Tomographic particle image velocimetry," Experiments in Fluids **41**, 933-947 (2006).
27. R. Hain, C. J. Kähler, and D. Michaelis, "Tomographic and time resolved PIV measurements on a finite cylinder mounted on a flat plate," Experiments in Fluids **45**, 715-724 (2008).
28. T. Upton, D. Verhoeven, and D. Hudgins, "High-resolution computed tomography of a turbulent reacting flow," Experiments in Fluids **50**, 125-134 (2011).
29. X. Li, F. He, and L. Ma, "Thermal management of cylindrical batteries investigated using wind tunnel testing and computational fluid dynamics simulation," Journal of Power Sources **238**, 395-402 (2013).
30. F. He, X. Li, and L. Ma, "Combined experimental and numerical study of thermal management of battery module consisting of multiple Li-ion cells," International Journal of Heat and Mass Transfer **72**, 622-629 (2014).
31. Y. Zhao, X. Li, and L. Ma, "Multidimensional Monte Carlo model for two-photon laser-induced fluorescence and amplified spontaneous emission," Computer Physics Communications **183**, 1588-1595 (2012).
32. N. Georgiev and M. Alden, "Two-dimensional imaging of flame species using two-photon laser-induced fluorescence," Applied Spectroscopy **51**, 1229-1237 (1997).
33. J. H. Frank, X. Chen, B. D. Patterson, and T. B. Settersten, "Comparison of nanosecond and picosecond excitation for two-photon laser-induced fluorescence imaging of atomic oxygen in flames," Applied Optics **43**, 2588-2597 (2004).
34. N. J. Bednar, J. W. Walewski, and S. T. Sanders, "Assessment of multiphoton absorption in inert gases for the measurement of gas temperatures," Applied spectroscopy **60**, 246-253 (2006).
35. A. Hsu, V. Narayanaswamy, N. Clemens, and J. Frank, "Mixture fraction imaging in turbulent non-premixed flames with two-photon LIF of krypton," Proceedings of the Combustion Institute **33**, 759-766 (2011).

36. M. Richter, Z. Li, and M. Aldén, "Application of two-photon laser-induced fluorescence for single-shot visualization of carbon monoxide in a spark ignited engine," Applied Spectroscopy **61**, 1-5 (2007).
37. U. Westblom and M. Aldén, "Laser-induced fluorescence detection of NH3 in flames with the use of two-photon excitation," Applied Spectroscopy **44**, 881-886 (1990).
38. K. Nyholm, R. Fritzon, N. Georgiev, and M. Aldén, "Two-photon induced polarization spectroscopy applied to the detection of NH3 and CO molecules in cold flows and flames," Optics Communications **114**, 76-82 (1995).
39. J. E. M. Goldsmith, "Photochemical effects in two-photon-excited fluorescence detection of atomic oxygen in flames," Applied Optics **26**, 3566-3572 (1987).
40. J. E. M. Goldsmith, "Two-photon-excited stimulated emission from atomic hydrogen in flames," J. Opt. Soc. Am. B **6**, 1979-1985 (1989).
41. N. Georgiev, K. Nyholm, R. Fritzon, and M. Aldén, "Developments of the amplified stimulated emission technique for spatially resolved species detection in flames," Optics Communications **108**, 71-76 (1994).
42. A. D. Tserepi, E. Wurzberg, and T. A. Miller, "Two-photon-excited stimulated emission from atomic oxygen in rf plasmas: detection and estimation of its threshold," Chemical Physics Letters **265**, 297-302 (1997).
43. L. W. Casperson, "Rate-equation approximations in high-gain lasers," Physical Review A **55**, 3073 (1997).
44. J. W. Daily, "Use of rate equations to describe laser excitation in flames," Applied Optics **16**, 2322-2327 (1977).
45. J. Amorim, G. Baravian, and J. Jolly, "Laser-induced resonance fluorescence as a diagnostic technique in non-thermal equilibrium plasmas," Journal of Physics D: Applied Physics **33**, R51 (2000).
46. H. Bergström, H. Lundberg, and A. Persson, "Investigations of stimulated emission onB-A lines in CO," Zeitschrift für Physik D Atoms, Molecules and Clusters **21**, 323-327 (1991).
47. Y. L. Huang and R. J. Gordon, "The effect of amplified spontaneous emission on the measurement of the multiplet state distribution of ground state oxygen atoms," The Journal of chemical physics **97**, 6363-6368 (1992).
48. J. Amorim, G. Baravian, M. Touzeau, and J. Jolly, "Two - photon laser induced fluorescence and amplified spontaneous emission atom concentration measurements in O2 and H2 discharges," Journal of Applied Physics **76**, 1487-1493 (1994).

49. Y. Zhao, C. Tong, and L. Ma, "Demonstration of a new laser diagnostic based on photodissociation spectroscopy for imaging mixture fraction in a non-premixed jet flame," Applied Spectroscopy **64**, 377-383 (2010).
50. Y. Zhao, C. Tong, and L. Ma, "Assessment of a novel flow visualization technique using photodissociation spectroscopy," Applied Spectroscopy **63**, 199-206 (2009).
51. T. B. Settersten and M. A. Linne, "Modeling pulsed excitation for gas-phase laser diagnostics," J. Opt. Soc. Am. B **19**, 954-964 (2002).
52. L. Allen and G. Peters, "Amplified spontaneous emission and external signal amplification in an inverted medium," Physical Review A **8**, 2031 (1973).
53. M. E. Riley, "Growth of parametric fields in (2+ 1)-photon laser ionization of atomic oxygen," Physical Review A **41**, 4843 (1990).
54. M. Aldén, J. E. M. Goldsmith, and U. Westblom, "Two-photon-excited stimulated emission from atomic oxygen in flames and cold gases," Optics Letters **14**, 305-307 (1989).
55. S. Agrup, F. Ossler, and M. Aldén, "Measurements of collisional quenching of hydrogen atoms in an atmospheric-pressure hydrogen oxygen flame by picosecond laser-induced fluorescence," Appl. Phys. B **61**, 479-487 (1995).
56. K. Niemi, V. Schulz-Von Der Gathen, and H. Döbele, "Absolute calibration of atomic density measurements by laser-induced fluorescence spectroscopy with two-photon excitation," Journal of Physics D: Applied Physics **34**, 2330 (2001).
57. L. Cerdán, A. Costela, and I. García-Moreno, "On the characteristic lengths in the variable stripe length method for optical gain measurements," J. Opt. Soc. Am. B **27**, 1874-1877 (2010).
58. R. K. Hanson, "Applications of quantitative laser sensors to kinetics, propulsion and practical energy systems," Proceedings of the Combustion Institute **33**, 1-40 (2011).
59. F. Mayinger and O. Feldmann, *Optical Measurements: Techniques and Applications* (Springer, Berlin Germany, 2001).
60. R. S. Barlow, "Laser diagnostics and their interplay with computations to understand turbulent combustion " Proceedings of the Combustion Institute **31**, 49-75 (2007).
61. I. Boxx, M. Stohr, C. Carter, and W. Meier, "Sustained multi-kHz flamefront and 3-component velocity-field measurements for the study of turbulent flames," Applied Physics B-Lasers and Optics **95**, 23-29 (2009).

62. M. Stoehr, I. Boxx, C. Carter, and W. Meier, "Dynamics of lean blowout of a swirl-stabilized flame in a gas turbine model combustor," Proceedings of the Combustion Institute **33**, 2953-2960 (2011).

63. B. H. Cheung and R. K. Hanson, "CW laser-induced fluorescence of toluene for time-resolved imaging of gaseous flows," Applied Physics B-Lasers and Optics **98**, 581-591 (2010).

64. K. N. Gabet, R. A. Patton, N. Jiang, W. R. Lempert, and J. A. Sutton, "High-speed CH_2O PLIF imaging in turbulent flames using a pulse-burst laser system," Applied Physics B-Lasers and Optics **106**, 569-575 (2012).

65. N. Jiang, M. Webster, W. R. Lempert, J. D. Miller, T. R. Meyer, C. B. Ivey, and P. M. Danehy, "MHz-rate nitric oxide planar laser-induced fluorescence imaging in a mach 10 hypersonic wind tunnel," Applied Optics **50**, A20-A28 (2011).

66. D. Hoffman, K. U. Münch, and A. Leipertz, "Two-dimensional temperature determination in sooting flames by filtered Rayleigh scattering," Optics Letter **21**, 525-527 (1996).

67. P. J. Emmerman, R. Goulard, R. J. Santoro, and H. G. Semerjian, "Multi-angular absorption diagnostics of a turbulent argon-methane jet," Journal of Energy **4**, 70-77 (1980).

68. P. Paci, Y. Zvinevich, S. Tanimura, B. E. Wyslouzil, M. Zahniser, J. Shorter, D. Nelson, and B. McManus, "Spatially resolved gas phase composition measurements in supersonic flows using tunable diode laser absorption spectroscopy," Journal of Chemical Physics **121**, 9964-9970 (2004).

69. A. M. Chojnacki, G. J. Wolga, and F. C. Gouldin, "Infrared color center laser system for tomographic determination of temperature and species concentration distributions in combusting systems," Combustion Science and Technology **134**, 165-181 (1998).

70. R. Villarreal and P. L. Varghese, "Frequency-resolved absorption tomography with tunable diode lasers," Applied Optics **44**, 6786-6795 (2005).

71. P. Wright, C. A. Garcia-Stewart, S. J. Carey, F. P. Hindle, S. H. Pegrum, S. M. Colbourne, P. J. Turner, W. J. Hurr, T. J. Litt, S. C. Murray, S. D. Crossley, K. B. Ozanyan, and H. McCann, "Toward in-cylinder absorption tomography in a production engine," Applied Optics **44**, 6578-6592 (2005).

72. C. T. Herman, *Image reconstruction from projections - the fundamentals of computerized tomography*, Computer Science and Applied Mathematics (Academic Press, New York, USA, 1980).

73. W. Cai, D. J. Ewing, and L. Ma, "Application of simulated annealing for multispectral tomography " Computer Physics Communications **179**, 250 (2008).
74. L. Ma and W. Cai, "Determination of the optimal regularization parameters in hyperspectral tomography," Applied Optics **47**, 4186 (2008).
75. S. Kirkpatrick and M. Vecchi, "Optimization by simulated annealing," Science **220**, 671-680 (1983).
76. S. A. Teukolski, B. P. Flannery, W. H. Press, and W. T. Vetterling, *Numerical Recipes in FORTRAN-The Art of Scientific Computing* (University Press, 1989).
77. A. Corana, M. Marchesi, C. Martini, and S. Ridella, "Minimizing multimodal functions of continuous variables with the "simulated annealing" algorithm Corrigenda for this article is available here," ACM Transactions on Mathematical Software (TOMS) **13**, 262-280 (1987).
78. I. O. Bohachevsky, M. E. Johnson, and M. L. Stein, "Generalized simulated annealing for function optimization," Technometrics **28**, 209-217 (1986).
79. S. Brooks and B. Morgan, "Optimization using simulated annealing," The Statistician, 241-257 (1995).
80. M. Padberg and G. Rinaldi, "A branch-and-cut algorithm for the resolution of large-scale symmetric traveling salesman problems," SIAM review **33**, 60-100 (1991).
81. L. Ingber, "Simulated annealing: Practice versus theory," Mathematical and Computer Modelling **18**, 29-57 (1993).
82. K. P. Savage, G. R. Beitel, R. S. Hiers, and R. J. Schulz, "Test capabilities in the AEDC/UTSI J85 turbojet test stand," US Air Force T&E Days, 1-10 (2007).
83. L. A. Kranendonk, X. An, A. W. Caswell, R. E. Herold, S. T. Sanders, R. Huber, J. G. Fujimoto, Y. Okura, and Y. Urata, "High speed engine gas thermometry by Fourier-domain mode-locked laser absorption spectroscopy," Optics Express **15**, 15115-15128 (2007).
84. S. I. Chou, D. S. Baer, R. K. Hanson, W. Z. Collison, and T. Q. Ni, "HBr concentration and temperature measurements in a plasma etch reactor using diode laser absorption spectroscopy," Journal of Vacuum Science and Technology A **19**, 477 (2001).
85. T. Kraetschmer, D. Dagel, and S. T. Sanders, "Simple multiwavelength time-division multiplexed light source for sensing applications," Optics Letter **33**, 738-740 (2008).
86. A. W. Caswell, T. Kraetschmer, K. Rein, S. T. Sanders, S. Roy, D. T. Shouse, and J. R. Gord, "Application of time-division-multiplexed lasers for measurements of gas

temperature and CH4 and H2O concentrations at 30 kHz in a high-pressure combustor," Applied Optics **49**, 4963-4972 (2010).

87. C. Jirauschek, B. Biedermann, and R. Huber, "A theoretical description of Fourier domain mode locked lasers," Optics Express **17**, 24013-24019 (2009).
88. X. An, A. W. Caswell, J. J. Lipor, and S. T. Sanders, "Determining the optimum wavelength pairs to use for molecular absorption thermometry based on the continuous-spectral lower-state energy," Journal of Quantitative Spectroscopy and Radiative Transfer **112**, 2355-2362 (2011).
89. L. Ma, X. Li, W. Cai, S. Roy, J. R. Gord, and S. T. Sanders, "Selection of multiple optimal absorption transitions for nonuniform temperature sensing," Applied Spectroscopy **64**, 1274-1282 (2010).
90. K. Kohse-Hoinghaus and J. B. Jeffries, *Applied combustion diagnostics* (Taylor & Francis, New York, 2002).
91. A. C. Eckbreth, *Laser diagnostics for combustion temperature and species* (Gordon and Breach Publishers, The Netherlands, 1996).
92. Y. Hardalupas, C. S. Panoutsos, and A. M. K. P. Taylor, "Spatial resolution of a chemiluminescence sensor for local heat-release rate and equivalence ratio measurements in a model gas turbine combustor," Experiments in Fluids **49**, 883-909 (2010).
93. M. Orain and Y. Hardalupas, "Measurements of local mixture fraction of reacting mixture in swirl-stabilised natural gas-fuelled burners," Applied Physics B-Lasers and Optics **105**, 435-449 (2011).
94. Y. Hardalupas, M. Orain, C. S. Panoutsos, A. Taylor, J. Olofsson, H. Seyfried, M. Richter, J. Hult, M. Alden, F. Hermann, and J. Klingmann, "Chemiluminescence sensor for local equivalence ratio of reacting mixtures of fuel and air (FLAMESEEK)," Applied Thermal Engineering **24**, 1619-1632 (2004).
95. Y. Zhao, C. Tong, and L. Ma, "Demonstration of a new laser diagnostic based on photodissociation spectroscopy for imaging mixture fraction in a non-premixed jet flame," Appl. Spectrosc. **64**, 377-383 (2010).
96. J. A. Sutton and J. F. Driscoll, "A method to simultaneously image two-dimensional mixture fraction, scalar dissipation rate, temperature and fuel consumption rate fields in a turbulent non-premixed jet flame," Experiments in Fluids **41**, 603-627 (2006).
97. B. O. Ayoolan, R. Balachandran, J. H. Frank, E. Mastorakos, and C. F. Kaminski, "Spatially resolved heat release rate measurements in turbulent premixed flames," Combustion and Flame **144**, 1-16 (2006).

98. S. Bockle, J. Kazenwadel, T. Kunzelmann, D. I. Shin, C. Schulz, and J. Wolfrum, "Simultaneous single-shot laser-based imaging of formaldehyde, OH, and temperature in turbulent flames," Proceedings of Combustion Institute **28**, 279-286 (2000).

99. N. Anikin, R. Suntz, and H. Bockhorn, "Tomographic reconstruction of the OH* chemiluminescence distribution in premixed and diffusion flames," Applied Physics B-Lasers and Optics **100**, 675-694 (2010).

100. Y. Ikeda, J. Kojima, and H. Hashimoto, "Local chemiluminescence spectra measurements in a high-pressure laminar methane/air premixed flame," Proceedings of the Combustion Institute **29**, 1495-1501 (2002).

101. J. Kojima, Y. Ikeda, and T. Nakajima, "Basic aspects of OH(A), CH(A), and C_2(d) chemiluminescence in the reaction zone of laminar methane-air premixed flames," Combustion and Flame **140**, 34-45 (2005).

102. H. N. Najm, P. H. Paul, C. J. Mueller, and P. S. Wyckoff, "On the adequacy of certain experimental observables as measurements of flame burning rate," Combustion and Flame **113**, 312-332 (1998).

103. K. Nakabe, Y. Mizutani, T. Hirao, and H. Fujioka, "An experimental study on detailed flame structure of liquid fuel sprays with and without gaseous fuel," Combustion and Flame **84**, 3-14 (1991).

104. J. Kojima, Y. Ikeda, and T. Nakajima, "Spatially resolved measurement of OH*, CH*, and C_2* chemiluminescence in the reaction zone of laminar methane/air premixed flames," Proceedings of the Combustion Institute **28**, 1757-1764 (2000).

105. Y. Hardalupas and M. Orain, "Local measurements of the time-dependent heat release rate and equivalence ratio using chemiluminescent emission from a flame," Combustion and Flame **139**, 188-207 (2004).

106. L. A. Feldkamp, L. C. Davis, and J. W. Kress, "Practical cone-beam algorithm," Journal of the Optical Society of America. A **1**, 612-619 (1984).

107. G. W. Faris and R. L. Byer, "Beam-deflection optical tomography of a flame," Optics Letter **12**, 155-157 (1987).

108. Y. Ishino and N. Ohiwa, "Three-dimensional computerized tomographic reconstruction of instantaneous distribution of chemiluminescence of a turbulent premixed flame," JSME International Journal Series B **48**, 34-40 (2005).

109. M. M. Hossain, G. Lu, and Y. Yan, "Optical fiber imaging based tomographic reconstruction of burner flames," IEEE Transactions, Instrumentation and Measurements **61**, 1417-1425 (2012).

110. C. T. Herman, *Image reconstruction from projections - the fundamentals of computerized tomography* (Academic Press, New York, USA, 1980).

111. X. An, T. Kraetschmer, K. Takami, S. T. Sanders, L. Ma, W. Cai, X. Li, S. Roy, and J. R. Gord, "Validation of temperature imaging by H_2O absorption spectroscopy using hyperspectral tomography in controlled experiments," Appl. Opt. **50**, A29-A37 (2011).

112. Q. Huang, F. Wang, J. Yan, and Y. Chi, "Simultaneous estimation of the 3D soot temperature and volume fraction distributions in asymmetric flames using high-speed stereoscopic images," Applied Optics **51**, 2968-2978 (2012).

113. L. Ma and W. Cai, "Numerical investigation of hyperspectral tomography for simultaneous temperature and concentration imaging," Appl. Opt. **47**, 3751-3759 (2008).

114. L. Ma and W. Cai, "Determination of the optimal regularization parameters in hyperspectral tomography," Appl. Opt. **47**, 4186-4192 (2008).

115. E. Y. Sidky, C. M. Kao, and X. H. Pan, "Accurate image reconstruction from few-views and limited-angle data in divergent-beam CT," Journal of X-Ray Science and Technology **14**, 119-139 (2006).

116. W. H. Press, S. A. Teukolsky, W. T. Vetterling, and B. P. Flannery, *Numerical recipes in FORTRAN: the art of scientific computing* (Cambridge University Press, New York, USA, 1992).

117. R. Crowther, D. DeRosier, and A. Klug, "The reconstruction of a three-dimensional structure from projections and its application to electron microscopy," Proceedings of the Royal Society, London, Ser. A **317**, 319-340 (1970).

118. H. M. Hudson and R. S. Larkin, "Accelerated image reconstruction using ordered subsets of projection data," IEEE Transactions, Medical Imaging **13**, 601-609 (1994).

119. W. Cai, D. J. Ewing, and L. Ma, "Investigation of temperature parallel simulated annealing for optimizing continuous functions with application to hyperspectral tomography," Applied Mathematics and Compututation **217**, 5754-5767 (2011).

120. W. Cai and L. Ma, "Hyperspectral tomography based on proper orthogonal decomposition as motivated by imaging diagnostics of unsteady reactive flows," Applied Optics **49**, 601-610 (2010).

121. D. S. Nobes, B. Wieneke, and R. P. Tatam, "Determination of view vectors from image warping mapping functions," Optical Engineering **43**, 407-414 (2004).

122. D. Verhoeven, "Limited-data computed-tomography algorithms for the physical sciences," Applied Optics **32**, 3736-3754 (1993).

123. P. C. Hansen, "Analysis of discrete ill-posed problems by means of the L-curve " Siam Review **34**, 561-580 (1992).

124. G. Frieder and G. T. Herman, "Resolution in reconstructing objects from electron micrographs," Journal of Theoretical Biology **33**, 189-211 (1971).

125. G. T. Herman and S. Rowland, "Resolution in algebraic reconstruction technique an experimental investigation of the resolving power of an algebraic picture reconstruction technique," Journal of Theoretical Biology **33**, 213-223 (1971).

126. L. Ma, Li, X., "Assessment of Signal Level, Measurement Volume, and Spatial Resolution in Tomographic Chemiluminescence," Submitted to Combustion and Flame (2014).